



Babes-Bolyai University
Faculty of Chemistry and Chemical
Engineering
Department of Chemical Engineering



Artificial Neural Network Modelling of Parametrized Photo-Induced Generation of Gold Nanoparticles and their Temperature Dynamics

PhD Student
Ana Maria Mihaela Gherman

Scientific advisor:
Prof. Dr. Ing. Paul Serban Agachi

Cluj-Napoca
2018

Table of Contents

Abbreviations and Nomenclature	4
General Information	8
Thesis motivation.....	8
Thesis objectives	8
Thesis structure.....	9
1. Introduction	10
1.1 Nanotechnology.....	10
1.2 Nanoparticles	11
1.3 Gold Nanoparticles	13
1.3.1 Gold Nanoparticle Properties	13
1.3.2 Gold Nanoparticle Synthesis	19
1.3.3 Nucleation and growth	30
1.3.4 Applications.....	31
2. Part A – Synthesis, characterization and modeling of the gold nanoparticles photochemical generation process	35
2.1 Introduction	35
2.2 Experimental	37
2.2.1 Chemicals	37
2.2.2 Instrumentation	37
2.2.3 Sample preparation	38
2.2.4 Characterization technique.....	39
2.2.5 The influence of the scanning velocity and irradiation power on the sample color	40
2.2.6 The influence of the scanning velocity and irradiation power on the LSPR absorption maxima	41
2.3 AuNP size determination	47
2.4 Modeling the AuNP size with ANN	50
2.4.1 The ANN model - 2 hidden Layer	53
2.4.1.1 Statistical assessment of ANN model	54
2.4.1.2 ANN model Predictions.....	55
2.4.2 Assessment of the input variables importance	58
2.4.3 The ANN model - 1 hidden Layer	58

2.4.3.1 Statistical assessment of ANN model	59
2.4.3.2 The relative impact of each process parameter on the particle size.....	61
2.5 Conclusions Part A	62
3. Part B - Gold Nanoparticles in Laser Fields: Heat Generation and Heat Transfer	64
3.1 Introduction	64
3.2 Temperature dynamics of a system that contains one spherical AuNP embedded in a polymer (PSS) matrix – the influence of AuNP size.....	68
3.2.1 Methods.....	68
3.2.2 Results and discussions.....	71
3.3 Temperature dynamics of a system that contains an ensemble of spherical AuNPs embedded in a polymer (PSS) matrix – the influence of the AuNP distribution	75
3.3.1 Methods.....	75
3.3.2 Results and discussions.....	77
3.4 Temperature dynamics of a system that contains an ensemble of spherical AuNPs embedded in a polymer (PSS) matrix – the influence of the interfacial thermal conductance	83
3.4.1 Methods.....	83
3.4.2 Results and discussions.....	85
3.5 Near field effects and temperature dynamics of laser irradiated gold nanoparticles.....	89
3.5.1 AuNPs in a cross-type geometry - 2D model	91
3.5.1.1 Methods	91
3.5.1.2. Results and discussions.....	94
3.5.2 3D Model - The influence of near field interactions on the AuNP temperature	98
3.5.2.1 Methods	98
3.5.2.2 Results and discussions	99
3.5.3 The influence of AuNPs distance on the AuNP heat generation and their maximum temperature. Comparison between two modelling approaches.	103
3.5.3.1 Methods	103
3.5.3.2 Results and discussions.....	104
3.6 Conclusions Part B.....	107
General conclusions	111
References	116

Abbreviations and Nomenclature

2D	Two dimensional geometry
3D	Three dimensional geometry
A	Parameter that includes details of the scattering process
AFM	Atomic force microscopy
AgNP	Silver nanoparticles
ANN	Artificial neural network
A_{spot}	Laser spot area [m^2]
AuNPs	Gold nanoparticles
BDAC	Benzylidimethylhexadecylammonium chloride
BEM	Boundary element method
c	Speed of light [m/s]
C1	Cube
c1, c2	Citrate : Gold(III) ratio
C_p	Specific heat [$\text{J kg}^{-1} \text{ K}^{-1}$]
CTAB	Cetyl trimethylammonium bromide
CTAC	Cetyltrimethylammonium chloride
D	Distance between two NP centers [m]
d_{AuNP}	Gold nanoparticle diameter [m]
DCI	Diameter of circumference [m]
DDA	Discontinuous deformation analysis
DLW	Direct laser writing
DNA	Deoxyribonucleic acid
e_c	Electron charge
e	Thermal effusivity
E	Electric field [V/m]
E^*	Complex conjugate of the electric field vector
E_0	Initial applied electric field amplitude [V/m]
Eb	Incident electric field [V/m]
Es	Scattered electric field [V/m]
Et	Total electric field [V/m]
f(t)	Laser pulse time profile
FDTD	Finite difference time domain
FEM	Finite element method
fs	Femtosecond
FWHM	Full width half maximum
G	Interface conductance [$\text{W}/(\text{m}^2\text{K})$]
G_c	Critical interface thermal conductance [$\text{W}/(\text{m}^2\text{K})$]
HAuCl_4	Tetrachloroauric acid

h_{oj}	Absolute value of connection weights between the hidden and the output layers
I	Radiation intensity [W/m^2]
i_j	Absolute value of connection weights between the input and the hidden layers
J	Current density [A/m^2]
k	Thermal conductivity [$\text{W m}^{-1} \text{K}^{-1}$]
k_0	Wavenumber
K_{abs}	Absorption efficiency
LSP	Localized surface plasmons
LSPR	Local surface plasmon resonance
L_x	Length of the System II [m]
L_y	Width of the System II [m]
L_z	Height of the System II [m]
m_{eff}	Electron effective mass
MFP	Mean free path
MIA	Multiple Image Alignment
mRNA	Messenger ribonucleic acid
n	Free electron density
NA	Numerical apertures
NaBH_4	Sodium borohydride
NaBr	Sodium bromide
NADH	Nicotinamide adenine dinucleotide
ND:YAG	neodymium-doped yttrium aluminum garnet
NDF	Neutral density filter
n_h	Number of neurons in the hidden layer
n_m	Refractive index of the surrounding medium
n_p	Number of data points
NPs	Nanoparticles
ns	Nanosecond
n_v	Number of neurons in the input layer
P, P1, P2	Radiation power [W]
PA	Photoacoustic
PEG	Poly(ethylene glycol)
PML	Perfectly matched layer
PMMA	Poly(methyl methacrylate)
PSS	Poly 4-styrenesulfonic acid
PT	Photothermal
Pt 1-4	Point in space

PVA	Poly(vinyl alcohol)
PVP	Poly(N-vinylpyrrolidone)
Q	Generated heat [W/m ³]
q	Heat flux [W/m ²]
Qml	Magnetic losses [W/m ³]
Q_{rh}	Resistive losses [W/m ³]
R	Pearson correlation coefficient
$R(y)$	Radius of curvature [m]
r _{AuNP}	Gold nanoparticle radius [m]
Rel _{err}	Neural network relative error (%)
RI	Relative importance
Rs	System radius [m]
SAXS	X-ray diffraction or small angle X-ray Scattering
SiO ₂	Silicon dioxide
SPR	Surface plasmon resonance
STEM	Scanning transmission electron microscope
T	Temperature
t ₀	Position of the center of the pulse peak
TEM	Transmission electron microscopy
TFILs	Thiol functionalized ionic liquids
Ti NP	Titanium nanoparticles
TiO ₂	Titanium dioxide
Tmax	Maximu temperature
Tmin	Minimum temperature
TOAB	Tetraoctylammonium bromide
Tx100	Non-ionic surfactant Triton X-100
UVA	Type A ultraviolet radiation
UVB	Type B ultraviolet radiation
V	Volume [m ³]
v ₂₋₈₀	Scanning velocities [m/s]
WD	Working distances
\bar{x}	Arithmetic mean of the experimental values
x _i	Experimental value
\bar{y}	Arithmetic mean of the ANN predicted values
y _i	ANN model predicted value
z_0	Rayleigh range [m]
ZnO	Zinc oxide
α_p	Polarizability [C·m ² ·V ⁻¹]

α	Thermal diffusivity [m ² /s]
γ	Phenomenological damping constant
γ_0	Bulk damping constant
ϵ	Permittivity
ϵ_0	Vacuum permittivity [F·m ⁻¹]
ϵ_1	Real part of the dielectric constant
ϵ_2	Imaginary part of the dielectric constant
ϵ_D	Drude term
ϵ_{IB}	Interband term that refers to the response of the d electrons
λ	Wavelength [nm]
λ_0, λ_1, D	Fitting parameters
μ_0	Vacuum permeability [H/m]
v_F	Velocity of the electrons at the Fermi level [m/s]
ρ	Density [kg/m ³]
σ_{abs}	Absorption cross section [m ²]
σ_{ext}	Extinction cross section [m ²]
σ_{sca}	Scatteringcross section [m ²]
τ	Gaussian pulse duration [s]
ψ and ξ	Riccati-Bessel functions
ψ' and ξ'	Riccati-Bessel function derivatives
ω	Angular frequency [rad/s]
$\omega(y)$	Spot radius [m]
ω_0	Gaussian beam waist radius [m]
ω_p	Bulk plasmon frequency [rad/s]

General Information

Thesis motivation

Gold nanoparticles are extensively studied because of their size dependent optical, electronic and photo-thermal properties, but also due to their excellent biocompatibility and large effective surface area. As a consequence of these unique characteristics, gold nanoparticles have applications in sensing, imaging, propagation of light, catalysis, drug delivery, photothermal therapy or bubble technology. As a result of these large number of applications, various gold nanoparticles synthesis methods have been developed. One of the most advantageous synthesis methods is the photochemical generation, technique which is known for its potential to generate gold nanoparticles in various media and, additionally, to control the reduction process *in situ*.

The challenge of all synthesis techniques is obtaining control over the size and shape of the metallic nanoparticles, process which implies knowing the influence of the reaction's chemical and physical parameters on the AuNPs morphology.

Regarding the photochemical synthesis process, one of the parameters that can influence the gold nanoparticles generation process is the temperature increase. This phenomena is caused by the photothermal effect produced in already formed nanoparticles, and is responsible for the AuNPs size diminish, and also for undesirable processes such as thin film deterioration, or in some cases ablation.

Thesis objectives

Within this work, a direct light writing method is used to photochemically generate thick film gold nanoparticles which are characterized using optic, spectroscopic and transmission electron microscopy investigations.

In order to control the gold nanoparticles diameter, an artificial neural network that takes into account all the important parameters that influence the formation of gold nanoparticles is developed. Thus, based on physical and chemical process parameters this mathematical model is able to reliably predict the gold nanoparticles dimension. Moreover, correlations between the predicted metallic nanoparticle dimensions and the essential process parameters is investigated.

Also, a hierarchy of the artificial neural network input parameters in terms of their influence over the gold nanoparticles size is studied.

A better control of the gold nanoparticles generation process also implies a temperature control management, which can be done only by investigating the factors that influence the gold nanoparticles temperature rise and determining the temperature dynamics in such systems. Therefore, the temperature dynamics in various systems that are irradiated with UV light is studied by means of mathematical modelling. The influence of particle size, number and their displacement in the surrounding matrix but also the influence of the interfacial thermal conductance on the gold nanoparticles temperature dynamics is studied. In addition, the effect of gold nanoparticles near-field interactions, their orientation regarding the electric field polarization and the gold nanoparticles distance on their heat generation and maximum temperature is investigated. Last, but not least, the impact of the modelling approaches on the gold nanoparticles heat generation is considered.

Thesis structure

The thesis is structured in three parts. The first part – **Introduction** – includes an overview of the gold nanoparticle synthesis methods and applications and the theoretical background needed to understand the gold nanoparticle optical and photothermal properties. The second part – **Part A** – presents the gold nanoparticles synthesis method, their size predictions based on the developed artificial neural network and also, the hierarchy of the artificial neural network input parameters in terms of their influence over the gold nanoparticles size is studied. The third part – **Part B** – focuses on the gold nanoparticles photothermal effect and studies the temperature dynamics in various systems that are irradiated with UV light, taking into account the propagation effects.

1. Introduction

1.1 Nanotechnology

One of the most widely accepted definitions of nanotechnology is given by Binns [1]: “the study and manipulation of matter at length scales of order of a few nanometers (100 atoms or so) to produce useful materials and devices”. An alternative definition is given by the Royal Society and the Royal Academy of engineering [2]: “Nanoscience is the study of phenomena and manipulation of materials at atomic, molecular and macromolecular scales, where properties differ significantly from those at a larger scale. Nanotechnologies are the design, characterization, production and application of structures, devices and systems by controlling shape and size at the nanometer scale”. The wide class of structures that have dimensions less than 100 nm and, on which nanotechnologies rely on, are called nanoparticles (NPs). These nanoscale particles are widely used in domains such as medicine, food industry, cosmetics or electronics and, as a consequence of the impact that their applications can have on our lives, thousands of researchers from all over the world are working in the nanotechnology field.

In medicine nanoparticles are used for cancer therapy [3,4], nanosurgery [4], cryosurgery [5], drug, gene or protein delivery [4,6], wound healing [7] and dentistry [8]. Thus, the most studied nanoparticles for these applications are silver nanoparticles (AgNPs) for their strong antimicrobial activity and gold nanoparticles (AuNPs) due to their excellent biocompatibility, tunable optical properties and their ability to generate heat when they are irradiated with a laser. In dentistry, nanoparticles are used in dental resin-based composites (to fill the space between larger filler particles), on the surface of implants to prevent infections (AgNPs) or to increase biocompatibility (Ti NPs).

In food industry nanoparticles are used as antimicrobials, as delivery systems to improve the bioavailability of bioactive compounds (coenzyme Q10, vitamins, calcium), antioxidants, color additives or anticaking agent [9]. For example metal and metal oxide nanoparticles (especially silver NP) are utilized in packaging and coating because of their well known antimicrobial functionality. The metal ions that are released outside the cell, at the surface of the cell or within the cell can alter the cellular function or structure. Furthermore the cell death through oxidative stress is caused by the physicochemical properties of the NP that allow excessive formation of reactive oxygen species [9]. Polymeric nanoparticles are used for encapsulation of flavonoids and

vitamins and release this bioactive compound in an acidic environment such as the stomach [9], whereas silicon dioxide (SiO_2) nanoparticles are used for thickening pastes, maintaining flow properties in powder products [9].

Related to medicine and food industry, sensors and especially biosensors are one of the most important applications of nanoparticles. AuNPs are successfully used for DNA sensors, glucose biosensors or NADH sensor [10–12], Quantum dots are used in applications such as immunoassays, nucleic acid detection or cellular labeling and analysis [13,14] and magnetic nanoparticles are used to design biosensors that are able to detect DNA/mRNA, enzymes, proteins, drugs or tumor cells [15].

The most popular nanoparticles in cosmetic industry are metallic nanoparticles such as TiO_2 , ZnO or AgNP. These nanoparticles are used for their antibacterial, anti-inflammatory properties (AuNPs, AgNPs, ZnO NP), protection of skin from UVA and UVB sun rays (ZnO , TiO_2) or regeneration and rebuilding of the skin (AuNPs, AgNPs, ZnO NPs) [16]. Fullerene nanomaterials are used in commercial skin and hair products due to their high anti-oxidant activity, antimicrobial and antiviral activity [17]. Moreover fullerenes are known as a melanin controlling agent and also as a hair growing agent [17]. Another example of nanoparticles used in cosmetics and pharmaceutical products are solid lipid nanoparticles and nanostructured lipid carriers. These particles are known for their occlusive properties, increase in skin hydration, increase of skin penetration and avoidance of systemic uptake [18].

In electronics nanoparticles are used for data storage (eg. FePt, CoPt), single electron transistors (AuNP) [19], organic field electron transistors (poly(3-hexylthiophene) NP) [20] or field effect transistors (carbon nanotubes) [21]. Also AgNP are used in metal inks that may be suitable for printed electronics. Due to their size, the melting point of such materials suffers a dramatic reduction and, in consequence, conductive films that have low resistance can be annealed at lower temperatures [22,23].

1.2 Nanoparticles

The fascinating thing about the ‘nanoworld’ is that the fundamental properties of a material (magnetization, chemical reactivity, mechanical properties – hardness, resistance, yield stress) start to change and become size dependent. For example an iron NP that has below 100 nm is fully magnetized and the strength of the magnetism per atom is enhanced [1]. The size dependent

chemical reactivity is best demonstrated by gold nanoparticles (AuNP). It is known that bulk gold does not corrode or tannish, thus being one of the least reactive chemical. However, 5 nm AuNPs are powerful catalysts that are mainly used for the oxidation of carbon monoxide.

An illustrative example for size dependent mechanical properties are aluminum alloys that have a yield strength (the load a material can tolerate before it becomes permanently deformed) four times higher than conventional aluminum based materials. Some articles also observe that copper nanoparticles can have a 10-fold increase [1].

As seen in the above-mentioned examples, based on the physical and chemical characteristics, several classes of nanoparticles are found. Therefore, carbon-based NPs (fullerenes and carbon nanotubes that can be used as gas adsorbents for environmental remediation or as support medium for different inorganic and organic catalysts), metallic NPs, ceramics NPs (they have applications in catalysis, photodegradation of dyes), semiconductor NPs, polymeric NPs and lipid based NPs are encountered in literature [24].

The metallic NPs are heavily utilized in biomedicine and engineering, thereby being one of the most studied classes. The ease with which these NPs are synthesized and modified chemically, their high surface to volume ratio, biocompatibility, stability, optical and magnetic properties make them exquisite candidates for various applications, but they are used especially in: targeted drug delivery, diagnostic imaging, biotechnology, biosensors or magnetic separation.

The two most important properties for the above-mentioned applications are: i) NPs that have a diameter much smaller than the wavelength of light, when excited in the visible spectrum, exhibit collective oscillations of free electrons at the metallic surfaces. By simply changing the NPs shape, size or orientation in the incident field, the surface plasmon resonance (SPR) can be shifted hundreds on nm. ii) A non zero magnetic moment in the ground state is encountered at the majority of elements because of the surface effects. For in vivo applications the metallic nanoparticles have to be biocompatible, stable and nontoxic, thereby ferromagnetic materials that are found in biologic systems (magnetite Fe_3O_4 , tetragonal magnetite $\gamma\text{-Fe}_2\text{O}_3$ and hexagonal magnetite $\alpha\text{-Fe}_2\text{O}_3$) are mostly used [25].

1.3 Gold Nanoparticles

1.3.1 Gold Nanoparticle Properties

In literature, a significant amount of articles are turning their attention to gold nanoparticles (AuNPs), which are part of the noble metal nanoparticle class. Compared to silver, platinum or palladium NP, AuNPs are studied on a large scale due to the fact that they are biocompatible, have excellent conductivity, possess a large effective surface area, have the ability to generate heat when are irradiated with visible light and, depending on their size, AuNPs have various strong vibrant colors. This unique optical characteristics in the visible region are caused by the AuNPs surface plasmon oscillations.

In bulk metals, plasmons are known as free electron collective oscillations that occur at a distinct frequency [26]. Also according to Fermi's liquid model, "plasmons describe a negatively charged electron cloud coherently displaced from its equilibrium position around a lattice made of positively charged ions" [26]. Thus, in bulk metals, the conduction electrons are quasi free electrons that are detached from their ionic core and can freely move through the metal's crystalline structure [26,27].

For nanoparticles that are much smaller than the wavelength of light, the electric field of incident light polarizes the whole assembly of conduction electrons, which generates surface charges that alternatively accumulate on opposite ends of the nanoparticle [27]. Because of the NPs oscillating polarization, a restoring force results from the generated electric field that opposes the excitation field [27]. Furthermore, the generation of heat and light scattering are the two ways through which this oscillation is damping. Therefore, in gold nanoparticles, due to the fact that the polarized oscillation is distributed over the whole particle volume, the plasmons are non propagating excitations, and are termed as localized surface plasmons (LSP) [26,27].

Two essential physical effects are associated to the localized surface plasmon: i) at the SPR frequency the AuNPs have a maximum optical extinction and also the extinction cross section is observed to be much larger than the geometric size ii) at the NP surface there is an enhancement in the electric field that rapidly decreases with increasing the distance from the particle [26].

One of the ways to describe the LSP is by assuming that the NP acts as a mass-spring harmonic oscillator where the electron density represents the mass and the Coulomb restoring force between the electrons and lattice atoms is determined by the spring constant. This theory of scattering and absorption of radiation by small spherical NPs (NPs that have the diameter much smaller than the

wavelength of light) provides a fairly good approximation for visible or near infrared radiated NP that have the size bellow 100 nm. Assuming the Frölich condition ($\varepsilon_{1AuNP} = -2\varepsilon_m$), this model gives the maximum polarizability (α_p) of a small sphere of sub-wavelength diameter in the electrostatic approximation [28].

$$\alpha_p = 3\varepsilon_m V_{AuNP} \frac{\varepsilon_{AuNP} - \varepsilon_m}{\varepsilon_{AuNP} + 2\varepsilon_m} \quad (1)$$

$$\varepsilon(\omega) = \varepsilon_1(\omega) + i\varepsilon_2(\omega) \quad (2)$$

where ε_m is the permittivity of the non-absorbing medium that surrounds the AuNPs, ε_{AuNP} is the AuNP permittivity and V_{AuNP} is the AuNP's volume, ε_1 is the real part of the dielectric constant and ε_2 is the imaginary part of the dielectric constant.

From the optics point of view, another consequence of the resonantly enhanced polarization is a concomitant enhancement in the efficiency with which a metal NP scatters and absorbs light [28]. Thus, the corresponding cross section for absorption and scattering are linked to the polarizability found in equation 1 [27]:

$$\sigma_{ext} = \sigma_{abs} + \sigma_{sca} \quad (3)$$

$$\sigma_{ext} = \frac{6\pi}{\lambda} \sqrt{\varepsilon_m} Im(\alpha) \quad (4)$$

$$\sigma_{ext} = \frac{18\pi}{\lambda} \varepsilon_m^{3/2} V_{AuNP} \frac{\varepsilon_{2AuNP}}{(\varepsilon_{1AuNP} + 2\varepsilon_m)^2 + \varepsilon_{2AuNP}^2} \quad (5)$$

For larger NPs a more accurate electrodynamic approach is needed because of the significant phase changes of the driving field over the particle volume [26,28]. Mie theory is one of the mathematical models that provides (for any optical constant) the optical properties for spherical NPs of any size that are embedded in an optically transparent medium. The approach is based on Maxwell equations and on the multipole expansion of the electromagnetic fields [26,29]. For non spherical NPs numerical models such as finite difference time domain (FDTD) method, finite element method (FEM) or boundary element method (BEM) are used.

Experimentally, the easiest way to probe the localized surface plasmon is to use the optical absorption spectroscopy which measures the optical extinction of the solid or liquid probe that contains the AuNPs. Far field extinction microscopy, electron energy loss spectroscopy or cathode luminescence are also experimental ways to directly probe the LSP in AuNPs [26].

Furthermore, based on both optical absorption spectroscopy and mathematical models, scientists observed that factors like AuNPs surrounding medium (through its dielectric constant) [30,31], the surface chemical interactions, the temperature [32], shape and size of the AuNPs [3,32–35] are heavily influencing the local surface plasmon resonance.

In their work Link et all studied theoretically and experimentally the influence of AuNP size on the LSPR [33,35]. In this regard, UV-vis absorption spectra of spherical AuNPs of 9, 22, 48 and 99 nm with a size distribution of 10% were considered. As a result, with increasing the metallic NP diameter, they obtained the following maximum plasmon absorption: 517 nm, 520 nm, 521 nm, 533 nm, 575 nm. It is seen that LSPR position is increasing with the increase of the AuNP diameter. Besides the maximum plasmon absorption, also the plasmon bandwidth is strongly influenced by the NP size [33]. The data obtained by Link et al suggest that until 22 nm the AuNPs decreases with increasing the AuNP size, and for AuNPs greater than this size the plasmon bandwidth will increase with the increase of the AuNPs diameter.

In fact it is established that for AuNPs that are below 25 nm the plasmon bandwidth is inversely proportional to the AuNP radius. This phenomenon is attributed to the fact that the dielectric function of bellow 25 nm spherical AuNPs is assumed to be size dependent and is mathematically modeled by the a modification of the dipole approximation of the Mie theory (see eq 5) in which the AuNPs dielectric function is both frequency and size dependent. In equation 5 the resonance condition for the plasmon absorption is roughly fulfilled when $\varepsilon_1(\omega)=-2\varepsilon_m(\omega)$ if $\varepsilon_2(\omega)$ is small or weakly dependent on w and the plasmon bandwidth mainly depends on $\varepsilon_2(\omega)$ [35]. In this theory however, the underlying relaxation mechanism are all included in the macroscopic material dielectric function, which does not distinguish between several possible decay processes. The plasmon resonance is directly related to the decay mechanism of the coherent motion of the free electrons which include the energy and the momentum dissipation. So, according to Drude model, the dielectric function can be written as follows [35]:

$$\varepsilon(\omega) = \varepsilon_{IB}(\omega) + \varepsilon_D(\omega) \quad (6)$$

$$\varepsilon_D(\omega) = 1 - \frac{\omega_p^2}{\omega^2 + i\gamma\omega} \quad (7)$$

$$\omega_p^2 = \frac{n * e_c^2}{\varepsilon_0 m_{eff}} \quad (8)$$

where ϵ_{IB} is an interband term that refers to the response of the d electrons, ϵ_D is the Drude term, ω_p is the bulk plasmon frequency, n is the free electron density, e_c is the electron charge, ϵ_0 is the vacuum permittivity, m_{eff} is the electron effective mass and γ is the phenomenological damping constant [35].

In the case of a perfect electron gas with $\gamma \ll \omega$, the damping constant equals the plasmon width. In the bulk material, γ is directly related to all scattering processes: electron-electron, electron-phonon and electron-defect scattering. For a bulk metal, the damping constant is calculated as the sum of all reciprocal relaxation times (Equation 9), with the electro-phonon relaxation time dominating [33].

$$\gamma = \frac{1}{\tau_{e-e}} + \frac{1}{\tau_{e-ph}} + \frac{1}{\tau_{e-def}} \quad (9)$$

For small particles, the surface of the AuNPs acts as an additional scatterer because the mean free path (MFP is about 50 nm for AuNP and the electron-phonon collision time of 35 fs) of the electrons becomes comparable to the size of the particle [35]. In case of very small AuNPs the dominant collisions (interactions) are those of the conduction electrons with the particle surface which leads to reduced effective mean free path. In these conditions, γ can be written as a function of the AuNP diameter (d_{AuNP}):

$$\gamma(d_{AuNP}) = \gamma_0 + \frac{2A\upsilon_F}{d_{AuNP}} \quad (10)$$

where γ_0 is the bulk damping constant, A is a parameter that includes details of the scattering process and υ_F is the velocity of the electrons at the Fermi level [33,35].

For larger AuNPs (AuNPs greater than 25nm) the increasing particle size leads to an increase in the plasmon bandwidth but also in the maximum plasmon absorption. In this case, within the Mie theory, the extinction cross section depends on high order multipole modes and it can be explained in terms of an inhomogeneous polarization of the AuNPs by the electric field. In other words the increase in the plasmon bandwidth is given by the faster loss of phase coherence of the plasmon resonance which can be described by the interactions between the dipole, quadrupole or higher order oscillatory motions of the free electrons. In this case, the dielectric function is not anymore size dependent and the plasmon resonance behavior is regarded as an extrinsic size effect [33].

As earlier mentioned, another parameter that dramatically influences the local surface plasmon resonance (LSPR) is the shape of the AuNPs [36–41]. AuNPs with shapes like nanospheres [38,40], nanoelipsoids [40], nanoplates [36], nanostars [37], nanotriangles [30], nanorods

[35,38,41], nanocubes and rhombic dodecahedra nanoparticles [39] where synthesized and UV-vis absorption spectra were taken. Thereby, in his work, Ah et al synthesized crystalline nanoplates and investigated the influence of the aspect ratio (with/thickness) on the maximum plasmon absorption. He observed that there are three distinct absorption peaks. One in the longer region which is attributed to the in plane plasmon resonance of AuNPs, one around 530 nm which is attributed to the out of plane dipole resonance and other peaks (at 730 nm or 930 nm) that are considered to be the contribution of multipole resonances which could be assigned to be the in plane quadrupole modes of AuNPs [36]. Daccaro et al synthesized gold nanostars that have four to six sharp branches. As in the nanoplates, the absorption spectrum shows tree distinct absorption peaks. The peak that is around 1300 nm (long band profile) is attributed to resonant longitudinal electron oscillations along the collinear branches, the 750 nm (medium band profile) absorption peak is attributed to resonant longitudinal electron oscillations along the isolated branches and the peak that is around 520 nm is assigned both to transversal resonant oscillations of the valence electrons of the branches and to some byproducts which are in fact small spherical AuNPs [37]. Also, in this work, a comparison between different aspect ratios of the gold nanostars is made. It is observed that a decrease in the aspect ratio (length of the branch/width of the branch) from 2.5 to 2 leads to a decrease in both the long band profile (from 1300 nm to 970 nm) and medium band profile (from 750 nm to 650 nm) [37]. Wu et al synthesized cubic and rhombic dodecahedral gold nanocrystals and experimentally obtained Uv-vis spectra of different nanocrystal sizes. Also, Murphy and Govorov present in their work comparisons between experimentally obtained spectra of gold nanospheres and nanorods of different sizes [38] and numerically calculated absorption spectra of nanospheres, nanocubes and nanoellipsoids [40]. As outlined earlier, in all the cases, an increasing nanocrystal aspect ratio leads to an increase in the plasmon absorption peak.

The surface chemical interactions and the surrounding media are influencing the LSPR through the dielectric permittivity which is directly linked to the refractive index. As mentioned before, the Drude model describes the collisions between the freely moving electrons and the lattice stationary ionic core (Equation 7) [42]. In regard to Equation 7, if the frequencies are in the visible and near infrared spectrum, the damping constant γ is much smaller than the plasmon frequency (ω_p) and the equation becomes [42]:

$$\epsilon_{1AuNP} = 1 - \frac{\omega_p^2}{\omega^2} \quad (11)$$

Knowing that $\epsilon_{1\text{AuNP}} = -2\epsilon_m$ (the resonant condition), $\omega=2\pi c/\lambda$, and $\epsilon_m=n_m^2$, Equation 11 becomes [42]:

$$\lambda_{max} = \lambda_p \sqrt{2n_m^2 + 1} \quad (12)$$

where λ_{max} is the maximum plasmon absorption, λ_p is the wavelength corresponding to the plasma frequency of the bulk metal, n_m is the refractive index of the surrounding medium and c is the speed of light [42].

Consequently, one can see that if the refractive index of the AuNPs surrounding medium changes, the LSPR will shift. Furthermore, Amendola et al suggested that the absorption of light by the AuNPs surrounding medium can generate different effects in the LSPR. In the case of a non-absorbing medium, an increase in the medium's dielectric constant leads to red-shift in the LSPR. This phenomena is demonstrated in [43,44] where the behavior of LSPR is numerically studied for gold nanorods that are embedded in air ($n_{air}=1$), water ($n_{H_2O}=1.333$), ethanol ($n_{et}=1.361$) and formamide ($n_{form}=1.428$). In [44] explains that for nanorods the absorption maximum of the both transversal and longitudinal mode red shifts and its intensity rises with the increase of the surrounding medium dielectric function. In the case of a light absorbing medium, besides shifting to different wavelengths, the LSPR can experience a shielding effect because of the absorption of light which is associated to the imaginary part of the dielectric constant [26]. This behavior may be seen in AuNPs that are embedded in graphene, metal oxides or semiconductor quantum dots [26].

The LSPR shift due to the interaction between the AuNPs surface and different molecules is mostly studied for sensing applications. The binding interactions between the AuNP surface and the analyte shift the plasmon absorption maxima due to the changes of the surface refractive index and implicitly the changes in the surface dielectric constant [26]. Soares et al studies the gold nanotriangles refractive index sensitivity using various concentrations (0-80% glucose) of aqueous solutions of glucose [30]. This results in a 34 nm red shift in the maximum plasmon absorption due to a refractive index variation from 1.33 to 1.40. Furthermore, [30] experimentally studies the LSPR in the case of hexadecyltrimethylammonium bromide (CTAB) capped gold nanotriangles (plasmon resonance peak at 697.2 nm) and the nanotriangles after functionalization with thiolated oligonucleotide and treatment with 6 mercaptohexanol (plasmon resonance peak at 713.6 nm). This redshift in the obtained UV-vis spectra corresponds to a change in the neighboring environment of the gold nanotriangles and is related to a refractive index rise from 1.435 (CTAB) to 1.462 (DNA). Besides oligonucleotides, AuNP can be functionalized with various analytes

which include: nucleic acids [45], amino acids [46,47], enzymes [48], proteins [48] or different neurotransmitters [49].

The main losses of a plasmonic system are described by the imaginary part of the AuNP dielectric constant ($\text{Im}[\epsilon_{\text{AuNP}}]$), the interband transitions being the primary source of loss.

The damping of the LSPR is described by the imaginary part of the AuNP dielectric constant ($\text{Im}[\epsilon_{\text{AuNP}}]$), the interband transitions being the primary source of loss. ϵ_{2AuNP} is also correlated to the dephasing time of the coherent electron oscillations [26]. Furthermore, the plasmon bandwidth is directly linked with the loss of coherence (a faster coherence loss leads to a larger bandwidth).

The main processes that have an important contribution in the LSPR damping are the radiative (light scattering) and the non radiative process (heat generation).

The heat generation depends on the electron relaxation and has the following dephasing mechanisms: electron-electron scattering (less than 500 fs dephasing time), electron-phonon scattering (1-5 ps dephasing time) and phonon-phonon interactions (additional surface effects that have a time scale of hundreds of ps up to ns) [26]. The charged particles that are accelerating and decelerating emit a far field radiation that is correlated with the radiative decay process [26]. Both processes are influenced by the NP size.

1.3.2 Gold Nanoparticle Synthesis

There are various ways of synthesizing gold colloids, but the most studied method is the AuNPs generation in an aqueous or organic phase. Historically, Michael Faraday in 1857 was the first scientist who produced gold colloidal nanoparticles by chemical reduction of an aqueous solution of gold chloride with phosphorus dissolved in carbon disulfide [50,51]. In 1951, Turkevich investigated the reduction of chloroauric acid in an aqueous solution [52]. He took into account reducing agents such as phosphorus, hydroxyl-amine, acetone, citric acid and trisodium citrate and he studied the size and shape of the generated AuNPs. He found that sodium citrate was the most promising reducing agent due to the fact that the spherical AuNPs are highly reproducible. Based on this reducing agent, Turkevich synthesised AuNPs of 20 nm (deep wine red color) as follows: the chloroauric acid solution was heated at the boiling point and sodium citrate was added with good mechanical stirring [52]. In 1973, based on Turkevich method, Frens controlled the synthesis of monodisperse AuNPs by varying the sodium citrate concentration [53]. Thus, at high sodium citrate concentrations he obtained 16 nm spherical AuNPs. With decreasing the reducing agent

concentration, the AuNPs diameter increases, but beyond 50 nm the results become less reproducible (the AuNPs are polydispersed and nonspherical) [53].

50 to 200 nm spherical monodispersed AuNPs were synthesized by Perrault with the seed growth method in which hydroquinone is used as a reducing agent [54]. This method is successfully used for the controlled size and shape AuNPs synthesis. The basic principle for this method implies two steps: i) preparation of small AuNPs denoted “seeds” ii) growth of the seed particles due to exposing them to a gold precursor and mild a reducing agent [54,55]. To ensure that the gold atoms generated in the second step do not undergo a second nucleation and are deposited on the surface of the seed particles, experimental conditions like the ratio of seed to metal salt should be controlled [51,54,55]. Based on this approach Jana developed a step by step seeding method to obtain a narrow size distribution AuNPs that have diameters between 5 and 40 nm [56]. Also Mallik et al. were the first to report the photochemically preparation of seeds and seeding technique in conjunction with successive reduction through photo-irradiation [57]. Besides the improved AuNPs size control, the shape can also be controlled through this technique. Jana reported spherical and rod-like AuNPs [58]. Spherical 3-4 nm gold nanoseeds were generated using borohydride as a reducing agent. For the further growth of gold nanorods, besides the previous formed seeds, HAuCl₄, ascorbic acid, silver ions and a rod-shaped micellar template were used. The small amount of silver ions is used for the shape induction (the silver ions are adsorbed on the AuNP surface leading to a stabilization of the nanorod surface and a growth restriction), whereas the ascorbic acid mild reducing agent can reduce the gold salt only in the presence of seeds [58]. By varying the concentration of seeds one can observe in the Uv-Vis spectra a longer plasmon band which corresponds to an increase in the aspect ratio of the nanorods. A drawback for this technique is the additional generation of spherical AuNPs which alters the plasmon band shape. Based on this technique, Nikoobakht adopted two strategies to synthesize gold nanorods that were divided into two categories: gold nanorods that have a plasmon band bellow 850 nm and gold nanorods with a pasmon band greater than 850 nm, respectively [59]. In the first approach, ascorbic acid is maintained as a reducing agent, and CTAB is used as a surfactant, whereas in the second approach a binary surfactant mixture of benzylidimethylhexadecylammonium chloride (BDAC) and CTAB is used. Thus, the use of only one surfactant (CTAB) leads to a maximum plasmon band of 850 nm. Nikoobakht explains that the CTAB surfactant covers the seed AuNP with which it forms a template whose size depends on the CTAB concentration and on the solution’s ionic

strength. The nanorods that are synthesized in the presence of both BDAC and CTAB surfactants have a maximum plasmon band greater than 850 nm and have a low reproducibility [59].

Besides spherical NPs and nanorods also nanostars, nanoprisms and cubic or rhombic dodecahedral nanoparticals can be synthesized based on the seed growth technique. The various shapes are due to the use of different reducing agents and capping ligands that have various concentrations. Daccaro generated seed AuNPs in Tx100 with NaBH₄ as a reducing agent [37]. Nanostars that have a diameter of circumference (DCI) of 76 nm are synthesized adding ascorbic acid to the aqueous solution that contains 4 nm seed AuNPs. With the same technique, but increasing the seed/growth volume ration smaller nanostars (a DCI of 46 nm) are formed [37]. Furthermore, Wu generates cubic and rhombic dodecahedral AuNPs using cetyltrimethylammonium chloride (CTAC) as a capping ligand, ascorbic acid as and reducing agent, 3-5 nm seed AuNPs and NaBr. Formation of one or the other shapes depends on adding different volumes of ascorbic acid (a greater volume is used for the synthesis of rhombic dodecahedral AuNPs) [39]. Nanoprisms are generated in a three step growth of 5 nm gold seeds in an aqueous solution that has CTAB as surface protecting agent and ascorbic acid as reducing agent and sodium hydroxide [60].

Brust and Schiffrin developed a two-phase AuNP synthesis method that implies the transfer of tetrachloroaurate from the aqueous solution into toluene (the organic phase) using tetraoctylammonium bromide (TOAB) as a phase transfer agent [61]. Furthermore they used dodecanthiol and an aqueous solution of sodium borohydride to generate AuNPs which can further be precipitated and dried into a powder. By using this method, cuboctohedral and isosahedral AuNPs that range between 1.5 and 5 nm are synthesized. The strong thiol-Au interactions give the AuNPs a superior stability and the advantage to be soluble in non polar solvents such as toluene, pentane or chlorophorm [50,61].

Based on Brust and Schriffin method, Martin developed a highly reproducible AuNP synthesis and he described a 2D self-assembly method of the alkenthiolate coated NPs [62]. The goal of synthesis is to generate 1-3 nm AuNPs in water and then transfer them into a non polar organic solvent. In this view, AuNPs are generated in water, using sodium borohydride as a reducing agent. Acetone is used for the phase transfer to an organic solution that contains hexane and dodecanthiol. A monolayer film of AuNPs is generated after the evaporation of a droplet formed by merging a hexane droplet that contains AuNPs and a bigger toluene droplet [62].

Besides dodecanthiol as a capping ligand, AuNPs can also be stabilized by thiol functionalized ionic liquids (TFILs) which can be designed to be either hydrophobic or hydrophilic. In this regard, using NaBH₄ as a reducing agent, Kim synthesized spherical AuNPs that have TFILs as capping ligand [63]. The NP size is between 2 and 3.5 nm, but it is observed that the AuNP diameter decreases with the increase in the number of thiol groups [63].

Various polymers or dendrimer are used to synthesize coted AuNPs. This common method is used both for easiness in controlling the AuNPs size and for its capability of generating highly stable AuNPs. Poly(N-vinylpyrrolidone) (PVP), poly(ethylene glycol) (PEG), poly(vinyl alcohol) (PVA), poly(methyl methacrylate) (PMMA) are only some of the commonly used stabilizing polymers. As a result, in their synthesis method, Oh et al used PEG that has at its end a thioctic acid (TA) or dihydrolipoic acid (DHLA) at one end and a reactive group to the other [64]. So, in the first step Au-TA-PEG-OCH₃ (metal-ligand precursors) are formed by mixing the tetrachloroauric acid with the modular ligands. Further, AuNP generation and growth is triggered by NaBH₄ addition and finally extra ligands are added to the Au core. AuNP that have a diameter between 1.5 to 18 nm can be prepared by controlling the Au:ligand ratio (an increase in the Au:ligand ration leads to an increase in the nanocrystal size) [64]. Yilmaz and Suzer used UV light to synthesize AuNPs in a PMMA matrices [65]. Spin coating is used to prepare a film that contains a solution of tetrachloroauric acid and PMMA in acetone. Even though the reduction of gold ions is complete after 30 min, depending on the gold concentration, the formation of NPs takes 12 to 24 h [65]. The same method (photochemical reduction) is used by Pucci et al to synthesize AuNPs in a film of poly(vinyl alcohol) and poly(ethylene)-co-(vinyl alcohol), the latter having a superior solubility at high temperatures [66]. Depending on the ligand, spherical AuNPs that range between 12 and 23 nm are formed. Furthermore, the irradiation time seems to influence the NP size in the sense that increasing the irradiation time leads to a reduction of the AuNPs size [66]. Seoudi also uses the UV irradiation (wavelength of 254 nm and 365 nm) to reduce an aqueous solution of tetrachloroauric acid using PVA as a surfactant stabilizer and borohydride as a reducing agent [67]. The influence of the irradiation time on the NP size is also studied, but in this study the AuNP size seems to increase with increasing the irradiation time [67].

The photochemical synthesis described above is part of the physical synthesis method that also include sonochemical methods, microwave assisted and electrochemical methods, radiolysis and

thermolysis. This methods have the advantage of using no chemical reductants and no thermal heating [50].

Besides the advantages already mentioned, the photochemical synthesis attracts the scientists interest because this technique is known for its great versatility (nanoparticles can be synthesized in various mediums such as emulsions, surfactant micelles, polymer films, glasses, cells) and additionally, the reduction can be controlled *in situ* [68]. Using this method, the reduction of gold precursors can be done through the following ways: i) a direct photo reduction or ii) a photosensitized reduction [68].

A possible reaction mechanism for the direct photo reduction is described by Eustis who studied the reaction mechanism of AuNP in ethylene glycol solution [69]. The main principle of this synthesis method is schematically represented in Figure 1 [68].

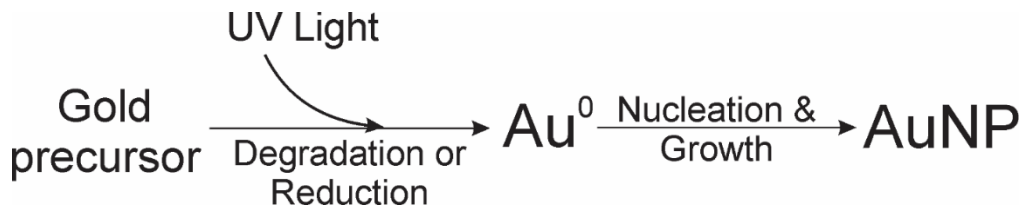


Figure 1. Schematic representation of the direct photo reduction [68]

The photosensitized reductions is the method that is usually preferred by the scientists because of the fast and efficient synthesis of AuNPs (compared to direct photo reduction) and because of its easiness in changing the excitation wavelength (it depends on the sensitizer). The scheme of this synthesis method is sketched in Figure 2.

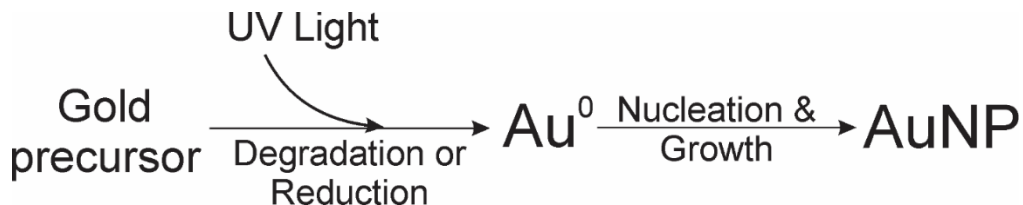


Figure 2. Schematic representation of the photosensitized reductions [68]

As seen in Figure 2, this approach implies the interaction between the UV light and photoactive reagents which generate intermediates (usually radicals) that reduce the gold precursor and form AuNPs. Based on the radical formation mechanism, the photoactive reagents can be classified in:

i) precursors that undergo hydrogen abstraction to form the radicals and ii) precursors that undergo bond cleavage [68].

Organic molecules such as acetone, acetophenone or benzophenone are excited by the UV light and abstract hydrogen atoms from different hydrogen donors such as α -alcohols [68,70]. Thus, the ketones are excited to the singlet state that further decays to the triplet excited state through intersystem crossing. The ketyl radical or other derived radicals form when the triplet excited state abstracts the hydrogen from the α -alcohol. The AuNPs are formed due to the reduction of the gold precursor by the generated radicals. It is worth mentioning that besides a hydrogen donor, the α -alcohol can also be a solvent and an oxidative radical precursor [68,70]. The mechanism of this synthesis is illustrated in Figure 3.

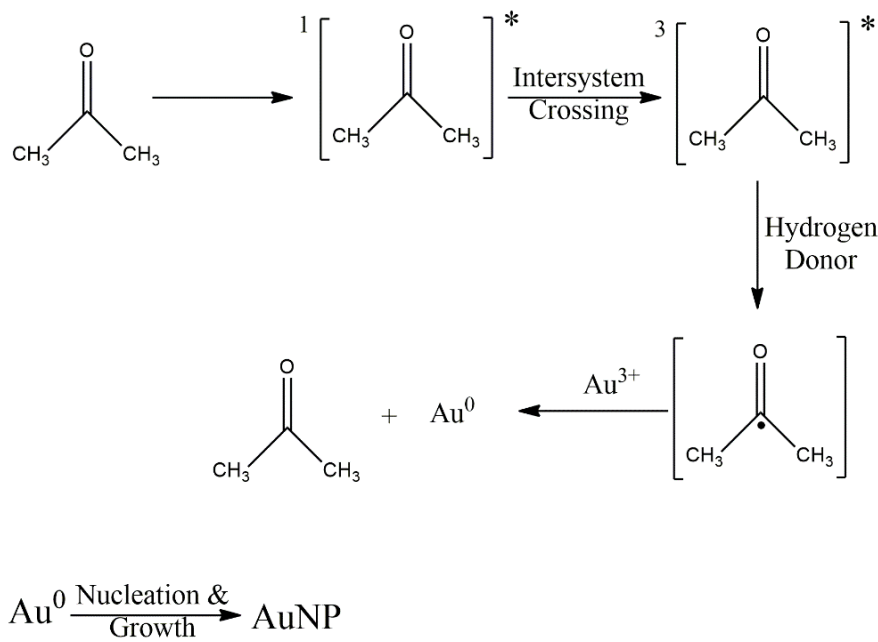


Figure 3. AuNP photosynthesis mechanism - the ketone-hydrogen donor system [70]

The bond cleavage is exemplified by McGilvray whom uses UVA light to produce benzoyl and acetone ketyl radicals via the Norrish type I reduction. It is demonstrated that the acetone ketyl radical reduces the tetrachloroaurate to generate AuNPs. In fact the Au^{3+} reduces to Au^{2+} which disproportionate to Au^{3+} and Au^+ . Au^+ reduces to Au^0 which agglomerates and, consequently, AuNPs are formed [71]. This synthesis mechanism is illustrated in Figure 4.

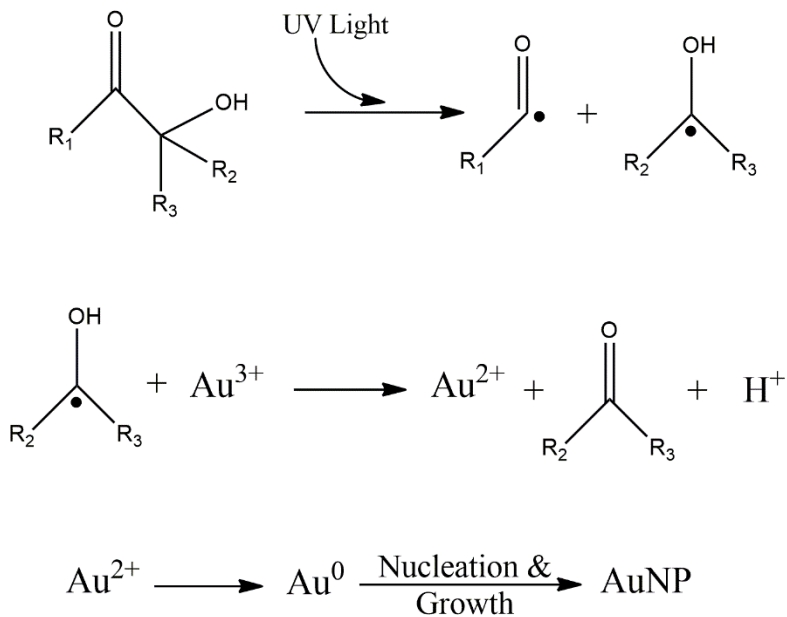


Figure 4. AuNP photosynthesis mechanism - the bond cleavage system [71]

The sonochemical synthesis of AuNPs relies on ultrasound irradiation of organic compounds which generate radical species that reduce gold precursors. The formation of hydrogen and hydroxyl radicals in water is based on passing high intensity ultrasound waves through a liquid in which gas bubbles generate, grow and finally violently collapse to produce the radical species. The frequency, the sonication time and the concentration of organic compounds may influence the AuNP size and shape. For example, Caruso used this method to reduce AuCl_4^- in the presence of several alcohols [72]. It is suggested that the alcohols adsorb on the AuNP surface and thus stabilize the NP and prevent its further growth. The increase in the sonication time and the alcohol (propanol) concentration and also a longer alkyl chain alcohol lead to a decrease in the NP size [72]. The influence of the ultrasound frequency on the reduction of tetrachloroaurate and, implicitly, on the AuNP size is studied by Okitsu [73]. In this article it is argued that the ultrasound frequency may have an effect on: i) the number, distribution, size and lifetime of the bubbles, ii) temperature and pressure of the collapsing bubble and iii) the dynamics and symmetry of the bubbles. Therfore, the factors may be interdependent, this behavior being reflected in the NPs size: until 200 kHz the AuNP size decreases, followed by an increase of the AuNPs for greater ultrasound intensities [73].

In the electrochemical synthesis method the current flow between the two electrodes can lead to the direct reduction of the gold salt. Yu immersed a gold metal plate (anode) and a platinum plate

(cathode) in an electrolytic solution of decyltrimethylammonium bromide, a cationic surfactant that also acts as a stabilizer [74]. Through this method cylindrical AuNPs were obtained.

By using the radiolytic method, active radicals or hydrated electrons are generated by γ beam irradiation. Using this technique, Henglein used an aqueous potassium tetrachloroaurate, methanol and surface protecting agents such as poly(vinyl alcohol) or PVP to prepare spherical AuNPs between 1.5 and 2.5 nm [75]. In this method Au^{3+} is reduced to Au^0 by the generated hydrated electrons and also by the hydroxymethyl radicals formed after the rapid reaction of hydroxyl radicals with methanol [75]. With the γ irradiation of a aqueous solution of $\text{KAu}(\text{CN})_2$, methanol and gold seeds from the previous synthesis, AuNPs can further be enlarged to a maximum size 120 nm.

AuNPs can also be synthesized by reducing tetrachloroaurate with sodium citrate in a closed chamber of a microwave system [76]. In this method an alternating electric field leads to a constant reorientation of the polar molecules in the liquid, phenomena which induces friction between molecules, friction which generates heat. In their microwave synthesis, Liu et al studied the influence of temperature upon the AuNPs size. It is observed that the temperature increase prevents NPs to aggregate, thus having a high dispersity that leads to a slower growth and finally a smaller size [76].

All the AuNP synthesis methods presented above are part of the “bottom up” approaches. There is also the “top down” method in which strong forces break down the bulk gold [55]. The AuNPs synthesis by pulsed laser ablation belongs to the latter approach. Elsayed generated AuNPs by laser ablation of a gold plate in de-ionized water [77]. The gold plate was irradiated with a ND:YAG nanosecond pulsed laser. The gold nanoparticle size and hence colloidal properties are controlled by varying the laser parameters such as fluence, wavelength as well as the focusing conditions [77]. Even though this technique has the advantage of a simple procedure, no reducing agents are used and the NPs can be generated in various liquids, it produces AuNPs with a broaden size distribution [77].

As can be seen, obtaining control over the size and shape of the AuNPs is a topic that raised interest in the scientific community. The optical properties (LSPR) of AuNPs depend on their size and shape, and implicitly various applications that rely on these properties are developed. Thus, each synthesis method has its specific reaction conditions that influence these two parameters, but

overall it can be stated that the most important parameters that influence the size and shape of the AuNPs are:

- the nature and the concentration of the capping ligand
- the ratio between the gold salt and the reducing agent concentration
- the ratio between the gold salt and the NPs stabilizer
- the irradiation time and power
- pH of the aqueous solution
- laser parameters: fluence, wavelength and the varying focusing conditions

A schematic representation of the most important AuNP synthesis methods that presents the different characteristics (size and shape) of the final product for various stabilizing agents, reducing agents, synthesis methods and reaction temperatures are given in Table 1.

Table 1. Most important AuNP synthesis methods

	Synthesis method	Reduction Mechanism	Reaction Media	Reducing Agent	Surface Protecting Agent	AuNP Size Range	Shape	Reaction Temperature
Frens	chemical	electrochemical potential difference	Aqueous	Sodium citrate	Sodium citrate	16-50 nm	Spherical	100 °C
Perrault	Chemical/ seed growth	electrochemical potential difference	Aqueous	Hidroquinone	Sodium citrate	50-200 nm	Spherical	Room temperature
Jana	Chemical/step by step seed growth	electrochemical potential difference	Aqueous	Borohydride (for AuNP seeds) Ascorbic acid (for AuNP growth)	Sodium citrate (for AuNP seeds) Ascorbic acid (for AuNP growth)	Au Seeds 3-4 nm AuNP 5-40 nm	Spherical	Room temperature
Jana	Chemical/ Seed mediated growth using rod shaped micellar template	electrochemical potential difference	Aqueous	Ascorbic acid (for NR)	Ascorbic acid	Aspect ratio of 1.5, 2.4, 6.1, 8.0 ad 10.0	nanorods	Room temperature
Brust& Schiffrin	Chemical/ two phase synthesis	electrochemical potential difference	Organic	Borohydride	dodecanethiol	1-3 nm	Mixture of particle shapes	Room temperature
Nikoobakht	Chemical/ seed growth	electrochemical potential difference	Aqueous	Ascorbic acid	CTAB	Aspect ratio of 1.5-5;	nanorods	Room temperature
					CTAB and BDAC	Aspect ratio of 5.5-10; (width from 6-14 nm)		
Martin	Chemical/ two phase synthesis	electrochemical potential difference	Aqueous	Borohydride	dodecanethiol	3-5 nm	Sherical	Room temperature
Kim	Chemical	electrochemical potential difference	Aqueous	Borohydride	Thiol functionalized ionic liquids	3-5 nm	Spherical	Room temperature
Elsayed	Laser Ablation	-	aqueous	-	water	9-20 nm	Spherical	Room temperature

Carruso	Sonochemical	radicals generated from solvents or other reagents	aqueous	-	Metanol Etanol n Propanol n Butanol n Pentanol	12 - 23 nm	Spherical	Room temperature
Henglein	Radiolytic/ radiolytic growth	hydrated electrons or active radicals generation from solvents or other reagents	aqueous	-	PVA	1.5-53 nm	Spherical	Room temperature
Seoudi	Photochemical	direct reduction of the metal salt or radicals generation from solvents or other reagents from the metal precursors	aqueous	Borohydride	PVP	34-60 nm		Room temperature
Zhou	Photochemical	direct reduction of the metal salt or radicals generation from solvents or other reagents from the metal precursors	aqueous	-	PVA	15-25 nm	triangles	Room temperature
Yu	Electrochemical	direct reduction by applying a negative potential	aqueous	-	CTAB	Mean transverse diameter 10 nm	Nanorods	38 °C
Liu	Microwave - assisted	organic reducing agents heated by microwave irradiation	aqueous	Sodium citrate	Sodium citrate	15-90 nm	Spherical	125 °C

1.3.3 Nucleation and growth

As presented above, there are numerous AuNP generation methods which lead to different NP dimensions due to the influence of various synthesis parameters. It is generally accepted that the generation process of these NPs consists of a nucleation and a growth process and that the size of the AuNP is controlled by the rates of these two steps. The formation of AuNP is described by different theories such as LaMer mechanism [78,79], Ostwald ripening [79,80], digestive ripening mechanism, Finke-Watzky two step mechanism [79] or the interparticle growth mechanism [79]. LaMer stated that in a first step the Au^{3+} reduces to Au^0 until the monomer concentration reaches a certain value (critical supersaturation level) at which the nucleation activation energy is overcome and the process of burst nucleation begins (step 2). In the third step the Au^0 concentration drops and so, the nucleation process ends. Finally, the monomers diffuse through the solution and thus, the growth of the AuNPs occurs [78,79].

The Ostwald ripening mechanism states that there is a critical radius (r_{critical}) over which NP grow. Due to the NP high solubility, the particles that are smaller than this critical value redissolve, allowing larger AuNPs to grow even more. Regarding the digestive ripening, the surface energy of the NPs controls the growth mechanism and so the larger AuNPs redissolve, smaller NPs being the ones who, in turn, grow [79].

Finke-Watzky mechanism claims that both steps (nucleation and growth) happen simultaneously due to the fact that the nucleation is a continuous slow process. In this mechanism, the surface growth is proposed to be an autocatalytic process [79].

The interparticle growth method describes the phenomenon in terms of surface energy instability. In this respect, the high energy facets dissolve, whereas the low energy facets will increase in size, phenomena that leads to an apparent interparticle diffusion [79].

Besides this theories, there are several other articles that try to explain this phenomenon. In this regard, the formation mechanisms proposed by Polte are worth mentioning [78]. In this study, the AuNP formation mechanism for two different synthesis methods are presented: the first method refers to the AuNP synthesis that uses sodium borohydride as a reducing agent and the second method refers to the AuNP synthesis that uses sodium citrate (Turkevich method) as a reducing agent.

The difference between the two methods is the strength of the reducing agent (NaBH_4 is a much stronger reducing agent than the sodium citrate). Thereby, the formation mechanism that implies sodium borohydride can be divided in three steps. In the first step, a rapid reduction of the gold ions occurs, followed by the formation of dimers and small clusters (step 2). The last step is characterized by the aggregation and coalescence of the small clusters, step in which the final particle size is established. The AuNP aggregation is due to an insufficient colloidal stability, phenomenon which determines the metallic NP size.

The Turkevich AuNP synthesis mechanism consists of four steps. The first step is characterized by a high reduction rate which is correlated with the formation of small NP (1-2 nm). In step 2, the reduction continues and the formed NPs start to grow due to coalescence, thus decreasing the number of particles. The colloidal stability and the amount of Au^0 are the two factors that determine the number of AuNPs for this first two steps. The growth due to coalescence is followed by the growth of AuNPs due to diffusion (step 3) which is further followed by a tremendous increase in the Au^{3+} reduction rate that is attributed to an autocatalytic surface reduction. In this case, the final size of the AuNPs is determined by the size of the AuNPs seeds obtained in the first two steps. This AuNP dimension influences the number of the AuNPs on which the gold precursor is autocatalytically reduced, consequently determining the final AuNP size [78].

1.3.4 Applications

Properties like high surface to volume ratio, excellent biocompatibility, ease in synthesis and functionalization, excellent conductivity and size, shape and surrounding medium dependent SPR band make AuNP to be extensively studied in a wide range of applications (Figure 5). It is important to state that the AuNPs optical properties on which these applications are based are size and shape dependent.

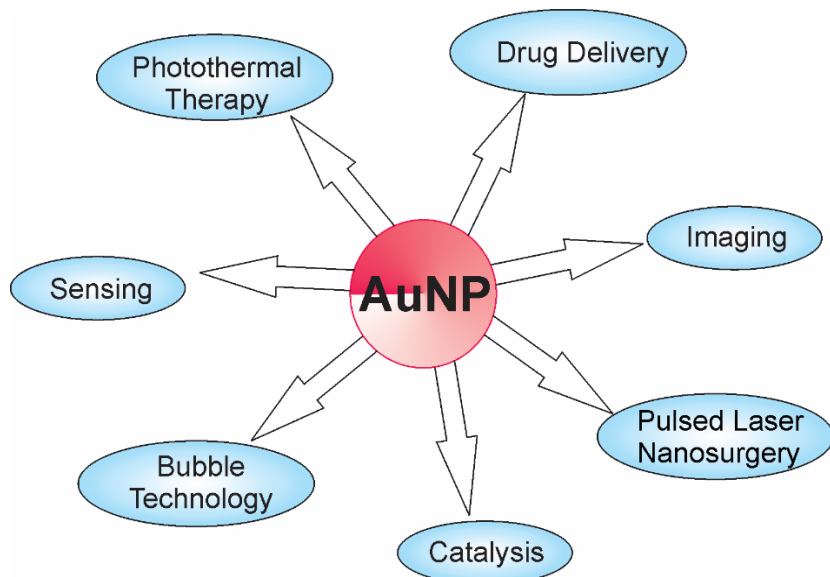


Figure 5. AuNP applications

In sensing, a detectable response signal is produced when the binding between the AuNP and the analyte alters the following three physicochemical properties: LSPR absorption, AuNP conductivity or their redox behavior. Based on this attributes, researchers developed sensing strategies that have an enhanced selectivity, sensitivity and stability [50]. Thus, colorimetric sensors rely on red to blue color changes that are induced by any target analyte that causes the AuNP aggregation or redispersion [50]. Glucose [81] or adrenaline [82] are just a few examples of important molecules that are detected using this technique and have an enhanced dynamic sensing range.

Chemiresistors are devices that have a film of protected AuNP whose electronic properties can be tuned by varying the AuNP size, surrounding medium or the surface functionality. Based on this sensing technique, Wohltjen et al can detect toluene and tetrachloroethylene with a detection limit of 1 ppm [83]. For this purpose they used a film of 2 nm AuNPs coated with octanethiol. The presence of the analyte caused the swelling of the film and thus a rapid decrease in the conductance is observed [83].

Sensors that are based on a change in the LSPR absorption, signal amplification and AuNP plasmon resonance scattering are widely developed. As a general principle, when the AuNPs are functionalized with various analytes the LSPR absorption maxima shifts. Moreover, the sensitivity of the sensor can be increased by increasing the intensity of the absorption band which depends on the size, shape and AuNPs surrounding medium. In addition to the LSPR absorption changes, the

plasmon scattering of larger AuNPs (around 36 nm) is observed to be much stronger than quantum dots or dyes, thus this property is also exploited for sensors design [50].

In addition to the examples presented above, AuNP based sensors enhance the detection sensitivity and selectivity for many other analytes such as: metal ions (Pb^{2+} , Cd^{2+} , Hg^{2+} and Al^{3+}), nucleic acids, proteins, malignant cells, toxic chemicals (arsenic, mercury, and antimony) and drugs (paracetamol, prednisone) [50].

In imaging, the enhanced radiative properties like light absorption, light scattering and fluorescence are exploited. For cellular and in vivo imaging, spherical AuNPs that have larger sizes (above 10 nm), nanorods, nanostars or nanocages are preferred due to the fact that they have strong scattering efficiencies [51]. For cellular imaging, especially for cancer imaging, the dark field optical microscopy is the most common used technique [51].

Photothermal (PT) and photoacoustic (PA) imaging are techniques in which AuNPs are viewed as promising contrast agents because of their ability to absorb and scatter light. Both methods rely on the use of lasers to cause local heating of various materials. The photothermal imaging method directly detects the generated heat, while the PA detects the acoustic waves that are generated by the thermal expansion of air that surrounds the medium [51]. Therefore, PT imaging is based on the AuNP enhanced light absorption, so small metallic NP (NP down to 2 nm) are used, whereas PA imaging relies on the scattering property and thus uses larger AuNP [51]. The most common application for this type of imaging is in cancer detection [51].

Besides imaging, the AuNPs property to generate heat due to light absorption is exploited in photothermal therapy. Cancer cells, bacteria or viruses are destroyed due to the heat generated by the laser irradiated AuNPs. The temperature control in such systems is critical and it can be done by varying the laser parameters (irradiation time and intensity) or by choosing the proper size and shape of the AuNPs [51].

Drug delivery is another important application in which AuNPs serve as carriers for small drug molecules, proteins, DNA or RNA. There are two efficient ways to release of the “payload”: i) a biologically controlled release manner that uses internal stimuli (difference in glutathione concentration or pH values) and ii) a spatio-temporal controlled release that uses light as an external stimuli [6]. The AuNPs are chosen as delivery vehicles because:

- the AuNPs have a high surface area that provides sites for the loading of therapeutic agents [6,51],

- the easiness in functionalizing the NPs surface with the targeting ligand [6,51],
- the wide range of diameters and shapes with which the AuNPs can be synthesized [6],
- the generation of heat when irradiated with a laser, property that can trigger the therapeutic agent release at the desired place [6,51],
- the loading and release events can be observed by fluorescence microscopy (if the drug is fluorescent) or by surface enhanced Raman spectroscopy [51].

For in vivo targeting, Bergen et al studied various sizes (50 nm, 80 nm, 100 nm and 150 nm) of galactose PEGylated AuNPs (Gal-PEG-AuNPs) for hepatocytes specific targeting [84]. He observed that 50 nm Gal-PEG-AuNPs provide a better cell targeting [84]. Likewise, Chithrani observed that spherical 50 nm AuNPs are faster internalized by the mammalian cells [85].

2. Part A – Synthesis, characterization and modeling of the gold nanoparticles photochemical generation process

2.1 Introduction

As described in the introduction, the AuNPs can be synthesized by using chemical methods that involve the use of various reagents such as sodium citrate or borohydride or by physical methods that use UV light, microwaves or ultrasonic waves as energy sources. The photochemical method, which is based on the use of UV light to generate AuNPs, is frequently used in the literature due to its possibility to synthesize AuNPs in various mediums (different polymers, glasses) and have control over the reducing agents generation. Furthermore, the variation of the synthesis conditions can lead to generation of different AuNPs shapes and sizes. The possibility of tuning the AuNP size and shape implies the tuning of the AuNPs optical properties which is important for applications like sensing, imaging or cancer therapy.

The metallic nanoparticle size distribution can be determined experimentally by using techniques like transmission electron microscopy (TEM), atomic force microscopy (AFM), X-ray diffraction or small angle X-ray Scattering (SAXS). Furthermore, a correlation between the determined LSPR absorption maxima and the AuNP dimension can be made [86]. There are also a few papers that use mathematical modelling to determine the AuNPs size [87]. Thus, Kumar et al develops a model that determines the AuNPs size in case of the Turkevich synthesis method in which the metallic NPs are formed due to the chemical reduction of HAuCl_4 with trisodium citrate. This approach assumes that the trisodium citrate is oxidized to dicarboxi acetone and reduces Au^{3+} to Au^+ . The dicarboxi acetone forms a multimolecular complex with Au^+ . The Au atoms and further, the nuclei, form when the complex undergoes disproportionation. Also due to the reaction's high temperatures, the dicarboxi acetone decomposes to acetone. The gold nanoparticle size is influenced by the equilibrium between the degradation of dicarboxi acetone and the formation of Au nuclei. For modelling this complex process and, in particular, to estimate the AuNPs size and density, Kumar uses the population balance equation. This model assumes that the AuNP density depends on: 1) the convective growth process that is caused by the AuNP surface reaction, 2) the Brownian collision frequency 3) the coalescence efficiency and 4) the generation rate of NPs that have a certain size. Based on this model, the influence of the ratio between the trisodium citrate and the HAuCl_4 concentrations is investigated [87].

Tim et al studied the kinetics of AuNP that are synthesized by using an aqueous solution of potassium tetrachloroaurate, trisodium citrate. For inducing the aggregation a concentrated solution of ethanolic solution of benzyl mercaptan was used. The DLVO classical theory is used to describe the AuNPs aggregation and the Monte-Carlo method is used to model the AuNPs aggregation kinetics and to estimate the time needed for the first color modification of the AuNPs. The model calculates an aggregation probability that is defined as the ratio between the aggregation rate between particles i and j and the maximum aggregation rate. The aggregation rate is defined as the ratio between the Brownian aggregation and the stability ratio, the later describing the interparticle interaction effect on the aggregation rate [88].

Sapogova and Bityurin model the size distribution of AuNPs that are generated in a PMMA matrix due to UV irradiation followed by 44 minutes of annealing at 65 °C. Experimentally it is shown that only the particle density is influenced by annealing, whereas the particle size does not modify. Thus the mathematical model that describes the particle distribution takes into account the probability of ceasing the particle growth. Experimentally this phenomenon is attributed to a chemical effect of the PMMA molecules on the AuNPs surface [89].

One of the difficulties with modelling the AuNPs size distribution is that scientist have different opinions with respect to the formation mechanism. Regarding the chemical synthesis, LaMer model and its modifications is being commonly accepted, but recent articles that use time resolved experimental investigations, suggest that the formation mechanisms depends on the used reducing agent. In addition, the formation mechanism for photochemical generation of AuNP or other types of synthesis methods are not well studied, thus the influence of parameters like irradiation power, irradiation time, or polymer concentration on the formation mechanism is not well known.

Thereby, from my knowledge, there is no mathematical model that takes into account all the parameter that influence the formation of AuNP. In addition, a general trial and error approach is used for obtaining AuNPs of a desired size.

The importance of developing a model that is able to predict the metallic NPs dimension is demonstrated by the numerous size dependent AuNP applications, some of them being described in the introduction.

In this view, artificial neural networks (ANNs) are one of the tools that are designed for prediction purposes and are capable of modelling such complex and nonlinear problems. Moreover, this high speed mathematical models require no mathematical expressions for describing the explored

phenomena, being developed on the basis of a finite number of input-output experimental data pairs.

Besides prediction, these models are also used for solving various problems like classification, identification, system control and pattern recognition. Therefore, due to their capabilities, the ANNs are commonly encountered in diverse domains such as medicine, engineering, food and science technology, chemistry or biology.

The aim of this subsection is to develop an artificial neural network that, based on the most influential AuNP synthesis parameters, is able to predict the particles dimension. Moreover, the correlation between these parameters and the NPs size is presented. Also, a hierarchy of the ANN input parameters in terms of their influence over the AuNPs size is studied. The AuNPs are generated in a thick film of poly 4-styrenesulfonic acid (PSS) by a direct light writing method that implies the use of a photo-induced process that has stable and controllable chemical and physical process parameters.

2.2 Experimental

The AuNPs photo-induced synthesis consists of two main parts: 1) the chemical system and 2) the necessary set-up that delivers the radiation within the sample's active layer. The generated AuNPs are then characterized by using spectroscopic and morphologic investigations (transmission electron microscopy (TEM)).

2.2.1 Chemicals

Tetrachloroauric(III) acid trihydrate 99.5% ($\text{AuCl}_4\text{H}\cdot 3\text{H}_2\text{O}$) and tri-sodium citrate dehydrate ($\text{C}_6\text{H}_5\text{Na}_3\text{O}_7\cdot 2\text{H}_2\text{O}$) were purchased from Merck, whereas poly (4-styrenesulfonic acid, 18 wt.% solution in water) (PSS) was purchased from Sigma-Aldrich. All chemicals were of purity grade and used as received.

2.2.2 Instrumentation

The Direct light writing (DLW) set-up (Figure 6) consists of an inverted microscope (BX71, Olympus, Japan), equipped with dry fluorite objectives (10X, 20X and 40X magnifications, 0.3 to 0.75 numerical apertures NA and 0.51 to 10 mm working distances WD), and an XYZ Piezo Stage System with 1 nm resolution (P-545, Physik Instrumente, Germany). The piezo-stage displaces in

a 200 μm range on three axes, runs in a closed-loop regime and has controllable scanning velocities that are set by an appropriate macro.

A 100 W mercury lamp equipped with a longpass filter having the cut-on wavelength at 370 nm, coupled with a dichroic mirror at 410 nm and a barrier filter at 420 nm is used as the radiation source. The radiation is directed into the inverted microscope, thus being focused within the sample. An absorbing neutral density filter (NDF) with 50% attenuation is used to attenuate to half the lamp power.

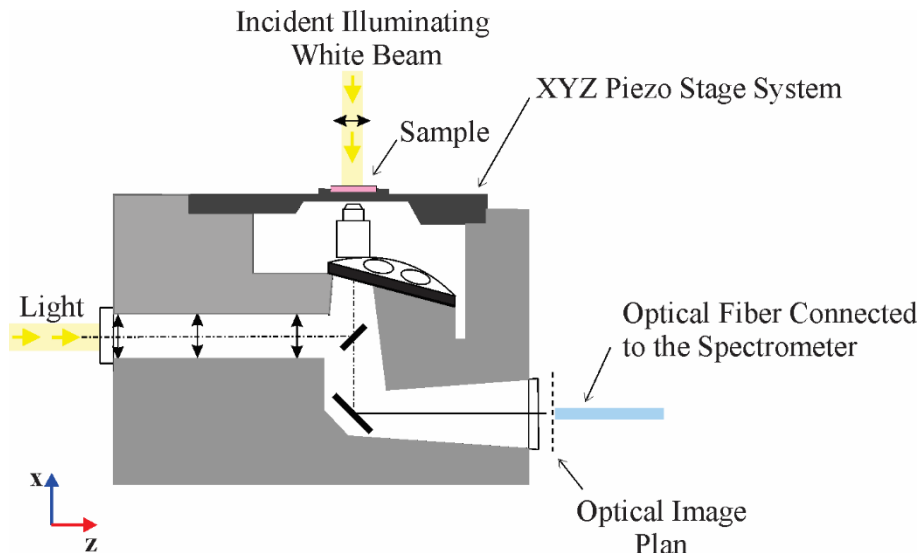


Figure 6. Direct light writing (DLW) set-up [90]

2.2.3 Sample preparation

Two stock solutions that are denoted A1 and A2 and have a concentration of 0.1 mM and 1 mM are prepared as follows: 1 millimole and 0.1 millimole of tri-sodium citrate dihydrate are added to 1 ml of PSS. Also a 1 millimole of $\text{AuCl}_4\text{H}\cdot 3\text{H}_2\text{O}$ (denoted Au^{3+}) is added to 1 ml PSS to obtain a 1mM stock solution of tetrachloroauric acid trihydrate (B).

Before the experiment, an equal volume from the stock solution A1 and A2, respectively, is mixed with the same volume of stock solution B, thus obtaining two solutions denoted A1-B and A2-B. The molar ratio of sodium citrate: Au^{3+} is denoted c_1 in case of the A1-B solution and has a value of 1, whereas the sodium citrate: Au^{3+} molar ratio is denoted c_2 for the A2-B solution and is almost ten times bigger than c_1 .

A single 20 μl droplet of A1-B and A2-B prepared solutions is then applied onto a glass slide, obtaining a uniformly spread thick film.

The prepared samples are placed in the DLW set-up, which is being controlled by a computer, and allows their translation to the focal point. For these experiments 12 scanning velocities of 2, 3, 5, 8, 10, 15, 20, 25, 30, 40, 60 and 80 $\mu\text{m/s}$ are used along with a radiation power of 100 W (P1) and 50 W (P2). The light focused in the sample has a spot diameter that depends on the objectives magnification as follows: 557 μm (10X), 281 μm (20X), and 139 μm (40X).

It is important to mention that the process is selective meaning that it only takes place at the sample's focal plan, in a limited volume and that it occurs under ambient conditions.

For this work, the piezo-stage travels on a length of 180 μm , thus generating thread-like gold patters that, depending on the velocity, will have irradiation times that vary from 94 seconds (2 $\mu\text{m/s}$) to 2 seconds (80 $\mu\text{m/s}$).

2.2.4 Characterization technique

A 12.8 MPixel CCD camera color/monochrome (DP72, Olympus, Japan), operated through the CellSense software and fitted on the microscope with a C-mount camera adapter (0.63x) was used to record optical images from the samples. The recordings have been done in transmission, in bright field (BF) and at lower magnification (6.3x, 12.6x and 25.2x) using Multiple Image Alignment (MIA) software approach to combine several images into one panorama view having high resolution at the same time.

For the UV-Vis absorption spectra, a HR2000+, Ocean Optics optical fiber spectrometer that works in the wavelength range of 200-1000 nm, at millisecond order integration time is used. The spectral response was directly collected from the irradiated area of the sample by using an optical fiber of 200 μm that is connected to the microscope.

For recording the reference and dark spectra, a glass slide that is the same as those used for the thick film deposition is used.

The TEM measurements were done with a Hitachi HD-2700 scanning transmission electron microscope (STEM), equipped with a cold field emission gun that has a resolution of 0.144 nm and is working at 200 kV acceleration voltage. The Digital Micrograph software from Gatan was used for recording the micrographs and ImageJ open source software was used for the NP size determination.

2.2.5 The influence of the scanning velocity and irradiation power on the sample color

It is known that in an aqueous solution, the AuNPs color changes along with their size modification. Similarly to the aqueous AuNP solution, the color change can also be observed in the yellowish colored, transparent polymer due to the fact that the AuNPs have a color that varies from red to purple to blue. To be able to compare the influence of concentration ratio, scanning velocities and irradiation power with respect to the sample's color, optical images from the samples were recorded. Thus, the color change is highlighted in case of c₂ citrate:Au³⁺ ratio, when the sample is irradiated with both powers P₁ of 100 W (Figure 7a) and, respectively, P₂ of 50 W (Figure 7b) and the light is focused through the 10x objective.

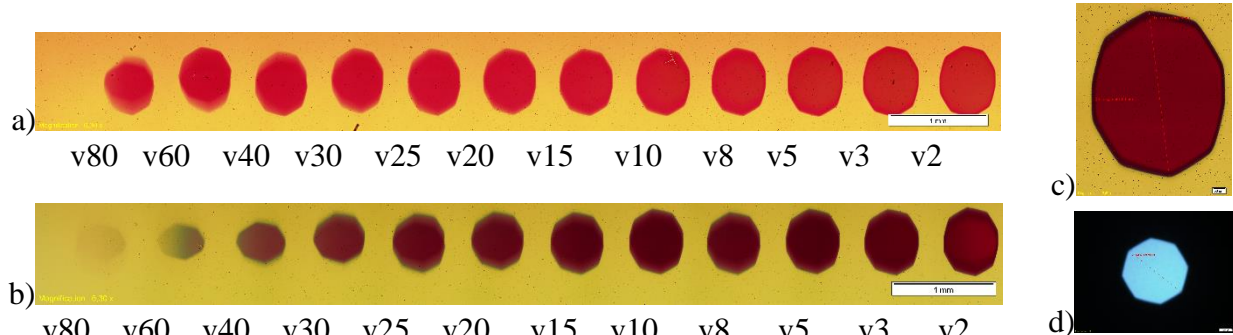


Figure 7. MIA optical microscopy images of two series of thread-like patterns containing gold nanoparticles, recorded in BF at 6.3x magnification, obtained by DLW at increasing scanning velocities from 2 to 80 $\mu\text{m/s}$ from right to left at different powers: a) P₁=100 W; b) P₂=50 W; c) detail recorded at 12.6x magnification. d) Fluorescence optical image of the light spot focused in the sample at magnification 6.3x (557 μm).

From Figure 7 one can observe that in case of the same velocity, the gold patterns color progresses from Chili Red for P₁ power (Figure 7a) to a darker shade Sangria for the lower irradiation power P₂ (Figure 7b). Even though the color has a uniform distribution inside the generated structure, for scanning velocity greater than 15 $\mu\text{m/s}$ the color tends to decrease in intensity at the travel path end. This behavior is especially highlighted in Figure 7b, where the gold patterns color changes from a darker to a lighter shade of red or even a grey color. Thus, by simply analyzing the generated patterns, it is suggested that both the scanning velocity and the irradiation power have an influence on the generated color, the irradiation power having probably a slightly higher influence.

2.2.6 The influence of the scanning velocity and irradiation power on the LSPR absorption maxima

As seen in subsection 2.2.6, the color of the generated gold patters can give quantitative information about the process parameters influence, but for a better description of the process a measurable parameter is needed. In this view, spectroscopy measurements correlated with TEM investigations were done during and after the DLW process, thus obtaining measurable parameters with which the changes inside the irradiated areas can be monitored.

The UV-vis absorption spectra that are presented in Figure 8 are recorded for the citrate: Au^{3+} concentration ratio, for similar scanning velocities, but for P1 and respectively P2 powers. The spectra are recorded in the 450-700 nm range and the 6.3x magnification is kept constant for both measurements.

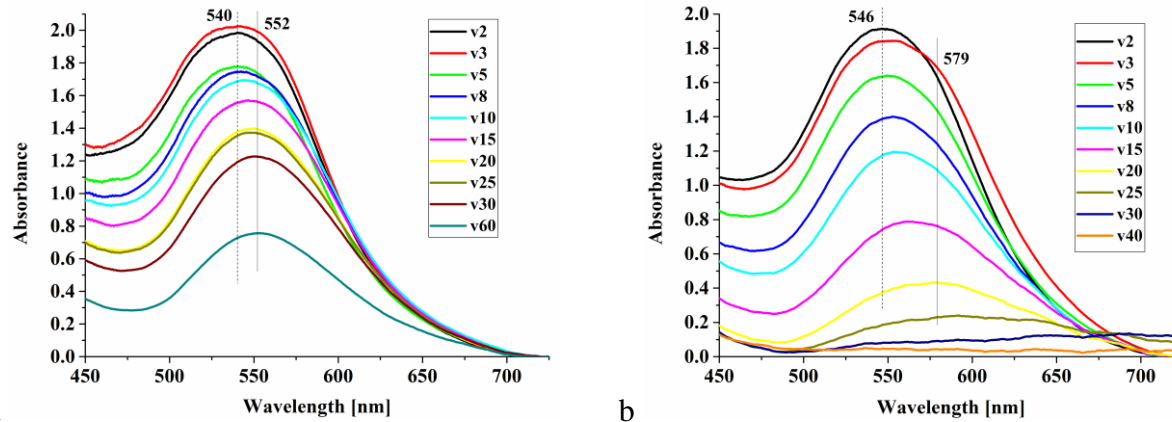


Figure 8. UV-Vis spectra recorded in thick films for two series of gold nanoparticulate patterns obtained at similar scanning velocities, citrate:gold(III) ratio c₂ and 6.3x magnification but different intensities: a. 4.11e4 W/cm²(P1); b. 2.055e4 W/cm²(P2).

In Figure 8 one can seen that the spectra have absorption maxima that are in the range of 540-579 nm, peaks that are specific to gold nanoparticles LSPR. In Figure 8a one can observed that for the same irradiation power of 100 W, the absorption maxima gradually increases from 540 to 552 nm along with increasing the scanning velocity. The same gradual absorption maxima increase that correlates with the rising scanning velocities) is also observed for P2 (50 W) irradiation power (Figure 8b). The difference between the two powers P1 and P2 is that, for P2, higher absorption maxima that are in the range 546-579 nm are measured. The obtained LSPR absorption maxima values could correspond to a broad distribution of AuNPs that exceeds 100 nm limit, but this is true only if the measurements are done in solution. It is known that the AuNPs surrounding medium has an influence on the LSPR absorption maxima, thus the peak values that encounter a

significant red-shift of 12 nm for the power P1 and 33 nm for the power P2 can not be directly estimated from the literature data.

The spectroscopic data presented in Figure 8 a and b show that the generated thread-like gold patters are not continuous structures, but are in fact made up of gold nanoparticles. These DLW gold structures can represent the starting point for the design of different types of materials that have interesting size dependent properties.

As presented in subsection 2.2.3 (Sample Preparation), the experiments are done for 12 scanning velocities (v2, v3, v5, v8, v10, v15, v20, v25, v30, v40, v60 and v80), two irradiation powers and three magnifications – process parameters that are presented in Table 2.

Table 2. Calculated intensities delivered in sample at given magnification/spot size/power

Magnification	Spot size [μm]	Power [W]	Intensity [W/cm^2]
6.3x	557	100 (P1)	4.11e4
		50 (P2)	2.055e4
12.6x	281	100 (P1)	1.611e5
		50 (P2)	8.055e4
25.2x	139	100 (P1)	6.6e5
		50 (P2)	3.3e5

UV-vis measurements are done for all the presented cases and the results are presented in Tables 3 and 4. Consequently, the tables present the variation of the LSPR absorption maxima with the citrate: Au^{3+} ratio, radiation intensity and scanning velocity. The radiation intensity is calculated with the following equation:

$$I = \frac{P}{A_{\text{spot}}}, [\text{W}/\text{m}^2] \quad (13)$$

where $P/[\text{W}]$ is the radiation power and $A_{\text{spot}}/[\text{m}^2]$ is the spot area.

As seen in Equation (13), the radiation intensity is a parameter that depends on the radiation power which is incident on the surface and on the spot area that in turn depends on the objective magnification. Taking into consideration that the light is focused within the sample through different objectives that have increasing magnifications correlated with diminishing spot sizes, at the same power the obtained radiation intensities increases, thus modifying significantly the photochemical response. In this view, the radiation intensity is considered a more relevant parameter, thus being chosen instead of the radiation power.

Table 3. Absorption maxima wavelengths recorded in thick film patterns at given citrate:gold(III) ratio/ intensity/scanning velocity

Citrate:Au ³⁺ ratio	I [W/cm ²]	v [$\mu\text{m/s}$]	LSPR absorption maxima [nm]			
C1	4.11E+04	2	547.45	2.06E+04	2	554.24
		3	550.62		3	554.24
		5	550.62		5	556.04
		8	551.07		8	556.04
		10	551.07		10	566.43
		15	556.5		15	566.43
		20	575.46		20	571.85
		25	577.71		25	578.16
		30	577.71		30	602.46
		40	588.52		40	603.81
		60	588.97			
	1.61E+05	2	546.55	8.06E+04	2	537.94
		3	547		3	537.94
		5	547		5	537.94
		8	547		8	537.94
		10	547		10	537.94
		15	547		15	537.94
		20	547		20	537.94
		25	548.36		25	537.94
		30	548.36		30	537.94
		40	548.36		40	542.47
	6.60E+05	60	549.71		60	549.26
		80	550.17		80	549.71
		2	541	3.30E+05	2	536.13
		3	541		3	537.04
		5	546		5	537.04
		8	546		8	537.94
		10	546		10	537.94
		15	546		15	537.94
		20	547		20	537.94
		25	547		25	537.94
		40	547		30	542.02
		60	548.5		40	544.28
		80	550		60	549.26
					80	550.62

Table 4. Absorption maxima wavelengths recorded in thick film patterns at given citrate:gold(III) ratio/ intensity/scanning velocity

Citrate:Au ³⁺ ratio	I [W/cm ²]	v [μm/s]	LSPR absorption maxima [nm]			
C2	4.11E+04	2	540.21	8.06E+04	5	549.26
		3	540.21		8	552.43
		5	540.21		10	553.33
		8	542.02		15	561.01
		10	543.83		20	578.61
		15	547		2	540.21
		20	548.81		3	541.57
		25	549.26		5	541.57
		30	550.17		10	541.57
		60	551.52		15	542.02
	1.61E+05	3	530.69		20	544.28
		5	530.69		30	547.45
		8	530.69		40	548.36
		10	530.69		60	555.59
		15	530.69		80	558.76
		20	530.69	3.30E+05	2	540.66
		25	543.38		3	541.57
		30	543.38		5	541.57
		40	543.38		8	542.0.
		60	543.38		10	542.02
		80	544.28		15	542.02
	6.60E+05	2	530.69		20	542.02
		3	530.69		25	544.74
		5	530.69		30	546.55
		8	530.69		40	547
		10	530.69		60	552.88
		15	530.69		80	561.47
		20	530.69			
		25	530.69			
		30	530.69			
		40	530.69			
		60	538.85			
		80	543.83			
	2.06E+04	2	546.09			
		3	548.81			

A first observation regarding Tables 3 and 4 is that for the 6.3x magnification, for some higher scanning velocities, powers and citrate: Au^{3+} ratios, AuNPs are not generated resulting in no absorption spectra. Furthermore, it can be observed that in case of the same c2 citrate: Au^{3+} ratio and increasing magnifications (12.6x and 25.2x), the absorption maxima increases from 531 to 544 nm for an intensity of $1.611\text{e}5 \text{ W/cm}^2$ and from 540 to 559 nm for an intensity of $8.055\text{e}4 \text{ W/cm}^2$. Also, the absorption maxima increases from 541 to 550 nm for a $6.6\text{e}5 \text{ W/cm}^2$ intensity and from 541 to 562 nm for an intensity of $3.3\text{e}5 \text{ W/cm}^2$.

It can be observed that the absorption maxima decrease with the increase of the intensity when working at c2 citrate: Au^{3+} ratio and the same magnification.

The absorption recordings have been done, also, in case of the patterns obtained at the lower citrate: Au^{3+} ratio c1 and increasing magnifications (6.3x, 12.6x and 25.2x). Therefore, the absorption maxima increased from 547 to 589 nm for an intensity of $4.11\text{e}4 \text{ W/cm}^2$ and from 554 to 604 nm in case of $2.055\text{e}4 \text{ W/cm}^2$ intensity. Regarding the $1.611\text{e}5 \text{ W/cm}^2$ and $8.055\text{e}4 \text{ W/cm}^2$ intensities, the absorption maxima increased in the range of 547-550 nm and 538-550 nm, respectively. Also, for $6.6\text{e}5 \text{ W/cm}^2$ intensity the absorption maxima increased from 544 to 548 nm, whereas for an intensity of $3.3\text{e}5 \text{ W/cm}^2$ the maxima are situated between 536 and 551 nm. The influence of scanning velocity, citrate: Au^{3+} ratio, magnification and radiation power are highlighted in Figure 9.a,b and c.

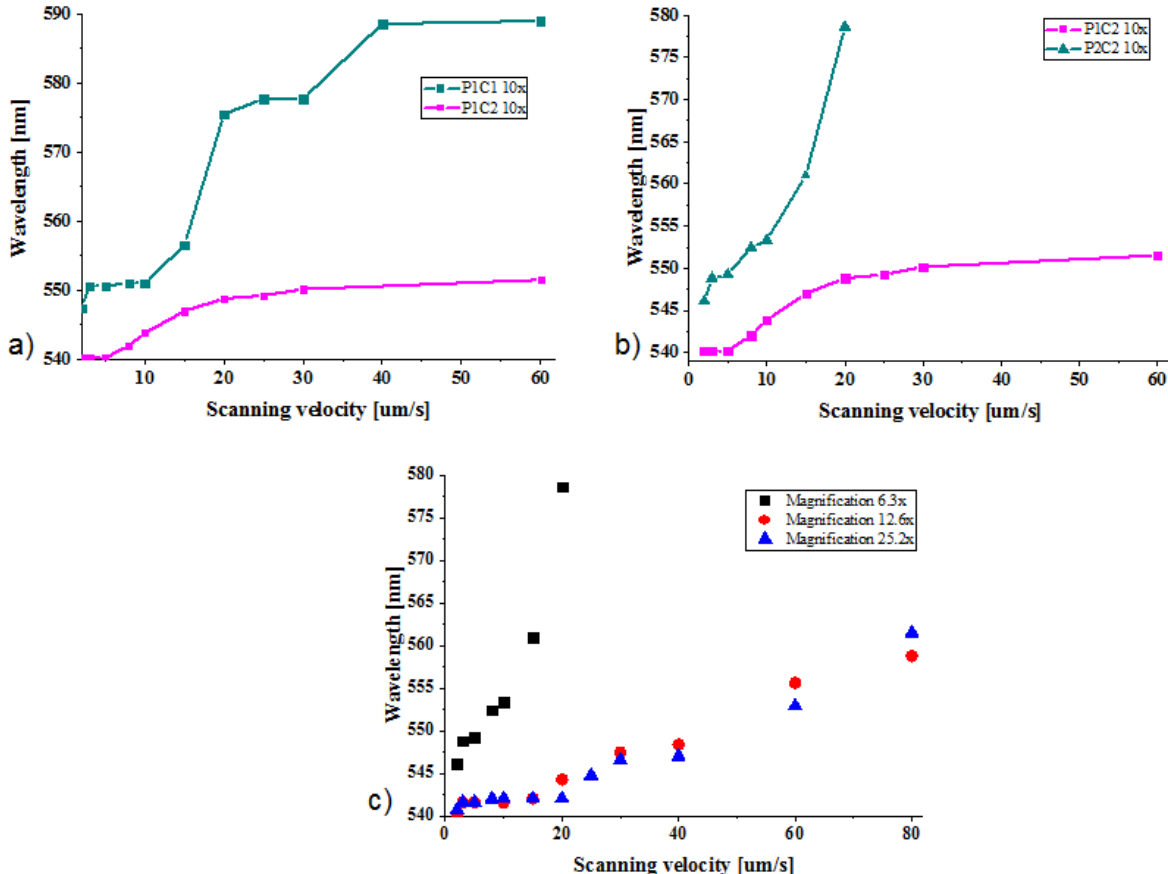


Figure 9. Dependence of the patterns absorption maxima on scanning velocity at: a) increasing citrate:gold(III) ratios (c1 and c2) at the same intensity (4.11×10^4 W/cm 2); b) decreasing intensities (4.11×10^4 and 2.055×10^4 W/cm 2) at the same c2 citrate:gold(III) ratio; c) increasing magnifications (6.3x, 12.6x, 25.2x) at the same power (P2) and c2 citrate:gold(III) ratio.

From Figure 9a one can observe that an increase of the scanning velocity leads to an increase in the LSPR absorption maxima. Also, maintaining the same power of 100 W, a higher citrate: Au^{3+} ratio induces a dramatic decrease of the LSPR absorption peak. This behavior confirms the fact that the citrate anions play the important role of stabilizing the AuNPs against agglomeration. Furthermore, in case of c1 citrate: Au^{3+} ratio, for scanning velocities above 10 μ m/s, a spectacular increase of 25 nm can be observed. A slightly lower raise (15 nm) of the LSPR absorption maxima can be also seen for scanning velocity above 30 μ m/s. Both increases are followed by a “terrace” that is encountered for scanning velocities of 20-30 μ m/s and 40-60 μ m/s. The presence of a “terrace” is more noticeable in case of the higher citrate: Au^{3+} ratio for scanning velocities that are above 20 μ m/s where the LSPR absorption maxima reaches a value of 550 nm. For the scanning

velocities of 2–8 $\mu\text{m/s}$ the absorption maxima have values around 540 nm, the rise being only of 10 nm.

For the same magnification (6.3x) and c₂ citrate:Au³⁺ ratio and for similar velocities, the influence of the radiation power is also studied (Figure 9b). It can be observed that a decrease in the radiation power leads to an almost exponential increase of the LSPR absorption maxima. Additionally, for the same radiation power (P2) and c₂ citrate:Au³⁺ ratio and for similar velocities, the influence of the magnification on the absorption maxima is studied (Figure 9c). A significant LSPR absorption maxima decrease of 34 nm is observed for 6.3x magnification and 12.6x magnifications, whereas a further increase to 25.2x magnification leads to insignificant absorption maxima increase.

Both Figure 9 b and c actually emphasize the decisive influence of the radiation intensity on the LSPR absorption maxima. In Figure 9b the used intensities are 4.11e4 W/cm² for P1 power and 6.3x magnification and 2.055 W/cm² for P2 power and 6.3x magnification, whereas in Figure 9c the intensities are calculated for the same power (P2) and different magnifications, thus having values of 2.055e4 W/cm², 8.055e4 W/cm² and 3.3e5 W/cm². Therefore, a rise in radiation intensity, which can be done by increasing the radiation power or increasing the magnification, leads to an absorption maxima decrease.

The particle size evolution was significantly influenced by the citrate:Au³⁺ ratio, particularly by adjusting the citrate amount as well as by using the PSS polymer matrix as environment for AuNPs generation process. Thus, in our experiment citrate played a double role: on a hand, as photosensitizer which induced the gold(III) cation photoreduction, on the other hand, as protective anion placed at the gold particles surface that protected them against forming larger particles [91–93]. The considerable length of the water-soluble PSS ion-exchange polymer chain as well as the presence of electron withdrawing sulfonyl hydroxide para-substituted styrene units overcome the tendency of agglomeration or aggregation of the already formed AuNPs [94].

2.3 AuNP size determination

The AuNPs size is analyzed by TEM for six samples that are prepared by the same DLW technique, in PSS thick films, with various scanning velocities, magnifications and citrate:Au³⁺ ratios so that the LSPR absorption maxima to be well spread in the studied range. The obtained TEM images along with their histograms are presented in Figure 10. For each histogram more than 500 NP are analyzed and the mean diameter along with the standard deviation are calculated.

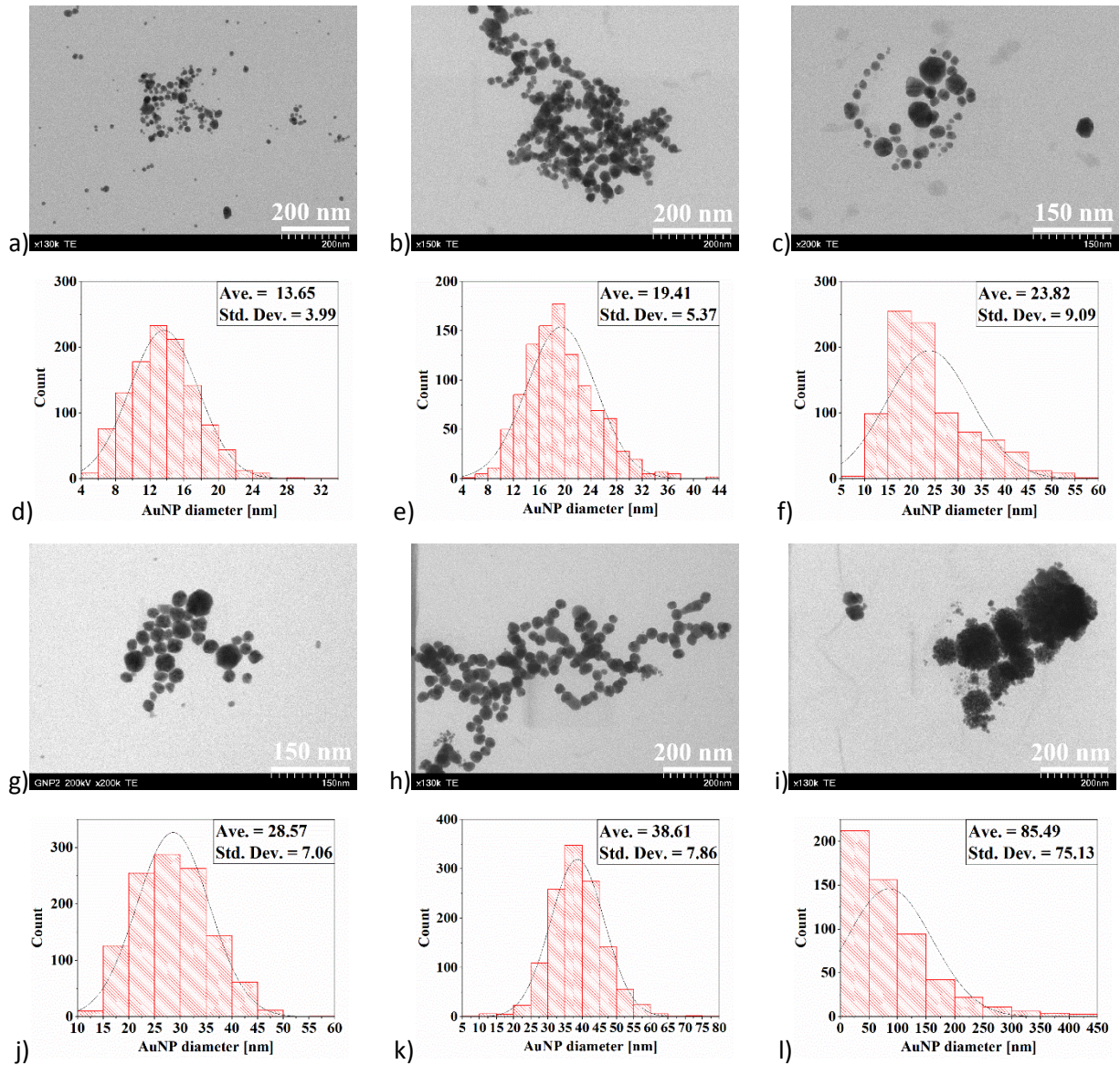


Figure 10(a-c), g-i)) TEM images of AuNPs prepared by DLW in PSS thick films at power/citrate:gold(III) ratio/magnification/scanning velocity conditions of P1c2-6.3x-v2, P1c2-25.2x-v15, P2c1-12.6x-v5, P2c2-6.3x-v2, P2c2-6.3x-v15 and P2c1-6.3x-v30, respectively. (d-f), j-l)) Relation between the particles number (count) and the average particle diameters.

From Figure 10 (a-c, g-i) one can observe that the generated AuNPs have mainly a spherical-like shape, have a relative homogeneous size distribution and are distributed in the broad range of 5 to 80 nm. In particular, the AuNPs that are photosynthesized in P2c1-6.3x-v30 conditions (Figure 10i) have a 5-180 nm range and a flake-like shape. For each of the six samples, the AuNPs number population (count) as a function of the NP diameter is presented in Figure 10 (d-f, j-l). Thus, an average AuNP size of 13.65, 19.41, 23.82, 28.57, 38.61 and 85.49 is determined. The correlation

between these AuNPs average sizes and their attributed absorption maxima are presented in Table 5.

Table 5. The absorption maxima wavelength associated with the TEM measured mean diameters of DLW generated gold nanoparticles in seven thick film samples at the given working conditions.

Absorption maxima wavelength [nm]	Mean Diameter [nm]	Standard Deviation	Intensity [W/cm ²]	DLW conditions
532.5	13.65	3.99	4.1e4	P1c2-6.3x-v2
536.58	19.41	5.37	6.6e5	P1c2-25.2x-v15
541.57	23.82	9.09	8.05e4	P2c1-12.6x-v5
546.09	28.57	7.06	2.053e4	P2c2-6.3x -v2
557.4	38.613	7.86	2.053e4	P2c2-6.3x -v15
653.95	85.49	75.13	2.053e4	P2c1-6.3x -v30

In order to determine the AuNPs real diameter, a correlation between the TEM measured mean diameters (Table 5) from six samples and their absorption maxima that had well distributed values in the studied range (Table 3 and 4) has been done. A similar work that studies the correlation between the absorption maxima measured for an aqueous solution of AuNPs and the NPs average finds an exponential function to fit their data [86]. The difference between the present work and Haiss study is that UV-Vis measurements for the six samples are done directly in the thick PSS film, whereas for Haiss work the LSPR absorption maxima is determined for the aqueous solution of AuNPs. In this view, for the present work, an exponential function is chosen to fit the LSPR absorption maxima as a function of the AuNP size (Figure 11).

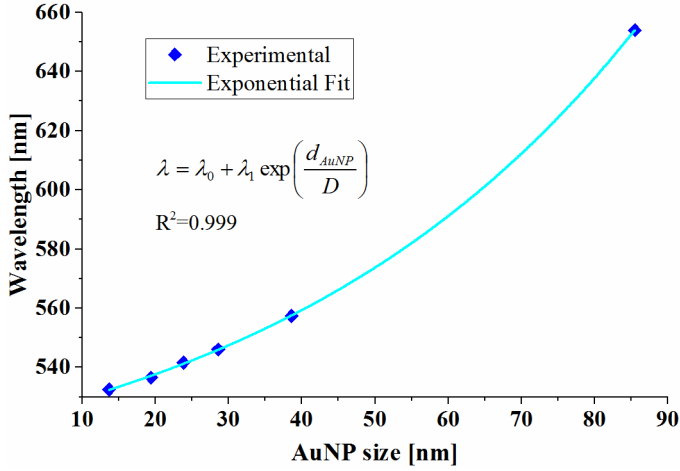


Figure 11. Correlation of the absorption maxima wavelength with the TEM measured mean diameters of DLW generated gold nanoparticles in thick films for experimental along with the fitted curve.

Consequently, knowing the localized LSPR absorption maxim values, the metallic nanoparticles diameter (d_{AuNP}) can be determined using the following equation:

$$d_{AuNP} = D \ln \left(\frac{\lambda - \lambda_0}{\lambda_1} \right) \quad (14)$$

where λ_1 (31.55), D (52.14) and λ_0 (491.36) are the fitting parameters for a correlation factor of 0.999.

2.4 Modeling the AuNP size with ANN

As mentioned earlier, ANNs are ‘black-box’ models developed on a limited number of experimental input-output data and are able to solve linear and non-linear multivariate regression problems [9, 11, 22].

The name of ANN originates from the fact that these type of models work similar with the human brain which is processing information based on the biological neurons and the synapse-connections established between them. The artificial neuron resembles to the biological neuron in terms of structure and functionality [11, 12].

An artificial neuron receives signals from the neighboring neurons, processes these inputs and generates the neuron output. The net signal computed by the artificial neuron is in fact the summation between the weighted input signals received from the neurons located in the previous-neighboring layer and the neuron bias. The activation function is the one that processes the net input of the neuron and generates the neuron output [12, 15].

The computing power of the artificial neuron emerges from connecting together sets of neurons and building an artificial neural network. In the ANN the neurons are organized in layers which consist in groups of artificial neurons having the same activation function. For a typical ANN architecture the connections are only present between neurons of adjacent layers. The ANN becomes a comprehensive computing structure, able to capture any complex relationship between its input and output variables.

For an ANN to learn the proper response to the given input, several learning methods are used, such as the Levenberg-Marquart algorithm, quasi-Newton method, gradient descendent or conjugate gradient algorithm. By training, the ANN values of the weights and biases are adjusted in order to minimize the chosen objective function which usually consists of the mean square error between the desired and the ANN simulated outputs [14, 23].

There are several classes of artificial neural network architectures, classified according to the number of layers, activation function type of the neurons and the configuration of their interconnections, for example: single layer feed forward networks, multilayer feed forward networks and recurrent networks [14].

For prediction purposes, the feed forward backpropagation network is the most efficient ANN model to be trained. The most important and highly appreciated quality of this type of network is its capability to provide a nonlinear solution given to a poorly defined problem, and the ability to approximate any function with a finite number of discontinuities. One of the fastest methods for training the moderate-sized feedforward ANN is the Levenberg-Marquart algorithm, which uses a standard but very efficient numerical optimization technique [12].

As presented in subsections 2.2.6 the three main chemical and physical process parameters that influence the LSPR absorption maxima are the citrate: Au^{3+} ratio, the scanning velocity and the radiation intensity. Thus, the ANN is constructed to have three inputs (the citrate: Au^{3+} ratio, the scanning velocity and the radiation intensity) and one output (LSPR absorption maxima). The data set on which the ANN is based on consists of the 118 experiments that are presented in Tables 3 and 4. Subsequent to the absorption maxima prediction, the AuNPs size is determined by using Equation 11 (subsection 2.3). The schematic representation of the AuNPs size prediction algorithm is presented in Figure 12.

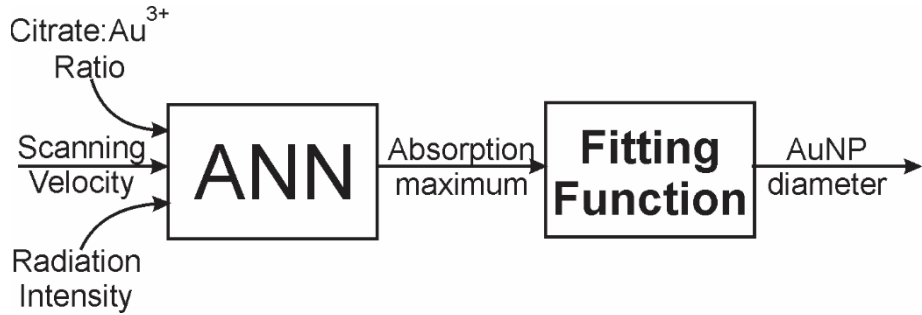


Figure 12. Schematic representations of the artificial neural network and associated fitting function

It is known that selecting the optimum ANN architecture (the number of hidden layers and their corresponding neurons) can be a challenging step. Unfortunately, there is no straightforward method to estimate the best ANN architecture. However, there are studies which claim that a single hidden layer is capable of approximating any function to any degree of accuracy [95–97] and studies which argue that with more than one hidden layer better ANN performances are achieved [98,99]. In this view, the LSPR absorption maxima prediction capabilities were compared for two multilayer feedforward ANN that differ only in structure, having thus one hidden layer (ANN I) and two hidden layers (ANN II), respectively. Both ANNs use the backpropagation training algorithm to compute the weights and biases and the Levenberg-Marquart learning algorithm for training the network. Also, the networks adjust their weights and biases such that to minimize the mean square error (MSE) objective function (Equation 15).

$$MSE = \frac{\sum_{i=1}^{n_p} (x_i - y_i)^2}{n_p} \quad (15)$$

where x_i is the experimental value, y_i is the model predicted value and n_p is the number of data points.

The performance of the two ANNs are evaluated considering the highest Pearson correlation coefficient (R) and the lowest neural network relative error (Rel_{err}).

$$R = \frac{\sum_{i=1}^{n_p} (x_i - \bar{x})(y_i - \bar{y})}{\sqrt{\sum_{i=1}^{n_p} (x_i - \bar{x})^2} \sqrt{\sum_{i=1}^{n_p} (y_i - \bar{y})^2}} \quad (16)$$

where x_i is the experimental value, y_i is the model predicted value, \bar{x} and \bar{y} are the arithmetic mean of the experimental and model predicted values.

$$Rel_{err} = \frac{100(y_i - x_i)}{x_i} \quad (17)$$

Due to the fact that the AuNPs generation process is highly non-linear, the architecture that consists of two hidden layers is first studied.

2.4.1 The ANN model - 2 hidden Layer

With the aim of achieving the desired ANN prediction performance, the overall experimental data set of input and desired output pairs is divided into training, validation and testing data sets as follows. From the sequence of the overall data set every fifth sample is extracted and used for building the testing data set. For the remaining data set the same method is used for generating the validation data set. The remaining data set represents the actual training data set. As a result, the actual training, validation and testing data sets consists of 70, 24 and respectively 24 data sets. Furthermore, in order to enhance accuracy of the training and make it more efficient, the input and output data values are mapped into values ranging within the $[-1, 1]$ interval.

The ANN structure is presented in Figure 13 and consists of one input layer, two hidden layers and one output layer. The number of neurons in each of the hidden layers is found by systematically testing the ANN performance. The best model, which implicitly has the best performance, is chosen from all the trained ANNs that have different combinations of neurons in the hidden layers.

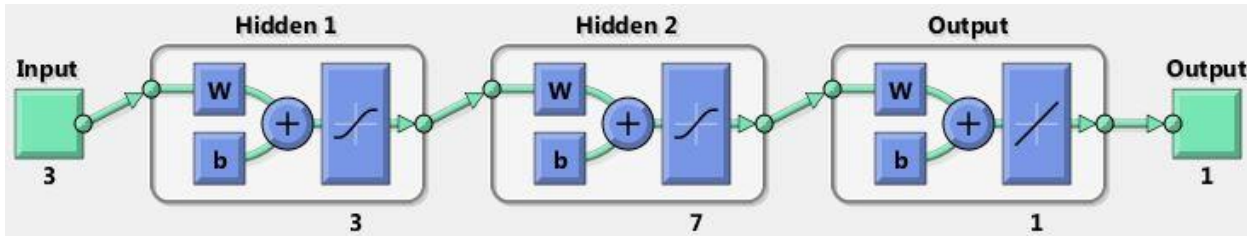


Figure 13. ANN II - Architecture

The tangent sigmoid function (tansig) is used for the hidden layer neurons and, for the output layer, a linear (purelin) transfer function is applied. As presented above, the multilayer feedforward ANN uses the backpropagation training algorithm to compute the weights and biases and, the Levenberg-Marquart learning algorithm for training the network.

2.4.1.1 Statistical assessment of ANN model

Subsequently to performing the training of the designed neural network, the trained ANN model was used to predict the AuNPs dimension. The testing data set, which are unseen by the network during the training step, are used for testing the ANN prediction capabilities.

The best designed and trained ANN has 3 neurons in the first hidden layer and 7 neurons in the second hidden layer, having a good correlation between the predicted and experimental data which is proved by the high values ($R>0.95$) of the Pearson correlation factor. As presented in Figure 14, the ANN has excellent correlation factors of 0.992 and 0.980 and 0.959 for the training, validation and testing data sets. Also the overall data set has a very good correlation factor of 0.978.

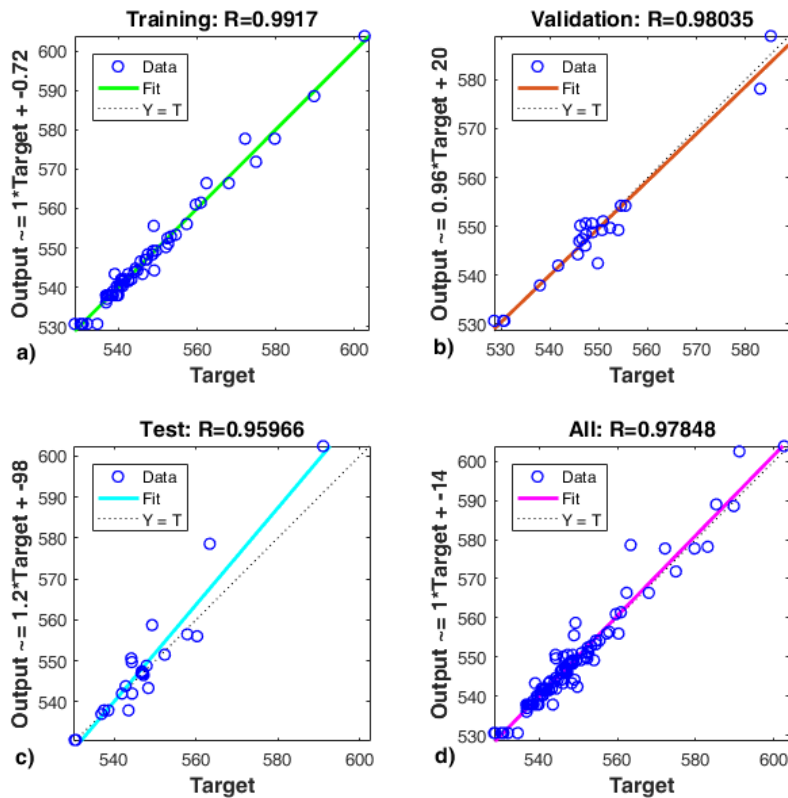


Figure 14. Correlation plots of the ANN model predicted versus experimental values for the: a) training, b) validation, c) testing and d) overall data sets

Besides the Pearson correlation factor, the ANN performance is also evaluated considering the relative error. Thus, the excellent ANN performance is also probed by small relative errors obtained for the testing data set (Figure 15).

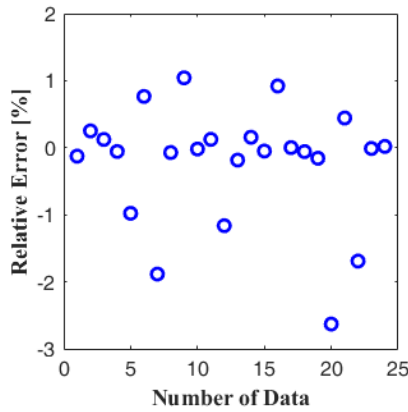


Figure 15. Relative errors between the ANN predicted and experimental values, for the testing data set. Furthermore, the mean and maximum relative errors (in absolute value) are calculated for all the data sets and are presented in Table 6.

Table 6. ANN II - The mean and maximum relative errors (in absolute value) determined for the training, validation and testing data sets

	Mean Relative Error [%]	Maximum Relative Error [%]
Training data set	0.2	1.21
Validation data set	0.33	1.35
Testing data set	0.53	2.62

Thus, from Table 6 one can observe that for the training and validation data sets the maximum relative errors (in absolute value) are 1.21% and 1.35%, whereas the mean relative errors are 0.2% and 0.33%, respectively. Also, even though the testing data set has the highest relative errors, the relative error values are less than 2.65%, indicating an excellent ANN performance.

Therefore, the high correlation factors and the low relative errors demonstrate that the ANN predicted absorption maxima, directly connected with AuNPs diameter, is in good correlation with the experimentally measured value.

2.4.1.2 ANN model Predictions

In the previous subsection the high performance of the ANN II model is demonstrated. As a consequence, new values of the input parameters, values that are different from those obtained in experiments, are further used to predict the AuNPs size. Specifically, the influence of the scanning velocity, radiation intensity, and citrate: Au^{3+} ratio on the AuNPs dimension is studied (Figure 16).

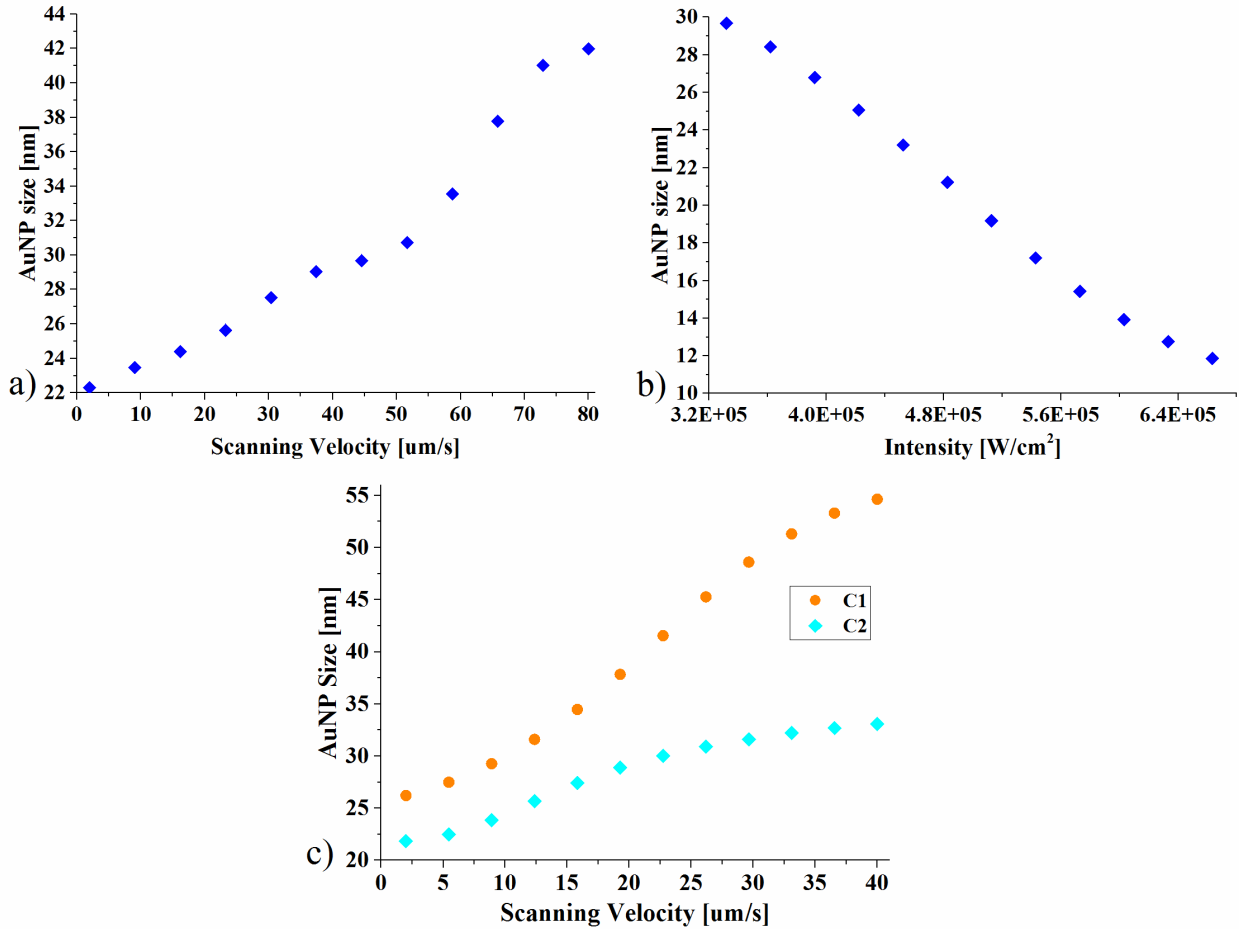


Figure 16. ANN predictions on AuNPs size showing the: a) effect of scanning velocity when ANN is simulated for c2 citrate:gold(III) ratio and an intensity of $3.419e5$ W/cm 2 (P1), b) effect of intensity when ANN is simulated for c2 citrate:gold(III) ratio and a scanning velocity of $40\text{ }\mu\text{m/s}$, and c) trend in AuNP size when citrate:gold(III) ratio changes (c1 and c2), both ANN predictions having an input intensity of $5e4$ W/cm 2

Figure 16 a and b present the influence of the scanning velocity on the AuNPs dimension. For Figure 16a, the used input process parameters are the following: the c2 citrate:Au $^{3+}$ ratio, 12 scanning velocities which have equally spaced values between 2 and $80\text{ }\mu\text{m/s}$ and an intensity of $3.419e5$ W/cm 2 . The intensity is chosen such that its value represents the mean between the minimum ($2.055e4$ W/cm 2) and maximum ($3.3e5$ W/cm 2) experimental intensity values. The intensity in Figure 16c represents the mean between the intensities obtained for the $6.3x$ and $12.5x$ magnifications and P2 power. From this two figures it can be observed that the AuNPs size increases with the increase of the scanning velocity, effect which is more noticeable at higher velocities. Besides the scanning velocity influence, Figure 16c also presents the citrate:Au $^{3+}$ ratio impact on the NPs size. Thus, it can be seen that higher citrate:Au $^{3+}$ ratios lead to bigger AuNPs,

implying that higher Au^{3+} concentrations result in a decrease of the AuNPs dimension. This phenomenon can be explained by an increase in the colloidal stability due to the distribution of the stabilizer around the gold nanoparticle which overcomes their agglomeration [78].

Figure 16b reveals the fact that the AuNPs dimension is also strongly influenced by the radiation intensity. The predictions are made for an average scanning velocity of 40 $\mu\text{m/s}$, the c2 ratio, and 12 equally spaced radiation intensities that are in the range of $3.3\text{e}5$ - $6.6\text{e}5 \text{ W/cm}^2$. Thus, for these process parameters, Figure 16b shows that a radiation intensity increase leads to a decrease of the AuNPs size. This phenomenon can be explained by the fact that at higher irradiation powers the number of nucleation centers rises, thus resulting in a AuNPs size reduction. Also, the decrease of the nanoparticles dimension can be explained considering that already formed AuNPs are excited and further subjected to an ablation process [100].

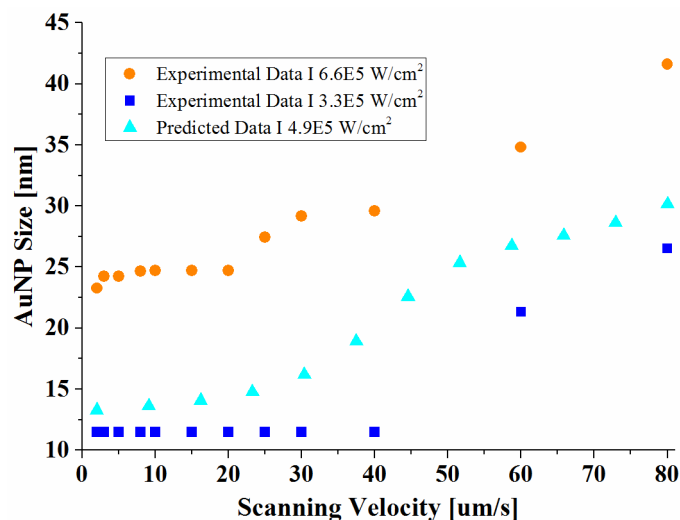


Figure 17. ANN II - predictions showing the interpolation capability of the trained ANN; the predicted data are obtained for c2 ratio and an intensity of $4.9\text{e}5 \text{ W/cm}^2$.

In addition to the model predictions, the trained ANN also has the ability to perform interpolations (Figure 17). The ANN predicted values of the AuNP size are situated between the experimentally measured data of the AuNP size, credibly corresponding to the new input intensity value of $4.9\text{e}5 \text{ W/cm}^2$ which is situated between the experimental input values of $3.3\text{e}5 \text{ W/cm}^2$ and $6.6\text{e}5 \text{ W/cm}^2$.

2.4.2 Assessment of the input variables importance

One of the methods through which the importance of the ANN input variables can be assessed is the use of a feature selection algorithm. This approach finds the subsets of features that optimally predict the experimental data and reveals the features that significantly influence the output. In the first step a generalized linear regression full model of the AuNP size output variable is built considering all three input feature variables and the full matrix of measurements. In the second step an objective function is defined for evaluating the generalized regression reduced models fitted for subsets of the full set of features. Finally, a sequential search algorithm was used for selecting features in the decreasing order of their importance by evaluating the reduced model for each of the feature candidate subset. The deviance of fit for the reduced model is higher compared to the one for the full model and consequently, it was used to order and assess the importance of each feature subsets.

Based on this algorithm, the ANN inputs are ordered according to their importance as follows: the most influential input is the radiation intensity, followed by the scanning velocity and the citrate: Au^{3+} ratio.

2.4.3 The ANN model - 1 hidden Layer

As presented earlier, there are articles that claim that an ANN that has a structure with only one hidden layer is capable of approximating any function to any degree of accuracy [95–97]. Thus, as for the ANN II model, the overall experimental data set of input and desired output pairs is divided into training, validation and testing data. From the sequence of the overall data set every sixth sample is extracted and used for building the testing data set. For the remaining data every fifth sample is uniformly extracted and used for generating the validation data set. The remaining data set represents the actual training data set. As a result, the actual training, validation and testing data sets consists of 78, 20 and, respectively, 20 data sets. Also, as for the ANN II model, the accuracy of the model is enhanced by mapping the input and output data value within the [-1, 1] range.

The ANN structure is presented in Figure 18 and consists of one input layer, one hidden layer and one output layer. The number of neurons in the hidden layers is found by systematically testing the ANN performance. The best model, which implicitly has the best performance, is chosen from all the trained ANNs that have different combinations of neurons in the hidden layer.

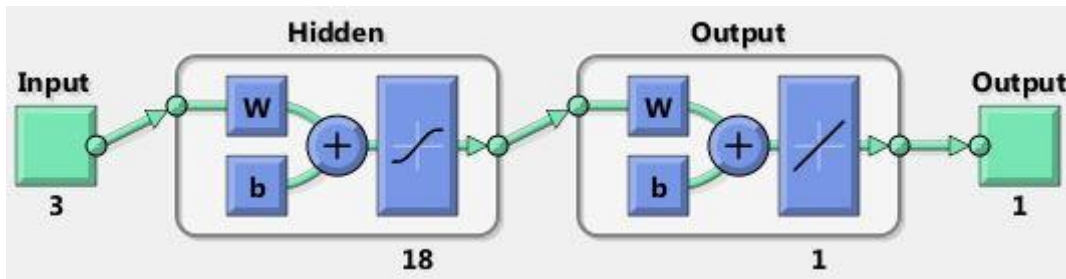


Figure 18. ANN Structure

The tangent sigmoid function (tansig) is used for the hidden layer neurons and, for the output layer, a linear (purelin) transfer function is applied. Also, the ANN I model is designed as a multilayer feedforward network that uses the backpropagation Levenberg-Marquart learning algorithm.

2.4.3.1 Statistical assessment of ANN model

As for the ANN II model, the one hidden layer ANN uses the yet unseen testing set of data for verifying the ANN prediction capabilities. The best designed and trained ANN has 18 neurons in the hidden layer, having an acceptable correlation between the predicted and experimental data which is proved by the high values ($R>0.9$) of the Pearson correlation factor. As presented in Figure 19, the ANN has an excellent correlation factor of 0.99 for the training data set, whereas for the validation and testing data, the correlation factor has acceptable values of 0.92 and 0.96.

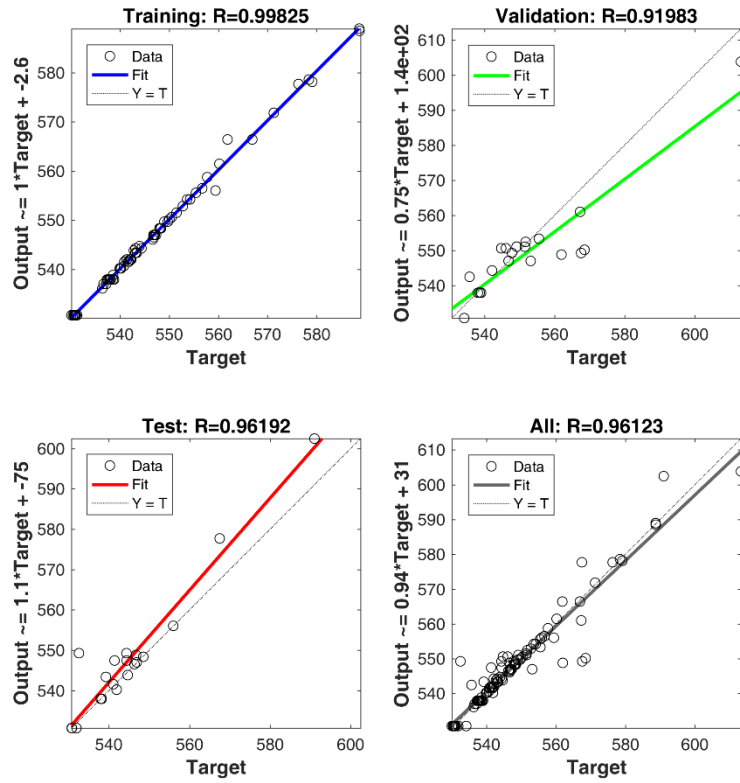


Figure 19. Correlation plots of the ANN model predicted versus experimental values for the: a) training, b) validation, c) testing and d) overall data sets

Besides the Pearson correlation factor, the ANN performance is also evaluated considering the relative error. The good ANN performance is additionally probed by the maximum relative errors (in absolute value) which are less than 3.5%, and also by their less than 1% mean absolute value (Table 7).

Table 7. ANN I - The mean and maximum relative errors (in absolute value) determined for the training, validation and testing data sets

	Mean Relative Error [%]	Maximum Relative Error [%]
Training data set	0.077	0.81
Validation data set	0.93	3.34
Testing data set	0.57	3.039

Comparing the ANN I and ANN II models in terms of performance, one can observe that the best results are obtained for the two hidden layers ANN. Thus, for the ANN I modeling, the influence

of the input parameters on the AuNPs size will not be further investigated. However, the process parameters relative impact on the AuNPs dimension is assessed in the following subsection (2.4.7).

2.4.3.2 The relative impact of each process parameter on the particle size

Apart from the fact that the ANNs are used for interpolation, prediction or classification purposes, scientists are also interested to develop new methods that are able to quantify the contribution of network inputs [101]. The method that exhibits the best performance in terms of accuracy and precision of estimating the importance of all ANN variables is the connection weight partitioning methodology proposed by Garson and Goh [95,101]. Based on this method, the relative importance (RI) of ANN input variables is determined as follows:

$$RI = \frac{\sum_{j=1}^{n_h} [(i_{v_j}/\sum_{k=1}^{n_v} i_{k_j}) h_{o_j}]}{\sum_{i=1}^{n_v} [\sum_{j=1}^{n_h} (i_{v_j}/\sum_{k=1}^{n_v} i_{k_j}) h_{o_j}]} * 100 \quad (18)$$

where i_j is the absolute value of connection weights between the input and the hidden layers, n_v and n_h are the number of neurons in the input and hidden layer, h_{o_j} is the absolute value of connection weights between the hidden and the output layers [95,101].

In this view, for this study, the connection weight partitioning methodology is used for determining the relative importance of the citrate:Au³⁺ ratio, scanning velocity and the radiation intensity on the AuNPs size.

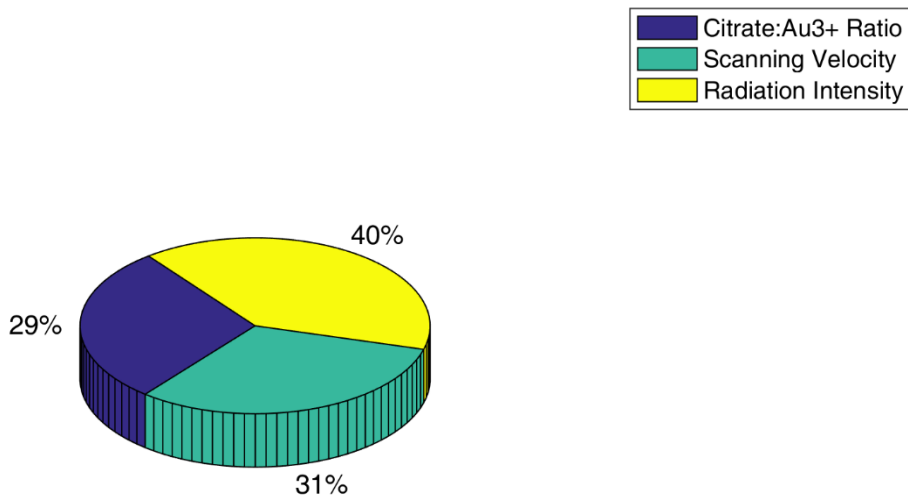


Figure 20. Pie chart showing the relative impact of each process parameter on the AuNPs size

As shown in Figure 20, the radiation intensity has a relative importance of 40%, thus being the factor that most influences the AuNPs size. The scanning velocity and the citrate:Au³⁺ ratio have a similar relative importance, the scanning velocity having a slightly higher value of 31% in

comparison with the citrate:Au³⁺ ratio which has a value of 29%. This results are consistent with those obtained in subsection two, where the same hierarchy regarding the input variables influence is determined.

2.5 Conclusions Part A

In this part, a direct light writing method is used to generate stable and reproducible gold patterns in a polymer thick films. These patterns are generated in the sample, at the focal plane, due to a photochemical process. Thick film spectroscopic investigations showed that the generated thread-like DLW patterns, which exhibited a strong absorption in visible range, were made up of gold nanoparticles instead of being continuous structures.

The influence of citrate:Au³⁺ ratio, radiation intensity and scanning velocity on the thick film SPR absorption maxima, and consequently on the AuNPs size, is studied. It is demonstrated that the SPR absorption maxima increases with decreasing the citrate: Au³⁺ ratio and radiation intensity as well as with increasing the scanning velocity.

The real dimension of the embedded AuNPs can be estimated using an exponential fit that was obtained based on the TEM measured AuNPs mean diameters and their corresponding localized SPR absorption maxima measured in thick film.

Based on the citrate: Au³⁺ ratio, radiation intensity and scanning velocity, parameters which have an important contribution to the AuNPs size, two ANNs that differ in terms of architecture, are developed to predict the localized SPR maxima and therefore the AuNP dimension.

The ANN that has two hidden layers has better prediction capabilities (low relative errors and the high correlation factor between the experimental and the predicted ANN data) than the one hidden layer ANN.

The influence of the input parameters upon the AuNPs size is studied only for the two hidden layers ANN, the observed dependences being in good agreement with the experimental data.

Based on the one hidden layer ANN the Garson and Goh method is used to evaluate the relative impact of each process parameter on the particle size. The results show that the radiation intensity has a relative importance of 40%, being thus the factor that most influences the AuNPs size. The scanning velocity and the citrate:Au³⁺ ratio have a similar relative importance, the scanning velocity having a slightly higher value of 31% in comparison with the citrate:Au³⁺ ratio which has a value of 29%.

The input variable importance is also examined with a feature selection algorithm was used to find the subsets of features that optimally predict the measured data, revealing the features that are most influential. As for the Garson and Goh method, the radiation intensity is found to be the input that influences the most the AuNP size, followed by the scanning velocity and the citrate: Au^{3+} ratio.

3. Part B - Gold Nanoparticles in Laser Fields: Heat Generation and Heat Transfer

3.1 Introduction

As presented in the Introduction, AuNPs are used in applications such as: sensing [50], imaging [51], drug delivery [6] or photothermal therapy [51]. These applications are developed based on the AuNPs property to generate heat when irradiated with visible light, phenomena that leads to a temperature increase both in the nanoparticle and in its surrounding medium. The electric field of the incident radiation polarizes the AuNPs conduction electrons, which generates surface charges that alternatively accumulate on opposite ends of the nanoparticle (phenomenon denoted as LSPR). Because of the NPs oscillating polarization, a restoring force results from the generated electric field that opposes the excitation field. One of the ways by which the oscillation is damped is through heat generation [26–28]. Thus, heat can be seen as an incoherent set of vibrations, which in solids is supported by phonons [27]. Generally, elementary particles like photons, electrons and phonons are responsible for the heat transport. The heat transport mechanism for electrons and phonons is conduction, whereas for photons is radiation [27]. Thus, when AuNPs are exposed to radiation the following phenomena occur, listed below from the fastest to the slowest one:

- a few electrons gain photon energy by absorption, while the others remain in a non-exited state
- the kinetic energy is redistributed among the whole quasi-free electron gas by electron-electron collisions
- the thermal equilibrium between the electrons and the lattice is established by electron – phonon collisions
- at the interface between the NP and the surrounding environment the thermal energy is exchanged through phonon-phonon collisions and as a result the AuNP is cooling down.

The AuNPs and their surrounding medium temperature are determined using both experimental and mathematical modelling methods. The few experimental methods that can estimate the AuNPs temperature are Raman spectroscopy, white light scattering spectroscopy and photoacoustic imaging. Besides these three techniques, a simple method to determine if the irradiated AuNPs produce heat is by using a pH thermo-indicator (thymol blue) dissolved in tris buffer. Being temperature dependent, the tris buffer decreases its ionization constant with the increase of the

temperature, thus its pH will also decrease with the temperature elevation. The pH indicator (thymol blue) changes its color from red to yellow to blue, colors that correspond to the following pH intervals: 1.2 to 2.8, 2.8 to 7.8 and 7.8 to 9.5. So, for temperatures that range between 25 to 90 °C the color of the thymol blue solution changes from blue to yellowish green [102]. Furthermore, Raman spectroscopy, white light scattering spectroscopy and photoacoustic imaging are also techniques used to assess the AuNP temperature.

Raman spectroscopy was used to determine the surface temperature of ice embedded AuNPs [103]. In this case, an ice to water phase transformation occurs due to the heat generated by the AuNPs. Thus, the Raman signal intensity is used to record the ice to water melting process [103]. It is known that the refractive index of a nanomaterial changes with the temperature increase, a phenomenon which can be assessed through the shift of the surface plasmon maxima [104]. Such changes can be measured with white light scattering spectroscopy. In this view, the local temperature of a laser irradiated single nanoparticle can be determined by using this method. For this purpose, gold nanoparticles were coated by a thermo-responsive polymer, poly(N-isopropylacrylamide) (pNIPAM) to determine the surrounding medium to be sensitive to the nanoparticle temperature. Then, the heating effect was monitored by measuring the peak scattering wavelength derived from the surface plasmon of gold nanoparticles, which varied with the refractive index of the surrounding polymer. Finally, the temperatures were calibrated by using a temperature controlled cell to heat a bulk sample of nanoparticles and measuring the temperature dependent peak shift by UV-Vis absorption spectroscopy [105].

Another approach for determining the elevation of AuNPs temperature is the use of photoacoustic imaging. This technique relies on the fact that, when irradiated, AuNPs absorb electromagnetic energy and subsequently emit an acoustic wave which leads to an increase in pressure. This photoacoustic pressure (P) depends on the absorption coefficient, laser fluence and a dimensionless parameter (Grueneisen parameter) which is temperature dependent. Thus, the temperature change is determined based on changes in photoacoustic signal ($\Delta P/P$) amplitude [106,107].

The fact that after the AuNP irradiation, the temperature increase takes place only on a nanometric scale range makes mathematical modelling the most suitable method for NP temperature determination [108]. Furthermore, noninvasive imaging techniques are limited by low sensitivity, penetration or contrast and, in addition, the temperature fields may have an inadequate dynamic mapping temporal resolution [107].

The models that study the temperature of the AuNP and its surrounding medium differ as approach and approximations. For example Baffou et al studies the temperature in a spherical symmetry system that consists of an irradiated AuNP immersed in water. The solution for the heat equation is provided for both a continuous irradiation source and a femtosecond illumination source [109]. Furthermore the temperature profile inside and near the AuNP for different normalized times and different Kapitza lengths is presented. The influence of the AuNP size, the importance of NP surface resistivity and the influence of NP irradiation with tens of pulses is also studied [109]. Letfullin et al [109] is interested in the temperature time dynamics of a system that consists of a AuNP immersed in water that is irradiated with a ns irradiation source. The numerical investigations take into account different NP diameters and shapes (spheres and rods), and various pulse durations, pulse repetition rates and laser energy densities. In all their simulations the systems maximum temperature was limited to the bulk gold melting point ($T \sim 1336$ K) [110]. Thus, extremely high temperatures can be recorded inside and around the AuNPs. In this respect, Sassaroli et al numerically solved the heat equation for a spherical AuNP immersed in water and irradiated with a ns laser pulse. In this model, besides the fact that the vapor formation is taken into account, also gold and water properties like density, specific heat and thermal conductivity are expressed as a function of temperature. Based on their model, the temperature evolution in time of a AuNP and its surrounding medium was calculated for various pulse durations and various intensities [111]. Also, Pustovalov obtained analytic expressions for the temperature of a pulsed laser irradiated spherical AuNP. The model takes into account the fact that the heat conduction coefficient has a nonlinear dependence of temperature [112]. AuNP temperatures of several hundreds of Kelvin degrees were also obtained after pulse laser irradiation by Plech and Kotaidis. In their study, time resolved x-ray spectroscopy was used to resolve lattice changes in water embedded AuNP but also the cooling of the NP surrounding matrix is investigated. They observed that the water matrix is governed not only by the heat conductivity, but also the heat transfer through the interface between the AuNP and its surrounding matrix should be taken into account. Thus, an interface conductance (G) value of 105 ± 15 MW/(m²K) is deduced [113]. Regarding the fs laser irradiation of AuNPs, the electron thermalization should be also taken into account due to the fact that the electron-electron scattering takes place on a time scale of fs (same as the laser irradiation). Rashidi-Huyeh and Palpant modeled the temperature dynamics for the electron, lattice and surrounding matrix of a fs laser irradiated spherical AuNP. The heat generation in NP of

various dimensions, different surrounding environments (SiO_2 , Al_2O_3) and variable gold concentrations was also modeled [114].

The temperature of a system that consists AuNPs embedded in a surrounding matrix can also be influenced by the matrix material properties. For example Smirnov studied the heating of AuNPs in a PMMA matrix [115], while other scientists investigated non-homogeneous medium [116] or human tissue [117]. The last two mediums were investigated due to the importance of studying the heat generated by laser irradiated AuNPs in the case of cancer treatment due to hyperthermia.

A relevant study in this field was made by Ren [117] who modeled the heat generated by tissue embedded AuNPs. In this approach the systems temperature is modeled with Pennes bioheat equation in which the AuNPs were introduced as volumetric heat sources and their heat was calculated in a previous step through Monte Carlo method and Beer's law. The influence of the tissue aspect ratio, the AuNPs volume fraction, the laser irradiated area and the importance of period heating are aspects that were also tackled [117].

The above presented mathematical models investigate various factors that influence the AuNP temperature. Such as the AuNP size, the laser pulse profile, temperature dependent material parameters or the existence of an interface between the AuNP and its surrounding medium. Most mathematical models restrict their study to only one gold nanoparticle that has water as a surrounding medium.

The aim of this part of the thesis is to mathematically model the temperature dynamics in a laser irradiated system that consists of many AuNPs surrounded by a polymer matrix. The influence of particle size, number and the displacement of particles in the surrounding matrix on the gold nanoparticles temperature dynamics is studied. A comparison between the large infinite system that has AuNPs dispersed in a random geometry and the one that contains only one AuNP is also performed. Furthermore, we investigated the non-perfect contact between the AuNPs and the surrounding medium as well as the near-field effects, NP orientation with respect to the electric field polarization and the influence of the distance between AuNP on the heat generation and maximum temperature. Last, but not least, the impact of the modelling approaches on the gold nanoparticles heat generation is considered.

3.2 Temperature dynamics of a system that contains one spherical AuNP embedded in a polymer (PSS) matrix – the influence of AuNP size

3.2.1 Methods

A system that contains only one AuNP embedded in a polymer matrix resembles experimentally with a dilute AuNP solution in which there is a substantial distance between the nanoparticles. Thus, the NP spatial distribution can be neglected when modeling the AuNP heat generation and the temperature distribution in their surrounding medium.

In this view, the aim of this section is to determine the temperature space-time evolution in a ns laser irradiated system (denoted as System I) that contains a spherical AuNP embedded in a polymer polystyrene sulfonic acid (PSS) matrix. Here, the influence of AuNP size is also investigated.

The temperature dynamics in such a system is numerically modeled using the finite element method (FEM) which is implemented in Comsol software. Within this software the Heat Transfer in solids module along with a 2D Axysimetry geometry are chosen. Therefore, the spherical AuNP and its surrounding medium are modeled as two concentric spheres, the entire model having thus a spherical symmetry (Figure 21).

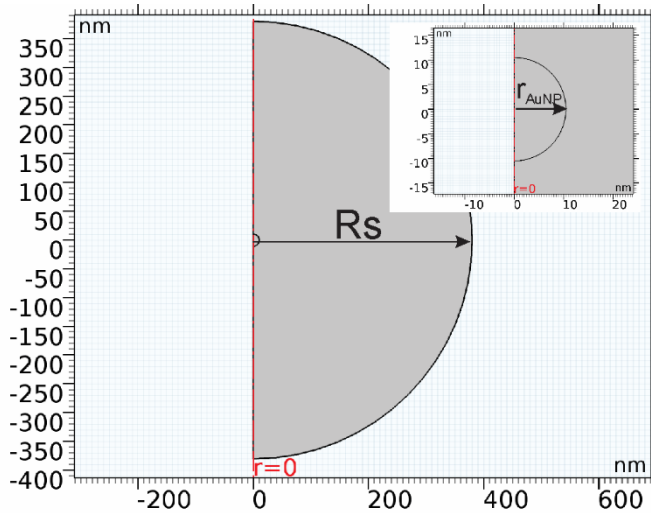


Figure 21. – System's I Geometry

The influence of the AuNP size is investigated for particles that have a radius (r_{AuNP}) of 10, 15 and 20 nm, whereas the entire system has a radius (Rs) of 380 nm in all three cases.

In these three simulations, the irradiation source is considered to be a Nd:YAG nanosecond laser that has a Gaussian pulse of 12 ns FWHM and a 532 nm wavelength. In the NP the electron-

electron and electron-phonon collisions time is 500 fs and 1-5 ps respectively, so that the heat transfer time from the hot electrons to the Au lattice is much shorter than the laser pulse duration. Thus, in the simulations it is assumed that the AuNP is uniformly heated and the heat loss is a result of heat conduction from the metal NP to the polymer surrounding medium. Furthermore, it is also assumed that the PSS matrix is optically transparent to the laser light and that at its exterior boundary, the system is isolated.

The density, heat capacity and thermal conductivity of the polymer matrix (an aqueous solution of 18% wt. PSS) were experimentally determined at INCDTIM and are presented in Table 8. Experimentally, the thermal effusivity (e) and thermal diffusivity (α) were detected at 20 °C using a photopyroelectric technique [118]. These parameters are related to the thermal conductivity (k) and static volume specific heat (C_p) through the following relations: $k = C_p * \alpha$ and $e = (C_p * k)^{1/2}$ [118].

Table 8. Polystyrene sulfonic acid properties at atmospheric pressure and 20 °C

Aqueous PSS matrix	Measurement units	Value
Density (ρ)	kg m^{-3}	1071.5
Heat Capacity (C_p)	$\text{J kg}^{-1} \text{K}^{-1}$	3043.77
Thermal Conductivity (k)	$\text{W m}^{-1} \text{K}^{-1}$	0.45

The AuNP density, heat capacity and thermal conductivity are obtained from the Comsol software material database. Their values are presented in Table 9.

Table 9. AuNP properties at atmospheric pressure and 20 °C

AuNPs	Measurement units	Value
Density (ρ)	kg m^{-3}	19300
Heat Capacity (C_p)	$\text{J kg}^{-1} \text{K}^{-1}$	129
Thermal Conductivity (k)	$\text{W m}^{-1} \text{K}^{-1}$	317

Thus, the heat transfer in system I is described by the following equations:

$$\rho_{AuNP} C_{p_{AuNP}} \frac{\partial T_{AuNP}}{\partial t} = k_{AuNP} \nabla^2 T_{AuNP} + Q, [\text{W/m}^3] \quad (19)$$

inside the NP, and

$$\rho_{PSS} C_{p_{PSS}} \frac{\partial T_{PSS}}{\partial t} = k_{PSS} \nabla^2 T_{PSS}, [\text{W/m}^3] \quad (20)$$

in the surrounding medium. Here ρ is density, C_p is specific heat, k is thermal conductivity, $T/(^0\text{C})$ is the temperature and $Q/(\text{W/m}^3)$ is the heat generated by the AuNP. The AuNP and PSS subscripts refer to the gold nanoparticle and the polystyrene sulfonic matrix.

The heat generated by the AuNP is modeled in Comsol software as a heat source and it is determined based on the following equation:

$$Q = \frac{3K_{abs}If(t)}{4r_{AuNP}}, [\text{W}/\text{m}^3] \quad (21)$$

where K_{abs} is the absorption efficiency, $I/(\text{W cm}^{-2})$ is the laser intensity, $r_{AuNP}/(\text{m})$ is the nanoparticle radius and $f(t)$ is the laser pulse time profile and is described by a Gaussian:

$$f(t) = \exp\left(-\frac{(t - t_0)^2}{\tau^2}\right) \quad (22)$$

where $\tau=12$ ns FWHM is the Gaussian pulse duration and t_0 is the position of the center of the peak.

The absorption efficiency depends on the absorption cross section ($\sigma_{abs}/(\text{nm}^2)$) and can be calculated with the following formula:

$$K_{abs} = \frac{\sigma_{abs}}{\pi r_{AuNP}^2} \quad (23)$$

In this study, the absorption efficiency values are calculated using Lorentz-Mie theory [110]. Within this mathematical model the absorption cross section is determined as follows [109]:

$$\sigma_{abs} = \frac{2\pi}{k^2} \sum_{n=1}^{\infty} (2n + 1) (\lvert a_j \rvert^2 + \lvert b_j \rvert^2), [\text{m}^2] \quad (24)$$

$$a_j = \frac{m\psi_j(\omega)\psi'_j(v) - m\psi_j(v)\psi'_j(\omega)}{m\psi_j(\omega)\xi'_j(v) - \xi_j(v)\psi'_j(\omega)} \quad (25)$$

$$b_j = \frac{\psi_j(\omega)\psi'_j(v) - m\psi_j(v)\psi'_j(\omega)}{\psi_j(\omega)\xi'_j(v) - m\xi_j(v)\psi'_j(\omega)} \quad (26)$$

where $m=\epsilon_{Au}/\epsilon_m$, $v=k_0 * r_{AuNP}$, $\omega=mv$; k_0 is the wavenumber, ψ and ξ are Riccati-Bessel functions and ψ' and ξ' are their derivatives.

The model has the following imposed initial and boundary conditions:

1. Initial conditions:

$$T_{AuNP}(x,y,z,0)=T_{PSS}(x,y,z,0)=20 \ ^\circ\text{C}$$

2. Boundary conditions:

- **Exterior boundary:** $q(R_s,t)=0$, where q is the heat flux
- **Boundary conditions on the particle surface:**

$$T_{AuNP}(r_0,t)=T_{PSS}(r_0,t),$$

$$k_{AuNP} \frac{\partial T_{AuNP}}{\partial r} \Big|_{r=r_{AuNP}} = k_{PSS} \frac{\partial T_{PSS}}{\partial r} \Big|_{r=r_{AuNP}}$$

3.2.2 Results and discussions

As explained earlier, System's I behaviour is described by Equations (19) and (20) and the solution $T(x,t)$ is obtained numerically by FEM method. Three simulations in which the entire system radius remains constant ($R_s = 380$ nm), but the AuNP radius is 10, 15 and 20 nm are performed. Due to the fact that the surrounding medium is an aqueous polymer solution, the irradiation intensity is chosen such that the matrix maximum temperature is below 100 °C. Thus, to find the maximum irradiation intensity value, a parametric scan is performed and the results are presented in Table 10.

Table 10. Variation with intensity of the surrounding medium temperature at 0.1 nm from the AuNP surface

20 nm AuNP		30 nm AuNP		40 nm AuNP	
I (W/cm²)	T (°C)	I (W/cm²)	T (°C)	I (W/cm²)	T (°C)
1.00E+06	83.15	5.00E+05	81.64	2.50E+05	66.73
1.08E+06	88.12	5.60E+05	88.77	3.00E+05	79.68
1.16E+06	93.12	6.20E+05	96.02	3.50E+05	90.84
1.24E+06	98.14	6.52E+05	99.99	3.95E+05	99.99
1.27E+06	99.99	6.80E+05	103.38	4.00E+05	100.96
1.32E+06	103.18	7.40E+05	110.73	4.50E+05	111.08
1.40E+06	108.36	8.00E+05	118.09	5.00E+05	121.2

It can be observed from Table 10 that the temperature of 100 °C is obtained for a minimum intensity of 3.95×10^5 W/cm² in case of the AuNP that has a diameter of 40 nm. To be able to compare the three simulations, the intensity of 3.95×10^5 W/cm² is maintained for all modeled cases. Thus, a comparison for the three simulations in terms of AuNP and surrounding medium temperature is presented in Figure 22. This figure highlights the fact that the heat generated by the AuNP remains in its proximity.

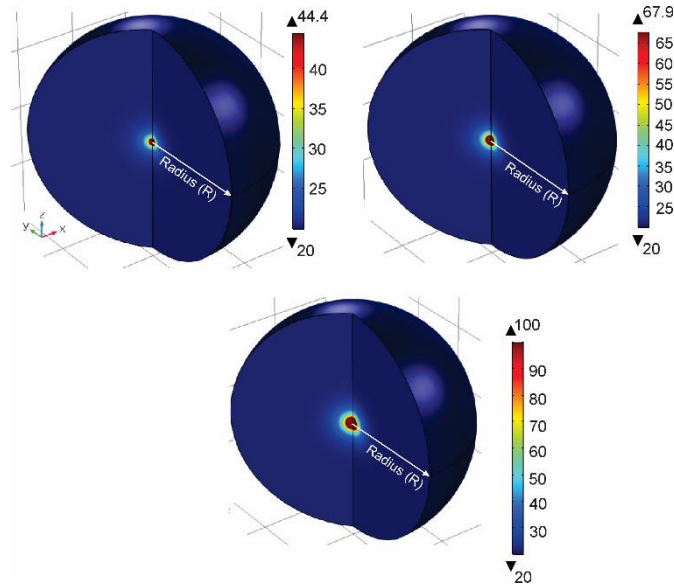


Figure 22. System I temperature at 19 ns and 3.95×10^5 W/cm² intensity for a) 20 nm AuNP b) 30 nm AuNP and c) 40 nm AuNP

The fact that an increase in the AuNP size determines the increase of the system temperature is pointed out in Figures 23 and 24.

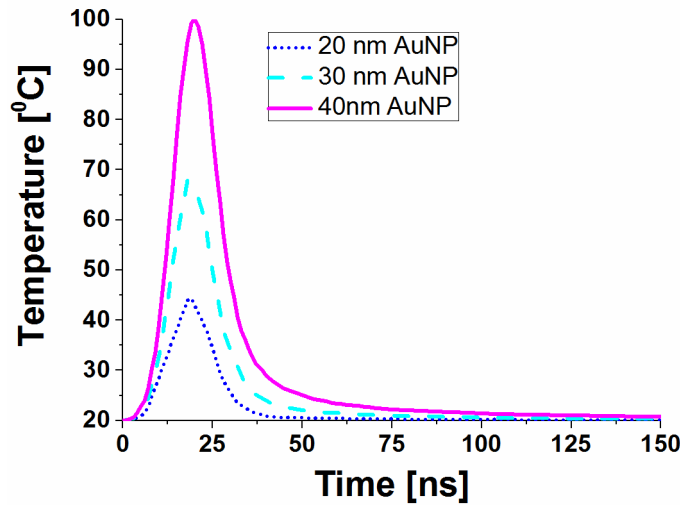


Figure 23. AuNP temperature variation with time – temperature value obtained in the center of the NP ($r_{\text{AuNP}} = 0$)

One can observe from Figure 23 that the AuNP's maximum temperature is reached at 19 ns for all three NP diameters and has a value of 44.45 °C for a 20 nm NP, 67.85 °C for a 30 nm NP and 99.99 °C for a 40 nm NP. In addition, at 24 ns (2τ) there is still a significant temperature rise from the

initial temperature of 16 °C, 34 °C and 64 °C, values which are correlated with the NP size increase. Also, one can note that an increase of the NP diameter from 20 to 30 (40) nm, indicates an energy increase in the NP that corresponds to a temperature rise of 23 (56) degrees, respectively.

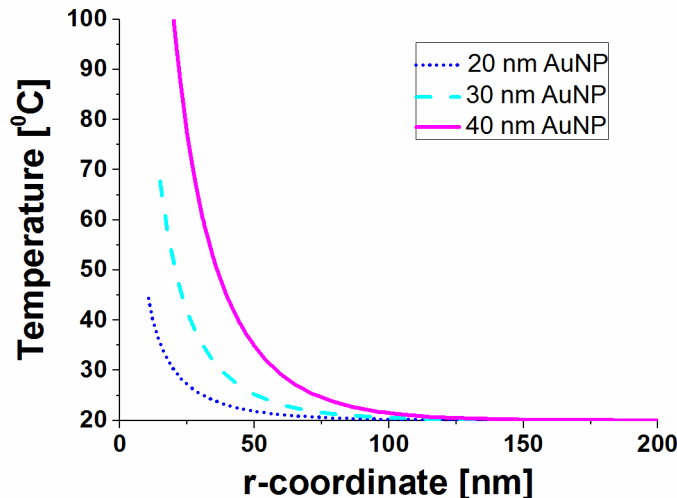


Figure 24. Polymer matrix temperature variation with r-coordinate for 20 nm, 30 nm and 40 nm AuNPs – all cases are represented at 19 ns.

Similar to the AuNP, the temperature of the surrounding medium increases with the increase in the NP diameter. Indeed, in the NP vicinity (0.1 nm away from the NP) we found temperatures of 44.4 °C, 67.4 °C and 99.9 °C for the 20, 30, and 40 nm AuNP size (Figure 24). This temperature difference is explained by the fact that larger NP generate more heat and, in addition, the system's radius (R_s) is not modified in the three simulations leading to a decrease in the polymer matrix volume. Thus, a polymer temperature rise of 23 and 55.5 degrees is observed for a NP diameter increase of 10 nm and 20 nm, respectively.

In this study, we were also interested in the dependence of the polymeric matrix temperature on the systems radius (R_s), the surrounding medium temperature being plotted for relevant moments of time (Figure 25 a,b,c).

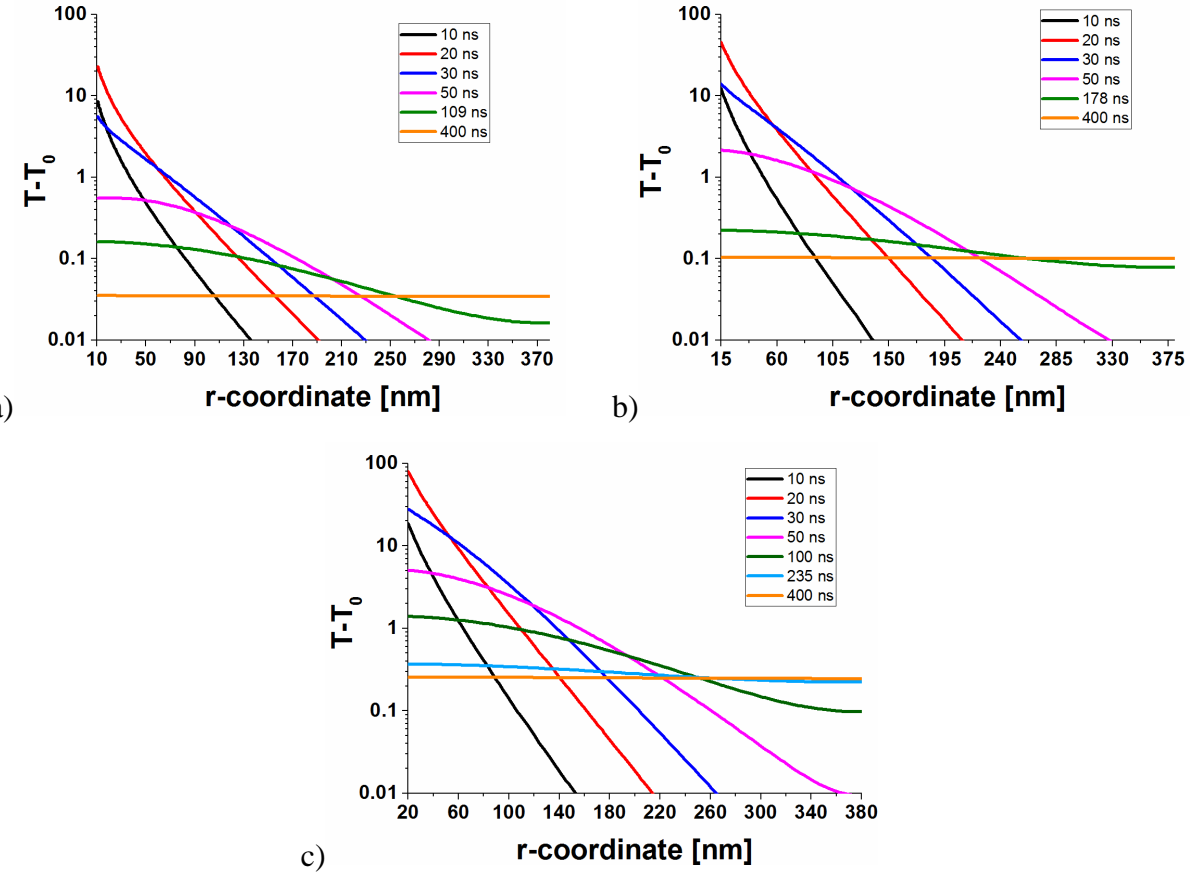


Figure 25. (a) Matrix normalized temperature (in logarithmic scale) as a function on r – coordinate at different times (20 nm AuNP) and $3.95E05$ W/cm 2 intensity. (b) Matrix normalized temperature (in logarithmic scale) as a function on r – coordinate at different times (30 nm AuNP) and $3.95E05$ W/cm 2 intensity. (c) Matrix normalized temperature (in logarithmic scale) as a function on r – coordinate at different times (40 nm AuNP) and $3.95E05$ W/cm 2 intensity.

As seen in Figure 25, the three simulations that correspond to AuNPs of 20 nm (Figure 25a), 30 nm (Figure 25b) and 40 nm (Figure 25c), the PSS medium is significantly heated on a radius of 76 nm, 119 nm and 168 nm, respectively. Furthermore, this figures present the necessary time to reach the thermal equilibrium, which is considered to be reached when:

$$\frac{T_{max} - T_{min}}{T_{max}} < 0.5\% \quad (27)$$

where T_{max} and T_{min} are the systems maximum and minimum temperature, respectively.

In this respect, for 20 nm AuNP the thermal equilibrium is reached at 109 ns, for the 30 nm AuNP at 178 ns and for the 40 nm AuNP at 235 ns. The normalized equilibrium temperature is 0.16 degrees for 20 nm AuNPs, 0.22 degrees for 30 nm AuNPs and 0.37 degrees for 40 nm AuNP. One

can see that both the necessary time to reach the thermal equilibrium and the normalized equilibrium temperature increase due to the NP diameter increase.

3.3 Temperature dynamics of a system that contains an ensemble of spherical AuNPs embedded in a polymer (PSS) matrix – the influence of the AuNP distribution

3.3.1 Methods

Most articles that deal with the heating of metallic NPs due to laser irradiation consider a system similar Sistem I, described in subsection 3.2, which consists of a single AuNP and its surrounding medium. The temperature dynamics in large (infinite) systems is not mathematically modeled. In this type of systems, the temperature is influenced by the NPs diameter or by the nature of various materials as surrounding medium, however, the configurations in which the AuNP can occur may be another important parameter that is worth studying.

The aim of this subsection is to mathematically model the temperature evolution in time and space in a system (denoted System II) that consists of an ensemble of AuNPs that are embedded in a PSS matrix. Thus, the influence of various AuNPs distributions in a large (infinite) system is studied. To be able to compare the two systems (System I and System II), the irradiation source remains a Nd:YAG nanosecond laser that has a Gaussian pulse of 12 ns FWHM, a 532 nm wavelength and an intensity of $3.95E+05$ W/cm² (same as the intensity used in System I). Also, it is assumed that the AuNPs heat uniformly and the heat loss is a result of heat conduction from the metal NP to the polymer surrounding medium. As for System I, the AuNPs surrounding matrix remains the polystyrene sulfonic acid, having its properties presented in Table 8. It is worth mentioning that this aqueous PSS solution provides a stable distribution for its contained AuNPs and can efficiently absorb their generated heat.

To demonstrate the influence of AuNPs distribution on the system's temperature, 100 spherical AuNPs are arranged in four distributions inside a cuboid polymer matrix that has a width and length of 200 nm and a height of 1000 nm. An infinite system is simulated due to imposing periodic boundary conditions at the cuboids lateral limits. The four geometries are denoted array distribution, concentric distribution, radial distribution and random distribution, and are presented in Figure 26a, b, c, and d respectively.

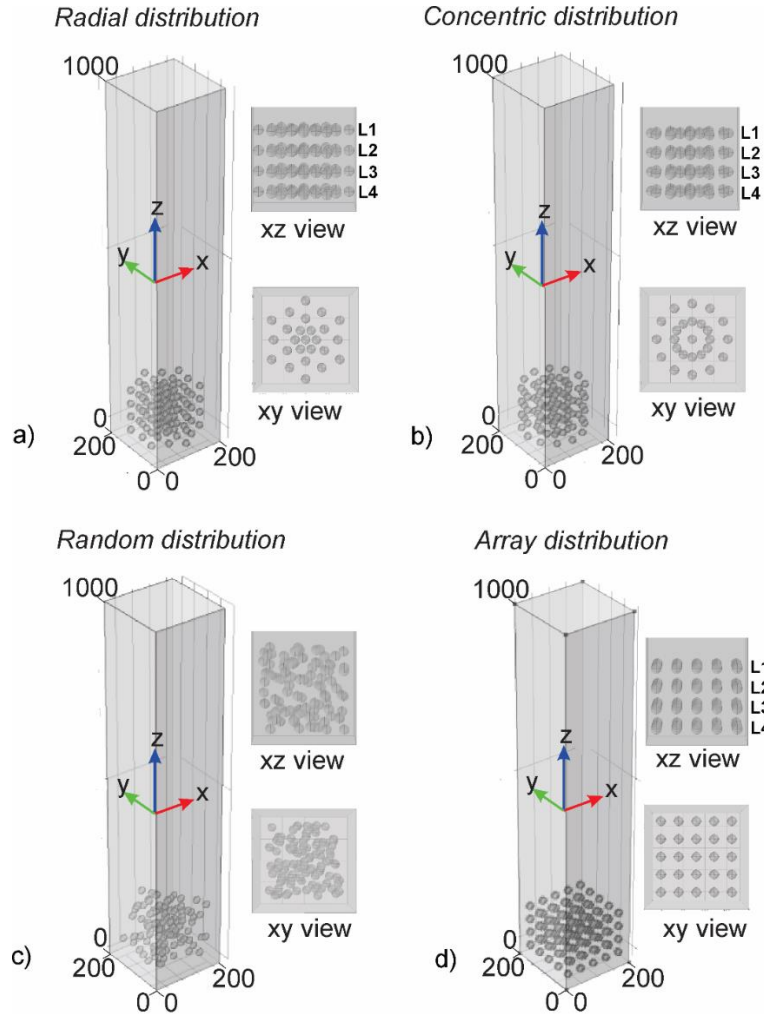


Figure 26. System II distributions: a) radial , b) concentric , c) random , d) array

As observed in Figure 26, in the xz plan, the array, radial and concentric distributions have four layers (L1, L2, L3 and L4) with a 20 nm spacing between them, each layer containing 25 NPs that are organized in the same geometry. In all geometries, the AuNPs are placed in a cube (C1) with 200 nm edge. The **array distribution** has in each layer an array of particles that consists of 5 rows and 5 columns with 20 nm distance between its particles. The **radial distribution** has the AuNPs in the xy plan distributed on four concentric circles and have a supplementary NP in the middle. All circles have six evenly spaced AuNPs. Between each two particles in circle i ($i=2,\dots,4$) there is one particle in the circle $i+1$ that has its center placed at the midway between the centers of the two other particles. The **concentric distribution**, besides the center AuNP, all other 24 AuNPs are placed on two concentric circles, each circle having twelve evenly spaced NPs. The circles have a radius of 40 nm and 80 nm, respectively. For **random distribution**, we developed a model that

generates the coordinates for the center of the AuNPs. The model is implemented in Matlab software, and generates 100 random points that are distributed in a 200 nm length cube in which the distance between two points should be greater than 20 nm. Thus, the AuNPs are distributed inside a 200 nm length cube and adjacent NP do not touch.

System's II temperature dynamics is numerically modeled in Comsol software using the Heat Transfer in Solids module along with a three dimensional geometry. The spherical AuNPs have a diameter of 20 nm, are modeled as heat sources and their heat generation is calculated using Equation 21. Equation 19 and Equation 20 describe the heat transfer equations for System II, whereas the imposed initial and boundary conditions are described as follows:

1. Initial conditions:

$$T_{AuNP}(x,y,z,0)=T_{PSS}(x,y,z,0)=293.15 \text{ K}$$

2. Boundary conditions:

- **Lower boundary, no heat flux through lower face:** $q(x,y,Lz_0,t)=0$; $Lz_0=0$ nm;
- **Upper boundary, no heat flux through upper face:** $q(x,y,Lz,t) = 0$, where Lz is the height of the system, $Lz = 1000$ nm;
- **Boundary conditions in x and y direction** (periodic heat boundary conditions):

$$-k_{PSS} \frac{\partial T_{PSS}}{\partial x} \Big|_{x=Lx_0} = k_{PSS} \frac{\partial T_{PSS}}{\partial x} \Big|_{x=Lx} \quad -k_{PSS} \frac{\partial T_{PSS}}{\partial y} \Big|_{y=Ly_0} = k_{PSS} \frac{\partial T_{PSS}}{\partial y} \Big|_{y=Ly},$$

Where Lx is the length of the system ($Lx_0=0$ and $Lx=200$ nm) and Ly is the width of the system ($Ly_0=0$ and $Ly=200$ nm). In addition, at each AuNP surface, the continuity of flux and temperature is imposed.

3.3.2 Results and discussions

The temperature difference regarding the system's maximum temperature and its associated time is presented for the four distributions in Figure 27. This figure is suggestive to point out the fact that the heat accumulates near the AuNPs and that the AuNP's distribution influences the system's temperature.

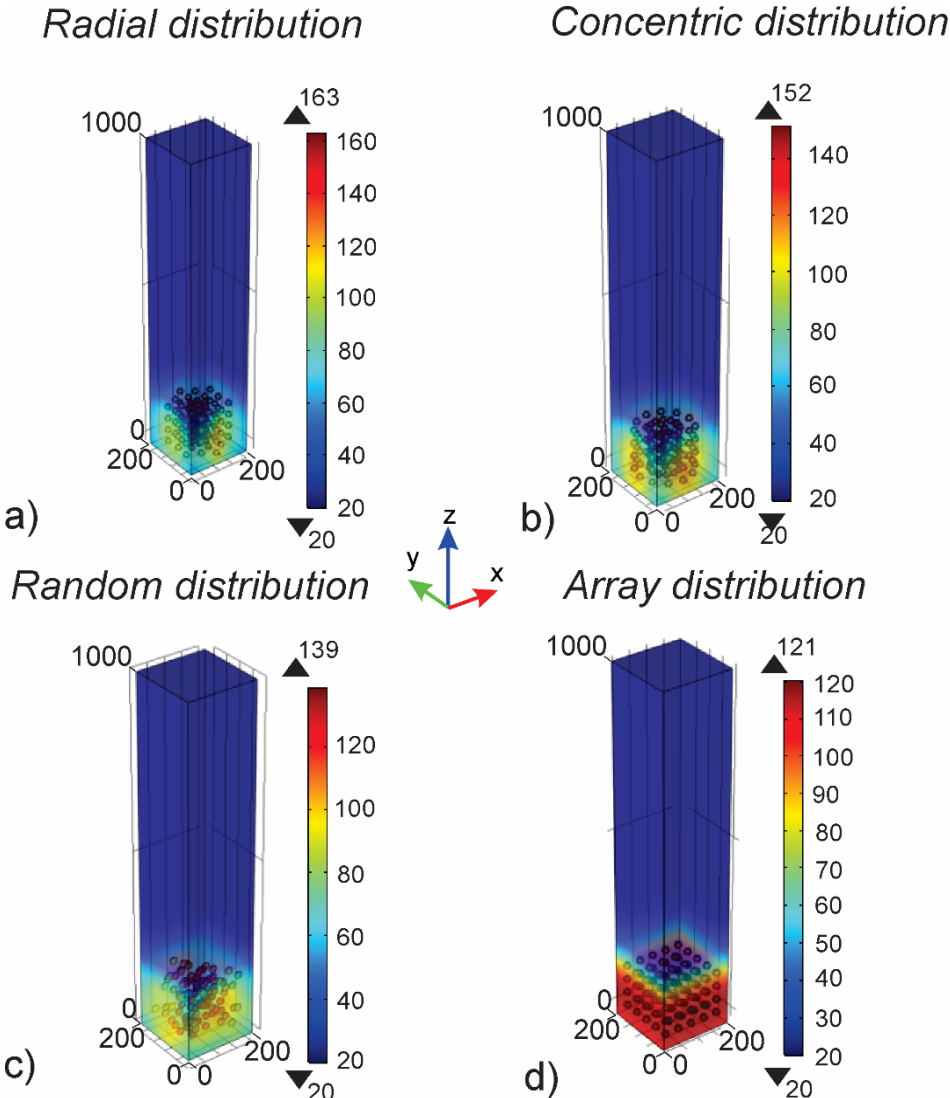


Figure 27. System II – maximum temperature presented for the: a) radial distribution, b) concentric distribution, c) random distribution, d) array distribution

For all four geometries, the data from the Comsol simulations regarding the temperature in each considered point in the geometry, at all moments in time, was extracted and further processed in Matlab software. For each distribution, the point that has the maximum temperature along with its associated moment in time is obtained. The data are presented comparatively in Table 11.

Table 11. System II – the point in space and the moment in time in which the maximum temperature is reached

	Point (x,y,z) [nm]	Maximum Temperature [°C]	Time [ns]
Array distribution	In each NP from layer 2 situated at 70 nm on z direction	120.5	27
Radial distribution	Pt1 (100, 109.23, 73.82)	163.4	23
Concentric distribution	Pt2 (100, 109.23, 73.82)	151.35	25
Random distribution	Pt3 (116.07, 105.58, 122.61)	138.85	24

As seen in Figure 27 and Table 11, the maximum temperature of 163.4 °C is reached in case of the **radial distribution**, at 23 ns. The next maximum temperature is reached at 25 ns in the **concentric distribution** (151.35 °C) followed by the **random distribution** (138.85 °C) at 24 ns and finally, the lowest temperature is reached in the **array distribution** (120.5 °C) at 27 ns. Thus, one can see that the radial geometry has the highest maximum temperature and this value is greater than the one in the concentric, random and array distribution with 12 degrees, 24 degrees and 42.8 degrees, respectively.

The point where the system's maximum temperature is reached is highlighted in Figure 28.

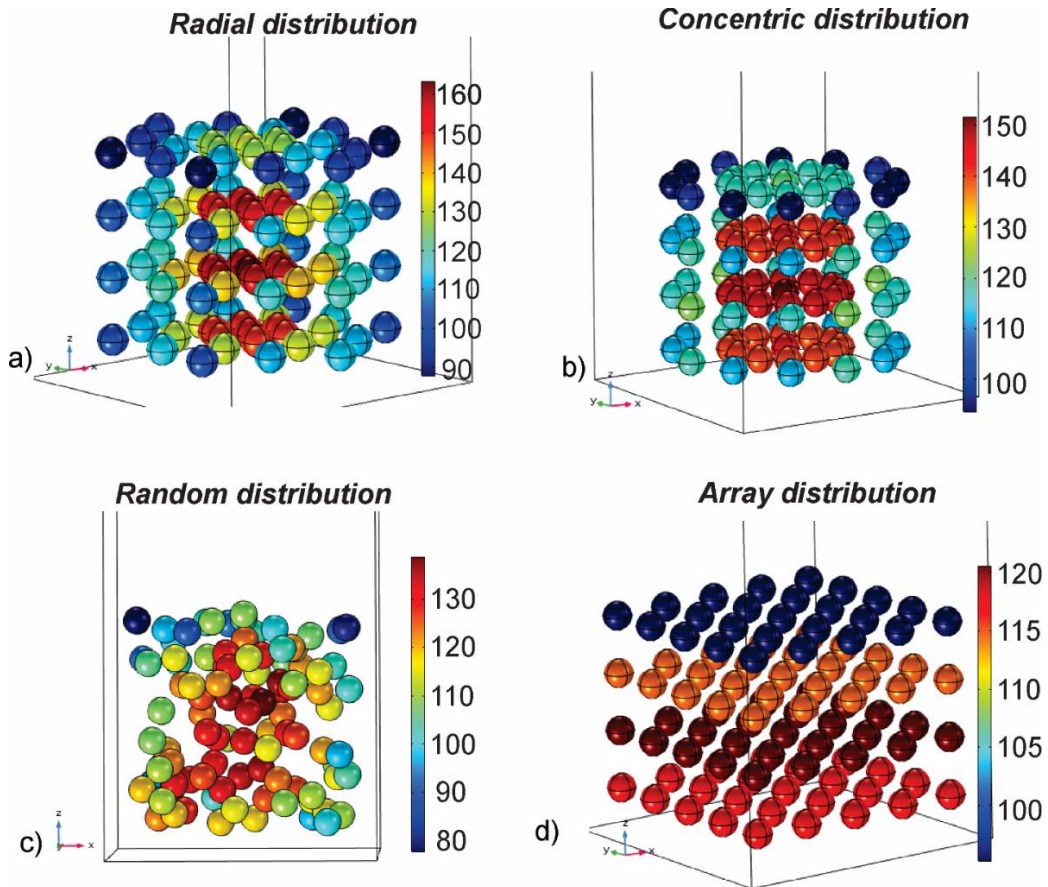


Figure 28. System II – AuNP maximum temperature presented for the: a) radial distribution, b) concentric distribution, c) random distribution, d) array distribution

For a better comparison, the AuNPs temperature is presented on the same temperature scale in Figure 29.

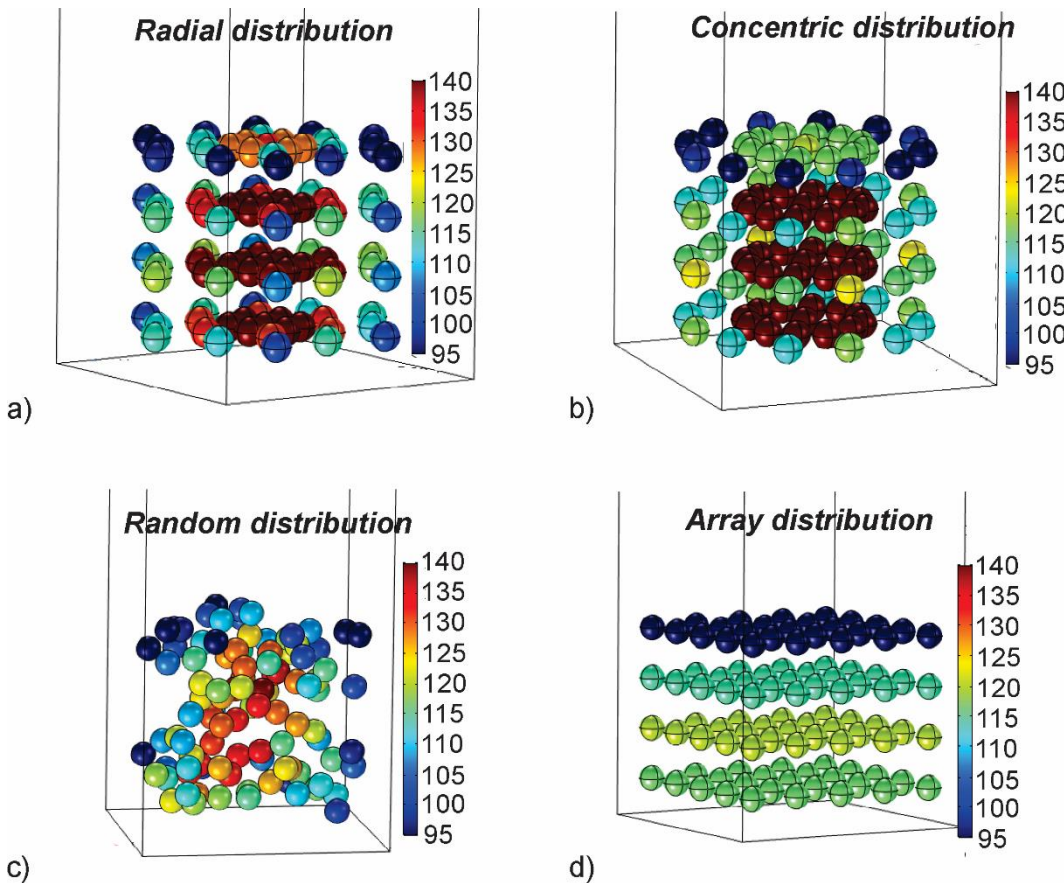


Figure 29. System II – AuNP maximum temperature presented for the: a) radial distribution, b) concentric distribution, c) random distribution, d) array distribution

The ***radial and concentric distributions*** reach the maximum temperature in the points Pt1 and Pt2 respectively, points which have the same coordinates and are situated in layer 2, inside the center AuNP, but close to its surface. The distance from the cube's C1 center to this points is 27.7 nm. The ***random geometry*** reaches its maximum temperature in point Pt3 which is also situated inside the AuNP (close to the NP surface). The distance from the cube's C1 center to this point is 28.3 nm. The ***array geometry*** does not have a specific point for the maximum temperature because all NPs that are situated in layer 2, at 70 nm in the z direction, have the same temperature.

Despite the relevant differences that occur between the various distributions maximum temperatures, by analyzing the system's average temperature one can see that the radial and concentric geometries have a medium temperature of 36.8°C , whereas the array and random distribution have a medium temperature of 34.9°C .

A line in the z direction and a zx plan that passes through this points is drawn so that the temperature variation with space (z and x coordinates) and time is studied (Figure 30).

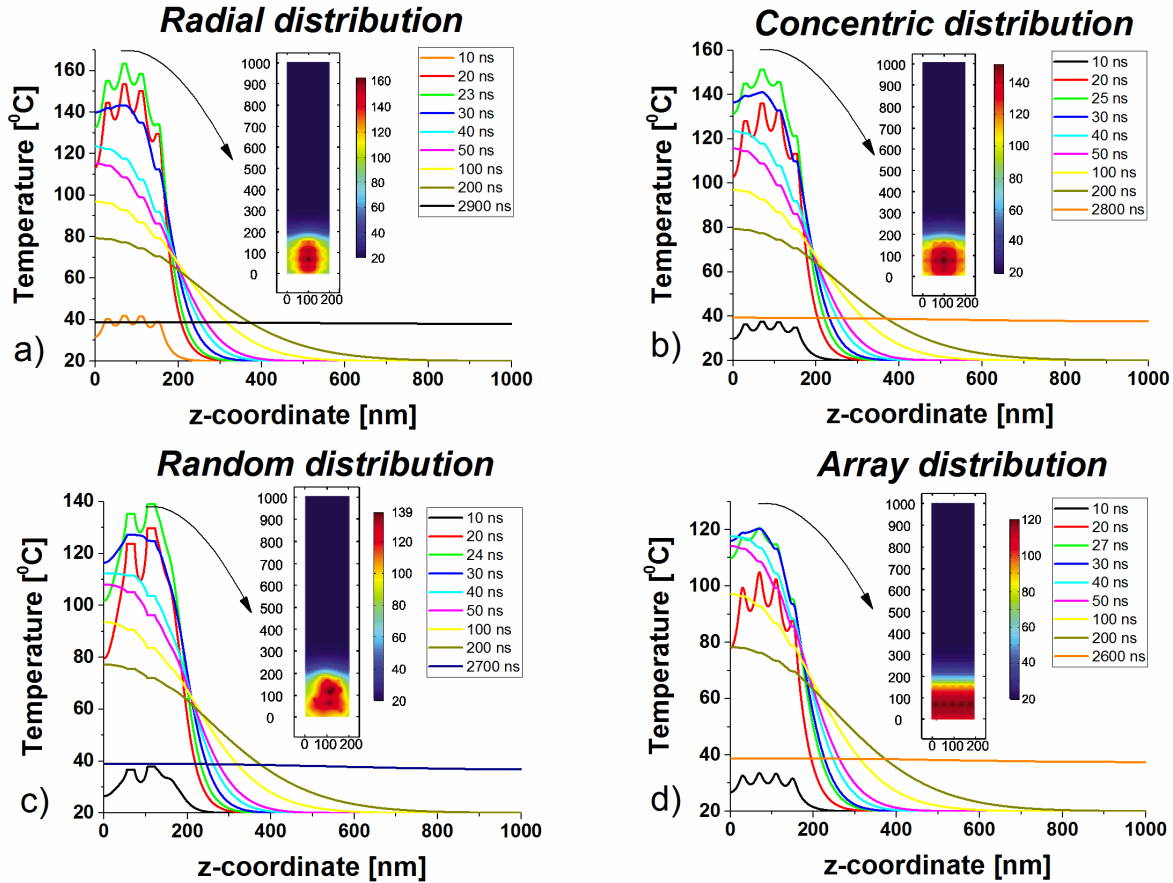


Figure 30. System II – Temperature variation with x and z coordinate at different moments in time for: a) array distribution, b) radial distribution, c) concentric distribution, d) random distribution.

Figure 30 reveals the fact that the highest temperatures are detected in areas where the spherical NPs are most agglomerated (the central area in case of the radial and concentric distribution). Furthermore, it can be noticed that the AuNPs distributions also influences the necessary time to reach the thermal equilibrium. Thus, one can see that the shortest time is 2600 ns and is achieved in case of the array distribution. The random distribution reaches the thermal equilibrium in 2700 ns, followed by the concentric distribution with 2800 ns and finally by the radial distribution with 2900 ns.

The longest time to reach the thermal equilibrium and the highest temperatures are encountered in the **radial distribution** for the reason that, compared with the other distributions, the radial distribution has its AuNPs concentrated in the central area. Thus, having a less polymer volume to diffuse in, the heat accumulates in the central area resulting in a temperature increase and consequently a longer time to reach the thermal equilibrium.

To emphasize the importance of simulating a large system that reflects a real AuNP distribution rather than limiting to only one AuNP, the comparison between System I and System II (the random distribution) has been done. Figure 31 presents the temperature evolution in time in: i) the center of the 20 nm AuNP in case of System I and ii) the center of the AuNP that has the highest temperature in System II – the random distribution.

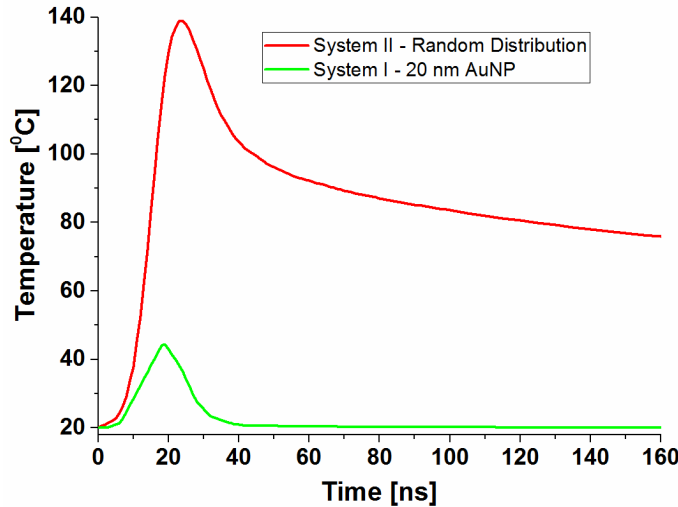


Figure 31. Temperature evolution in time in case of System I (in the center of the AuNP) and System II (the center of the AuNP that has the highest temperature)

From Figure 31 one can observed that the highest temperature is reached in System II, the difference between the two systems being $44.5\text{ }^{\circ}\text{C}$. System I reaches its maximum temperature in 19 ns, whereas the radial distribution in System II reaches the maximum temperature in 24 ns. Additionally, there is a significant difference when comparing the necessary time to reach the thermal equilibrium. It can be observed that the random distribution needs 2700 ns to reach the thermal equilibrium, whereas the single AuNP only needs 109 ns. This phenomena are attributed to the collective effects that are present in a real AuNP thin film, where a significant amount of NPs is heated at once [119].

3.4 Temperature dynamics of a system that contains an ensemble of spherical AuNPs embedded in a polymer (PSS) matrix – the influence of the interfacial thermal conductance

3.4.1 Methods

It is known that, in case of two different materials, their thermal property mismatch leads to an interfacial resistance known as the Kapitza resistance. Due to this resistance, a temperature jump is observed at the interface of the two materials. In case of the heat transfer between the two

materials, the material interface is characterized by an interface thermal conductance (G) that can be determined using the acoustic mismatch model or the diffusion mismatch model [120,121].

In case of the interface between a fluid interface and AuNPs, the interface thermal conductance influences the NPs thermal decay [120]. Wilson et al suggest that the interface thermal conductance has to be taken into account only if G is much smaller than a critical interface thermal conductance (G_c), otherwise only the fluids effusivity plays a role in the NP cooling [121]. The interface thermal conductance has values between 100 MW/m²K and 300 MW/m²K [120], while the critical interface thermal conductance can be determined from the following equation [121]:

$$G_c = \frac{3C_{pm}k_m}{r_{AuNP}C_{p_{AuNP}}}, [\text{Wm}^{-2}\text{K}^{-1}] \quad (28)$$

where C_{pm} and $C_{p_{AuNP}}$ are the heat capacities of medium and the AuNP, respectively, k_m is the medium conductivity and r_{AuNP} is the AuNP radius.

Therefore, using Equation 28, the critical interface thermal conductance of 165 MW/m²K is calculated in case of a 20 nm AuNP immersed in an aqueous PSS solution. Comparing this value with the interface thermal conductance of 105 MW/m²K [113] it is observed that G_c is not much higher than G , the difference being of 60 MW/m²K. However, due to the fact that the interface thermal conductance can have a significant impact on the NPs thermal decay, the aim of this subsection is to determine the temperature evolution in time and space in a large system that consists of AuNPs embedded in an aqueous PSS matrix when the interface thermal conductance is taken into account. The AuNPs are irradiated with a Nd:YAG nanosecond laser that has a Gaussian pulse of 12 ns at FWHM, a 532 nm wavelength and an intensity of 3.95E+05 W/cm². The mathematical modeling is done for the four AuNP distributions (array, radial, concentric and random distribution) from System II.

As in the previous subsection, the temperature dynamics is numerically modeled in Comsol software using the Heat Transfer in Solids module along with a three dimensional geometry. The spherical AuNPs of 20 nm diameter are modeled as heat sources and their heat generation is calculated using Equation 21. Equation 19 and Equation 20 describe the heat transfer equations for System II, whereas at the boundary between the AuNP and the polymer matrix, a thermal contact boundary condition with a gap conductance of 105 MW/(m²K) [113] is imposed.

$$\rho_{AuNP}C_{p_{AuNP}}\frac{\partial T_{AuNP}}{\partial t} = k_{AuNP}\nabla^2T_{AuNP} + \frac{3K_{abs}If(t)}{4r_{AuNP}}, [\text{W}/\text{m}^3] \quad (19)$$

$$\rho_{PSS} C_{p_{PSS}} \frac{\partial T_{PSS}}{\partial t} = k_{PSS} \nabla^2 T_{PSS}, [\text{W/m}^3] \quad (20)$$

where ρ is density, C_p is specific heat, k is thermal conductivity, $T(^0\text{C})$ is the temperature, K_{abs} is the absorption efficiency, $I(\text{W cm}^{-2})$ is the laser intensity, $r(\text{m})$ is the nanoparticle radius and $f(t)$ is the laser pulse time profile.

1. Initial conditions:

$$T_{AuNP}(x,y,z,0) = T_{PSS}(x,y,z,0) = 293.15 \text{ K}$$

2. Boundary conditions:

- **Lower boundary:** $q(x,y,Lz_0,t)=0$; $Lz_0=0 \text{ nm}$;
- **Upper boundary:** $q(x,y,Lz,t)=0$, where Lz is the height of the system, $Lz = 1000 \text{ nm}$;
- **Boundary conditions in x and y direction** (periodic heat boundary conditions):

$$-k_{PSS} \frac{\partial T_{PSS}}{\partial x} \Big|_{x=Lx_0} = k_{PSS} \frac{\partial T_{PSS}}{\partial x} \Big|_{x=Lx} \quad -k_{PSS} \frac{\partial T_{PSS}}{\partial y} \Big|_{y=Ly_0} = k_{PSS} \frac{\partial T_{PSS}}{\partial y} \Big|_{y=Ly},$$

where Lx is the length of the system ($Lx_0=0$ and $Lx=200 \text{ nm}$) and Ly is the width of the system ($Ly_0=0$ and $Ly=200 \text{ nm}$).

• Boundary condition at the AuNP surface

$$-(-k_{AuNP} \nabla T_{AuNP}) = -G(T_{PSS} - T_{AuNP}),$$

$$-(-k_{PSS} \nabla T_{PSS}) = -G(T_{AuNP} - T_{PSS}),$$

where $G/(\text{W m}^{-2} \text{ K}^{-1})$ is the interface thermal conductance.

3.4.2 Results and discussions

For the four AuNPs distributions, the maximum temperature along with its associated time are presented in Figure 32. Due to the fact that the maximum temperature is reached inside the AuNPs, Figure 32 highlights the NP that reaches the highest temperature.

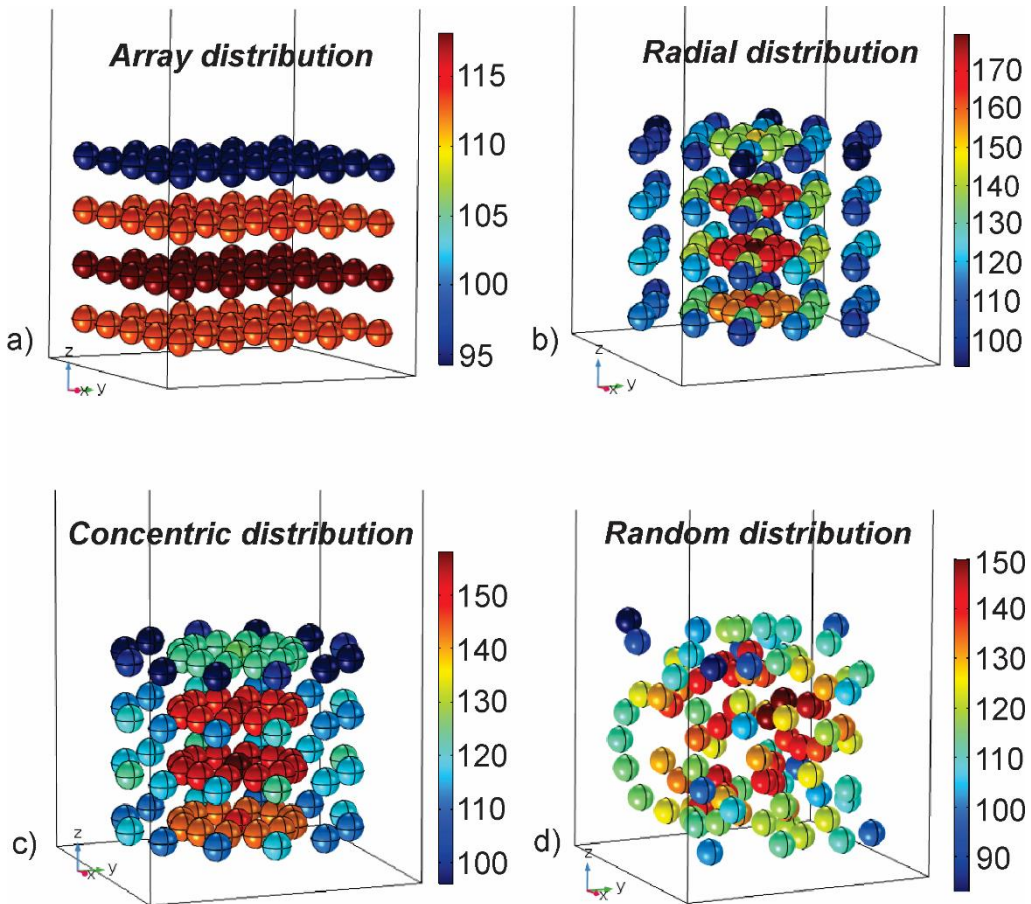


Figure 32. System II – Maximum temperature presented for a) array distribution, b) radial distribution, c) concentric distribution, d) random distribution.

As seen in Figure 32, the maximum temperature of 179.5°C is reached in the **radial distribution** after 22 ns. This temperature is encountered in the central AuNP in layer 2. Also layer's 2 central AuNP, the **concentric distribution** reaches its maximum temperature of 164.6°C after 24 ns. A slightly smaller temperature of 149.7°C is reached after 22 ns in the **random distribution**, whereas the smallest temperature of 124.7°C is reached after 26 ns in the **array distribution**. In this distribution, the maximum temperature is found in all AuNPs that are situated in layer 2. Thus, the temperature difference between the radial distribution and the concentric, random and array distribution is: 14.9°C , 30.5°C and 59.6°C , respectively.

Figure 33 presents the temperature variation with the z coordinate at different moments in time. The line in the z coordinate for which the temperature is plotted is such chosen that it passes through the center of the particle that reaches the maximum temperature. For the time at which the system's maximum temperature is reached, also the temperature in the xz plane is presented. Thus, it can be

seen that as in the simulations where the interface thermal conductance was not taken into account, the highest temperatures are reached in areas where the spherical NPs are most agglomerated. Furthermore, the necessary time to reach the thermal equilibrium is also influenced by the AuNPs distribution and its value decreases as follows: 3000 ns (radial distribution), 2900 ns (concentric distribution), 2800 ns (random distribution) and 2700 ns (array distribution) (Figure 32).

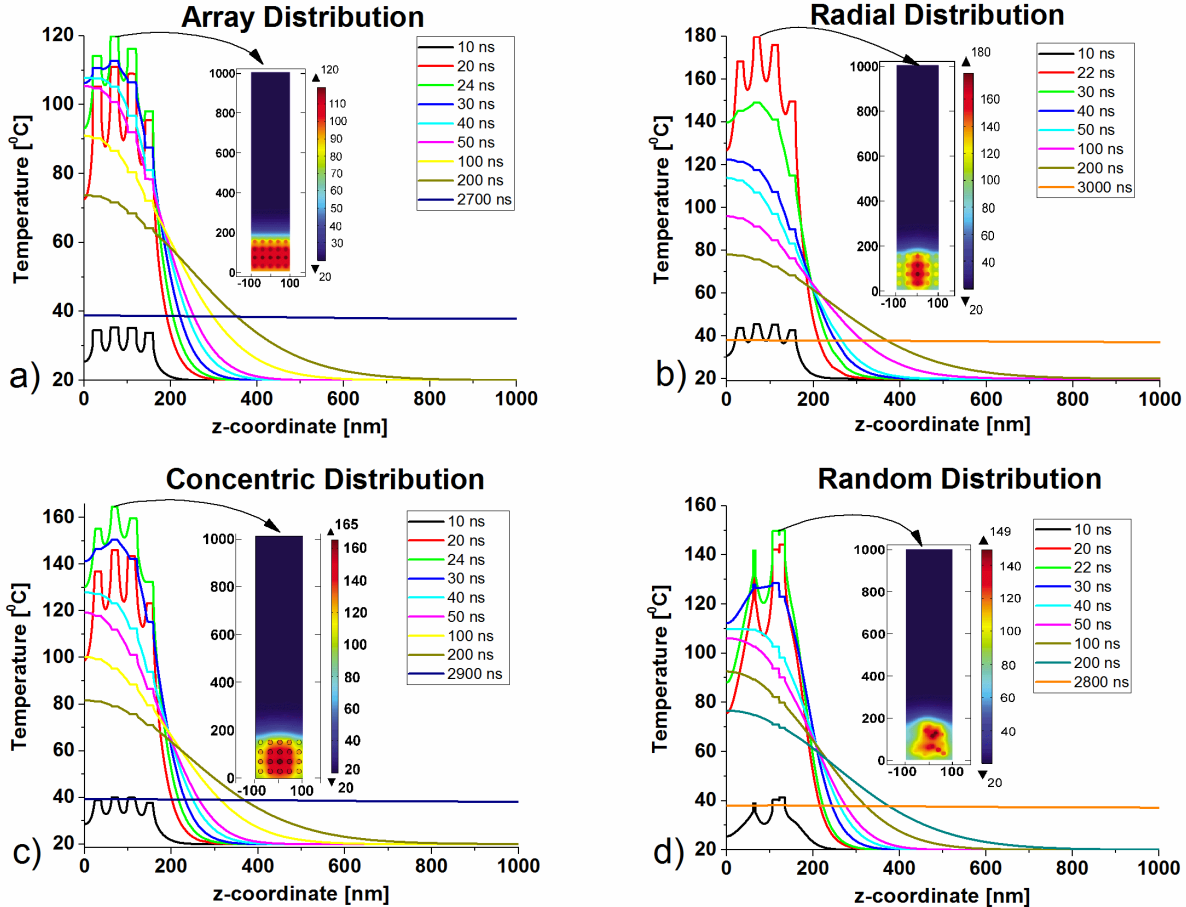


Figure 33. System II – Temperature variation with x and z coordinate at different moments in time for: a) array distribution, b) radial distribution, c) concentric distribution, d) random distribution.

For better understanding the influence of the interfacial thermal conductance on the system's temperature, we performed a comparison between the four AuNP distributions in which G_c is not taken into account (Simulation 1) and this last case in which G_c is used as a boundary condition at the interface between the AuNP and the polymer matrix (Simulation 2). Figure 34 presents comparatively the temperature dynamics in the NP that reaches the maximum temperature in the four AuNPs distributions. It can be observed that the simulations that consider G_c reach higher temperatures, with a temperature difference for the four distributions of: i) 4.2 °C for the array

distribution, ii) 10.85 °C for the random distribution, iii) 13.27 °C for the concentric distribution and iv) 16.1 °C for the radial distribution. Also the time needed to reach the AuNP maximum temperature suffers practically no modification (a slight decrease - 1 ns drop) in the simulations that take into account the interfacial thermal conductance.

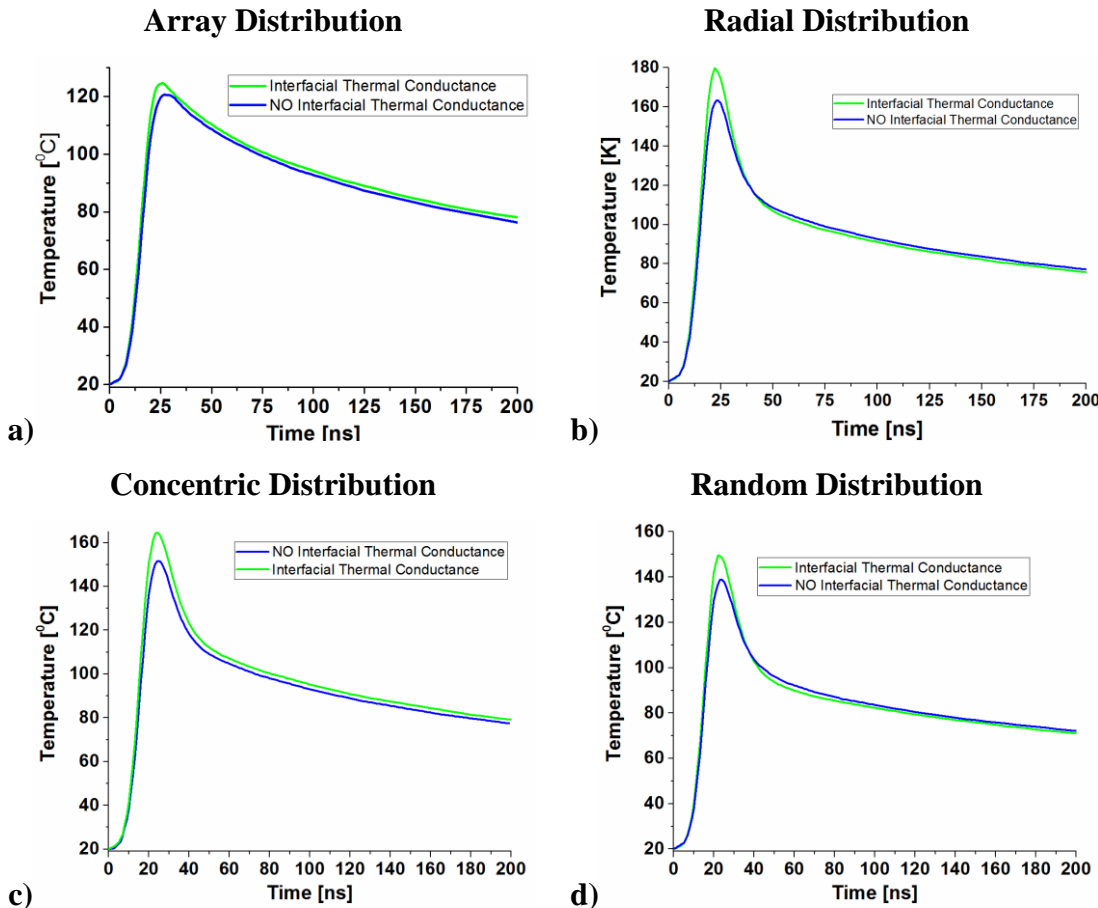


Figure 34. AuNP temperature evolution in time - Comparison between Simulation I and Simulation II for:
a) array distribution b) radial distribution, c) concentric distribution, d) random distribution.

Besides the AuNP temperature difference, also the temperature variation with the z coordinate is investigated (Figure 35). The line in the z coordinate for which the temperature is plotted is such chosen that it passes through the center of the particle that reaches the maximum temperature.

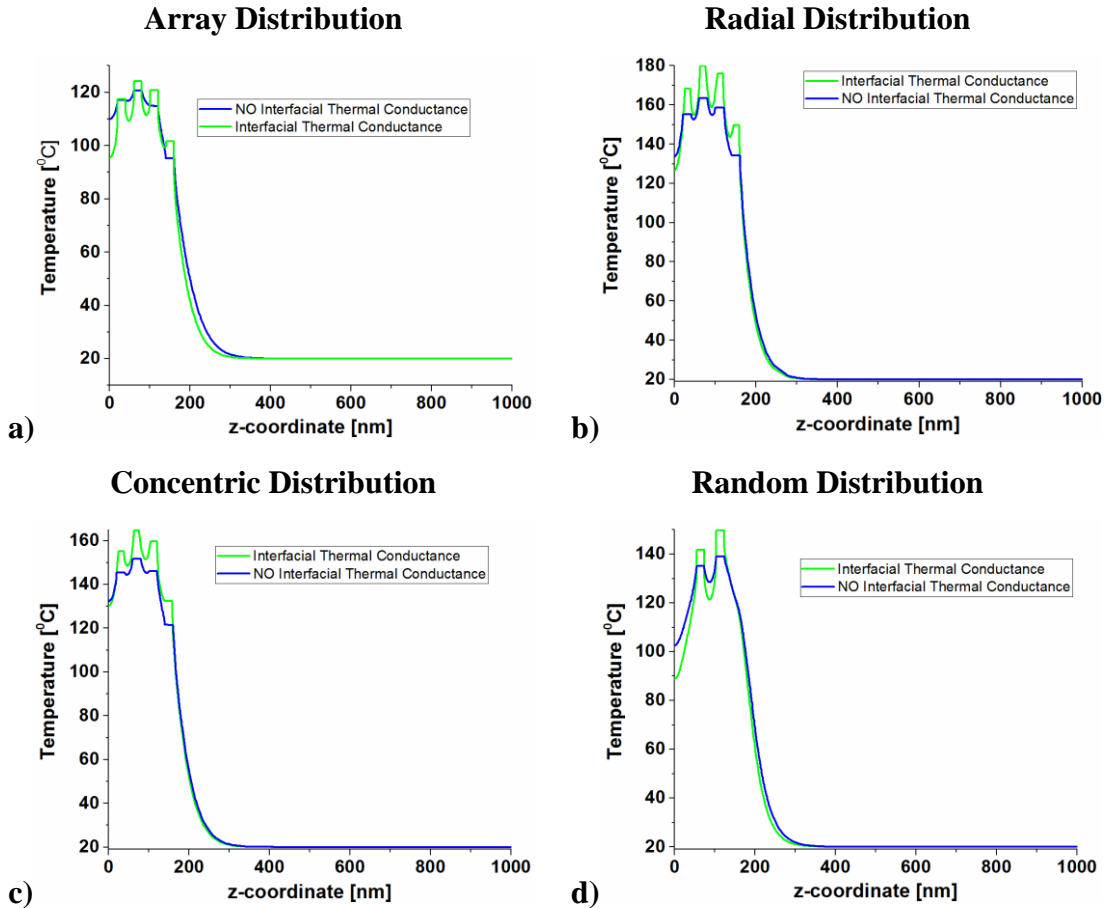


Figure 35. Temperature variation with z coordinate at the time when the system reaches its maximum temperature - Comparison between the Simulation I and Simulation II for: a) array distribution b) radial distribution, c) concentric distribution, d) random distribution

From Figure 35 one can see that the main temperature difference between Simulation I and II is reached in the AuNPs. The differences are attributed to the thermal property mismatch between the AuNPs and the aqueous PSS matrix. Thus, if the interface thermal conductance can not be neglected, the AuNPs thermal decay is achieved in a longer time, phenomenon that leads to higher temperatures in the AuNPs and consequently higher maximum temperatures in the system.

In conclusion, the interface thermal conductance influences the AuNPs thermal decay, having a significant influence on the temperature's system in case of the radial distribution.

3.5 Near field effects and temperature dynamics of laser irradiated gold nanoparticles

The previous subsections mathematically models the temperature dynamics of ns laser irradiated AuNPs that are embedded in a PSS matrix. The simulations rely on the fact that the AuNPs generated heat depends on the NP absorption cross section (Equation 24). Besides this approach,

there are studies that determine the AuNPs heat by using Joule-Lenz relation. This approach assumes that the heat generated by the AuNPs ($Q(r,t)$) depends on the NP's electric field ($E(r,t)$) and on the current density ($J(r,t)$) [122]:

$$Q(r,t) = J(r,t) * E(r,t) , [\text{W/m}^3] \quad (29)$$

$$Q(r,t) = 0.5Re \left[i\omega \frac{\varepsilon_{AuNP}}{4\pi} |E(r)|^2 \right] , [\text{W/m}^3] \quad (30)$$

$$E(r) = \frac{2\varepsilon_m}{2\varepsilon_m + \varepsilon_{AuNP}} E_0 , [\text{V/m}] \quad (31)$$

where ω is the frequency, ε_{AuNP} and ε_m are the dielectric functions of the AuNPs and the surrounding medium, respectively.

Both approaches assume that inside the AuNPs there is a local homogeneous electric field and therefore, the NP heats homogeneously.

Recent studies suggest that if laser irradiated AuNPs have the inter-particle distance less than four or five times their diameter [119], a **near-field enhancement** effect is observed at the NPs external surface. This local field enhancement is given by the sum of the incident and scattered vector fields on the same surface [122] and it depends on the distance between the NPs and on the electric field polarization [123,124]. Experimentally, the near-field interactions can induce red/blue shifts of the SPR absorbance maxima along with modifications of the SPR width and amplitude [123–125]. Thus, in case of a linear chain of AuNPs, if the inter-particle distance is decreased, the SPR peak redshifts in case of an electric field polarized parallel with the AuNPs and blue shifts in case of an orthogonal polarization [124]. The influence of the inter-particle distance end electric field polarization on the AuNPs electric field amplitude can be studied also by DDA or FDTD or FEM modelling [123,125–127].

According to these studies, sufficiently close laser irradiated AuNPs give rise to an inhomogeneous electric field in the AuNPs mainly due to its huge enhancement at the NPs surface. Equation 31 suggests that the AuNPs heat is influenced by the local electric field, thus the near-field interactions should be taken into account.

The aim of this subsection is to numerically model the temperature evolution in time and space in a system that contains water immersed AuNPs and takes into account the heat accumulated by the metal NPs due to near-field interactions.

3.5.1 AuNPs in a cross-type geometry - 2D model

3.5.1.1 Methods

For a better understanding of the phenomenon, the laser irradiated system consists of nine spherical AuNPs that have a radius of 10 nm, are arranged in a cross-type geometry with 40 nm distance (d) between each two AuNPs and have a sufficiently large amount of water as a surrounding medium (Figure 36). The cross-type geometry was chosen having in mind the possible electric field effects along the propagation direction as well as along the polarization direction of the laser field.

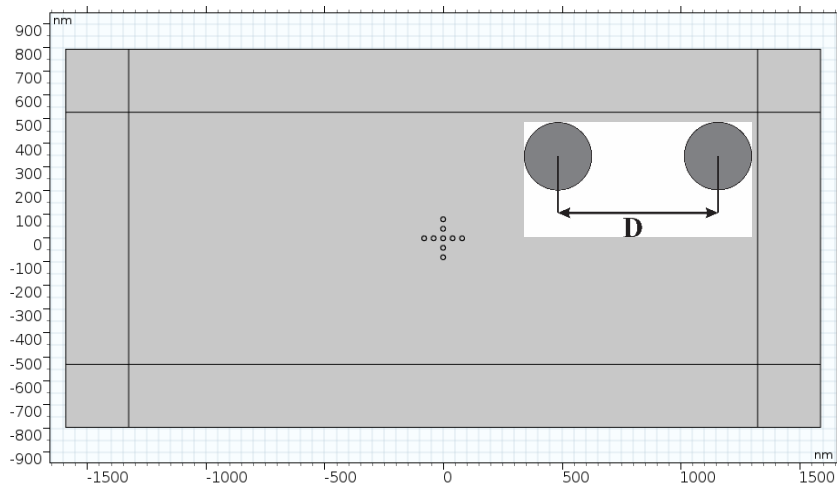


Figure 36. AuNPs arranged in a cross-type geometry

The irradiation source is considered to be a Nd:YAG nanosecond laser that has a Gaussian pulse of 12 ns at FWHM, 532 nm wavelength, a waist radius that is twice the wavelength and an intensity of 3.95E+05 W/cm². The AuNPs and water properties are obtained from the Comsol software material database and are presented in Table 12.

Table 12. Water and Au properties at 20 °C

	Measurement units	H ₂ O	AuNP
Density (ρ)	kg m ⁻³	1000	19300
Heat Capacity (C_p)	J kg ⁻¹ K ⁻¹	4186	129
Thermal Conductivity (k)	W m ⁻¹ K ⁻¹	0.598	317

The electric field enhancement effect, the heat generated by the irradiated AuNPs and the system's time and space temperature evolution are modeled in a two-dimensional geometry, using the finite element method (FEM) that is implemented in Comsol software. The system's near-field interactions and the AuNPs heat accumulation are modeled using the "Wave Frequency Domain"

module (Simulation I), whereas the temperature dynamics is modeled in the “Time Dependent Heat Transfer in Solids” module (Simulation II). In order to determine the system’s temperature, the AuNP’s are modeled as heat sources whose values are in fact Simulation I solution ($Q(x,y)$). Thus, the electric field enhancement and the AuNPs heat generation model consists of solving a wave equation for a homogeneous dielectric for three domains: i) a perfectly matched layer (PML), which is the outermost layer, and has the role of absorbing all radiated waves with small reflections [128], ii) a rectangular domain that represents the water surrounding matrix and iii) the nine circles with a radius of 10 nm that are arranged in a cross-type geometry and represent the AuNP’s. The wave equation is given by:

$$\nabla(\nabla \times E) - k_0^2 \varepsilon_r E = 0 \quad (32)$$

$$\varepsilon_r = (n - ik)^2 \quad (33)$$

where E is the electric field that propagates along the $-y$ - coordinate and is polarized in x direction, k_0 is the wavenumber ($k_0=2\pi n_{H2O}/\lambda_0$), n and k are the real and imaginary parts of the refractive index and are obtained from Johnson and Christy for AuNPs [129] and from Hale and Querry for water [130].

The system is irradiated with a Gaussian pulse, whose electric field equation is presented as follows:

$$E(x, y) = E_0 \sqrt{\frac{\omega_0}{\omega(y)}} \exp\left(\frac{-x^2}{\omega(y)}\right) \exp\left(\frac{jk_0 x^2}{2R(y)}\right) \exp\left[j\left(k_0 x - 0.5 \operatorname{atan}\left(\frac{y}{z_0}\right)\right)\right], [\text{V/m}] \quad (34)$$

where ω_0 is the waist radius, $\omega(y)$ is the beam waist for different positions along the y axis, z_0 is the Rayleigh range, $R(y)$ is the radius of curvature and E_0 is the initial applied electric field amplitude and has a value of 1.220616e6 [V/m].

$$E_0 = \sqrt{2I_0 \sqrt{\frac{\mu_0}{\varepsilon_0}}}, [\text{V/m}] \quad (35)$$

where $\mu_0/(\text{F m}^{-1})$ is the vacuum permeability and $\varepsilon_0/(\text{N/m}^2)$ is the vacuum permittivity. The total electric field is defined as the sum of the incident (background) and scattered electric fields:

$$E_t = E_b + E_s, [\text{V/m}] \quad (36)$$

where E_t is the total electric field, E_b is the incident electric field and E_s is the scattered electric field.

The heat generated by the AuNPs is equal to the total power dissipation energy (Q_t) which is given by:

$$Q_t = Q_{ml} + Q_{rh}, [\text{W/m}^3] \quad (37)$$

where Q_{ml} are the magnetic losses and $Q_{rh}/\text{W m}^{-3}$ are the resistive losses.

In this simulations the magnetic losses are considered zero, whereas the resistive losses are calculated as follows:

$$Q_{rh} = \frac{1}{2} Re[J \cdot E^*], [\text{W/m}^3] \quad (38)$$

where $J/[\text{A/m}^2]$ is the current density and $E^*/[\text{V/m}]$ is the complex conjugate of the electric field vector.

As initial condition, the electric field in all three dimensions is imposed to be 0, whereas the PML that absorbs all the radiative waves with small reflections is chosen as a boundary condition.

The temperature dynamics model consists of solving the following equations:

$$\rho_{AuNP} C_{p_{AuNP}} \frac{\partial T_{AuNP}}{\partial t} = k_{AuNP} \nabla^2 T_{AuNP} + Q_t \exp(-(t - t_0)^2/\tau^2), [\text{W/m}^3] \quad (39)$$

$$\rho_{H_2O} C_{p_{H_2O}} \frac{\partial T_{H_2O}}{\partial t} = k_{H_2O} \nabla^2 T_{H_2O}, [\text{W/m}^3] \quad (40)$$

where ρ is density, C_p is specific heat, k is thermal conductivity, $T/(\text{ }^\circ\text{C})$ is the temperature, $\tau=12$ ns FWHM is the Gaussian pulse duration and t_0 is the position of the center of the peak.

As **initial conditions**, the heat transfer model assumes that the initial water and AuNPs temperature is $20 \text{ }^\circ\text{C}$: $T_{AuNP}(x,y,0)=T_{PSS}(x,y,0)=20 \text{ }^\circ\text{C}$. As boundary conditions this model assumes that the system is isolated and that there is continuity of temperature and heat flux at the AuNPs surface:

Boundary conditions:

- **Exterior boundary:** $q(x,y,t)=0$, where q is the heat flux

- **Boundary conditions on the particle surface:**

$$T_{AuNP}(r0,t)=T_{H2O}(r0,t),$$

$$k_{AuNP} \frac{\partial T_{AuNP}}{\partial r} \Big|_{r=r_{AuNP}} = k_{H_2O} \frac{\partial T_{H_2O}}{\partial r} \Big|_{r=r_{AuNP}}$$

As already explained, the electric field is linearly polarized in the x direction, and propagates along the y coordinate. The system is irradiated with a Gaussian beam that has a wavelength of 532 nm, a waist radius equal to twice the wavelength, and a focal point in the center of the system – where the AuNPs are situated. In these conditions, the system's field distribution (Figure 37) is calculated both in the AuNP and in their surrounding medium and is described by the following equation:

$$E_{norm} = \sqrt{E_x^2 + E_y^2}, [\text{V/m}] \quad (41)$$

Where $E_{norm}/[\text{V/m}]$ is the normal electric field.

3.5.1.2. Results and discussions

One can see from Figure 37 that in case of the AuNPs that are aligned with the polarization of the electric field, there is a strong electric field enhancement at the AuNPs surface and in its proximity. However, in case of the y oriented AuNPs, an electric field decrease is observed.

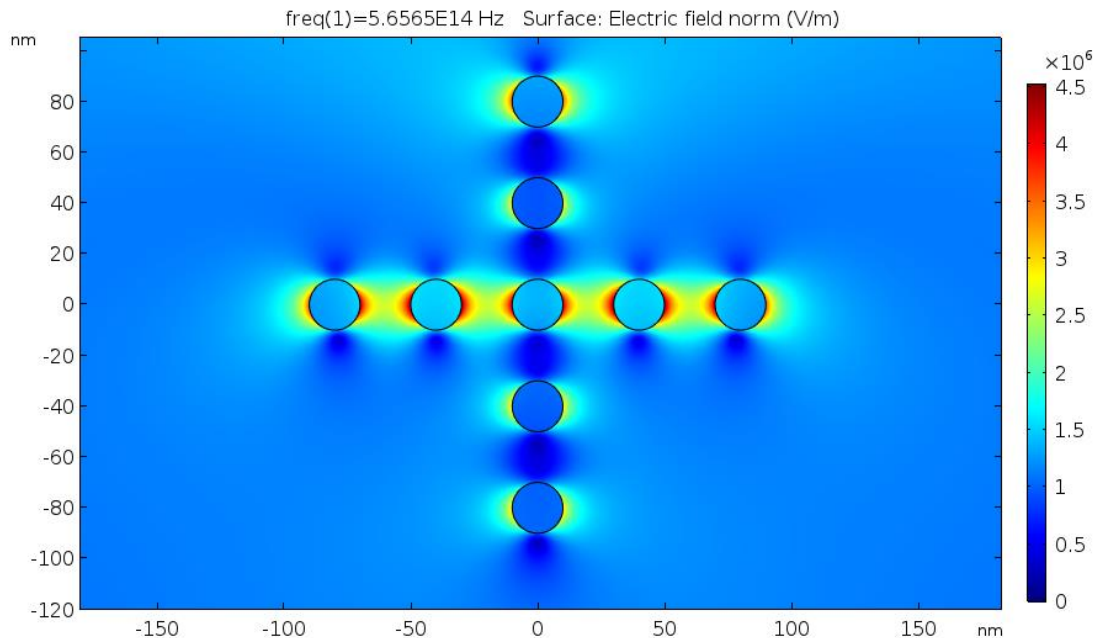


Figure 37. Zoom-in of the calculated field distribution for a laser irradiated system of 20nm AuNPs immersed in water

In Figure 38 a and b the electric field enhancement and applied electric field in x direction ($y=0$) is plotted. It can be observed that in case of x oriented AuNPs, there is a significant electric field increase at the surface of the AuNPs. The maximum value of the incident electric field is in fact E_0 and has a value of $1.22\text{E}6$ [V/m], whereas the AuNP's maximum electric field is $1.6\text{E}6$ [V/m]. In water, at the AuNPs proximity, the electric field can reach much higher values, having a maximum of $4.54\text{E}6$ [V/m]. From this image one can also see that, even though we expect to have the highest electric field in the center AuNP, this particle has a slightly diminished value, due to the interactions with the y chain of AuNPs.

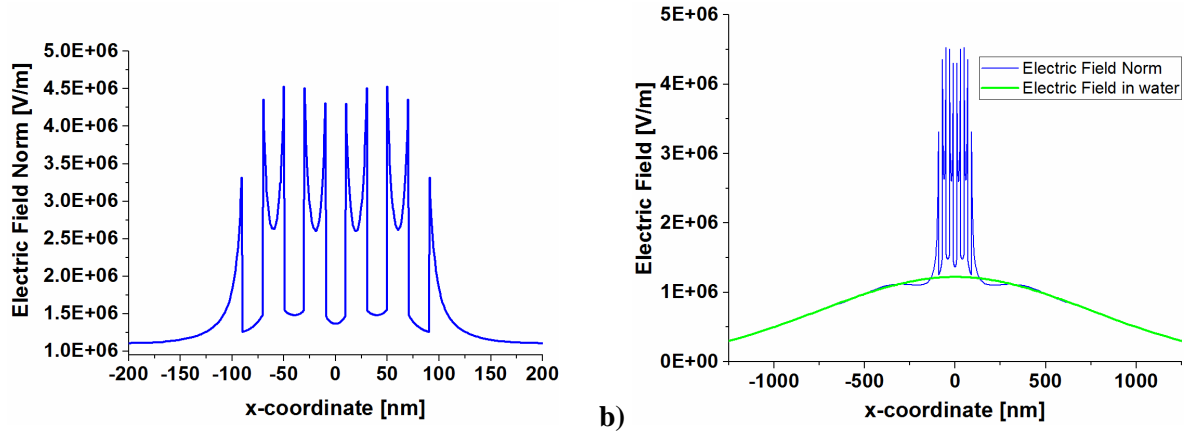


Figure 38. a)Electric field distribution in the $y=0$ along the x coordinate; b) Electric field and the electric field in water distribution in the $y=0$ along the x coordinate

The local field enhancement is given by the coherent interactions between the adjoining AuNPs, thus the induced field adds constructively to the applied field. In the same time, in case of the neighboring AuNPs that are oriented in the y direction, the scattered field adds destructively to the applied field [123].

The metallic particles heat generation and thus the system's temperature are determined based on the electric field enhancement that is developed on the AuNPs surface. The influence of the near-field interactions on the AuNPs heat can be observed in Figure 39.

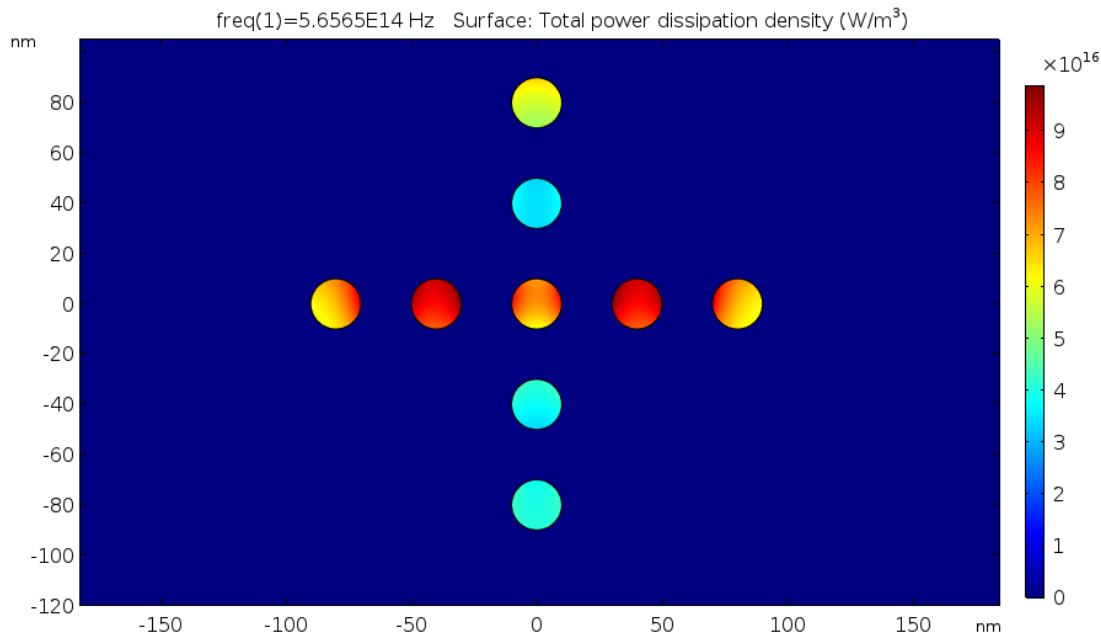


Figure 39. Zoom-in of the calculated AuNPs heat generation for the laser irradiated system

One can observe that, as in the electric field distribution, the particles that are situated in the x direction generate the highest heat (9.9060 W/m^3). This value is obtained on the NP surface, for the NPs that are situated to the right and left towards the central particle (Figure 39). The NP that is situated at the top of Figure 39, in the y oriented AuNPs chain, has higher generated heat values compared to its neighboring NP due to the fact that it is the first NP that interacts with the Gaussian beam. Moreover, in the y oriented AuNPs chain, besides the center NP which is also influenced by the NPs from the x chain, all other NPs have lower generated heat values due to the fact that the electric field ads destructively to the applied field [123].

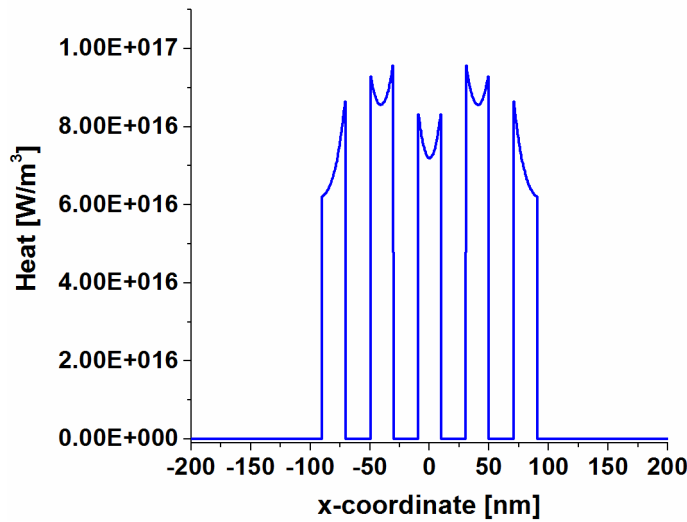


Figure 40. Generated heat in the x chain of AuNP

Based on the calculated AuNPs heat generation, the system's temperature in space and time is modeled. Figure 40 shows that even though the heat generated by the center AuNP is lower than that of its x chain neighbouring particles, only for the first 1-5 ns interval its temperature has lower values. In fact its temperature gradually grows until 20 ns when it reaches 38.7°C (Figure 41). This phenomenon can be attributed to the system's geometry - the center particle has other four NPs nearby and therefore, the temperature has less water to diffuse in.

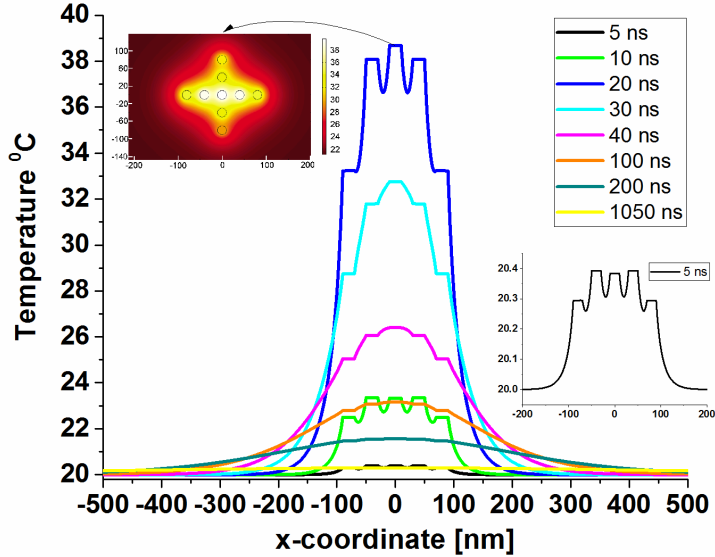


Figure 41. Temperature variation with time and x coordinate at an intensity of 3.95E05 W/cm²

In Figure 41 it can also be seen that the water significantly heated near the AuNPs, on a radius of 400 nm and that the system reaches the thermal equilibrium after 1050 ns. The thermal equilibrium is considered to be reached when relation 27 is satisfied ((T_{max}-T_{min})/T_{max} < 0.5%).

Along with the central NP temperature dynamics, Figure 42 also displays the Gaussian beam pulse profile.

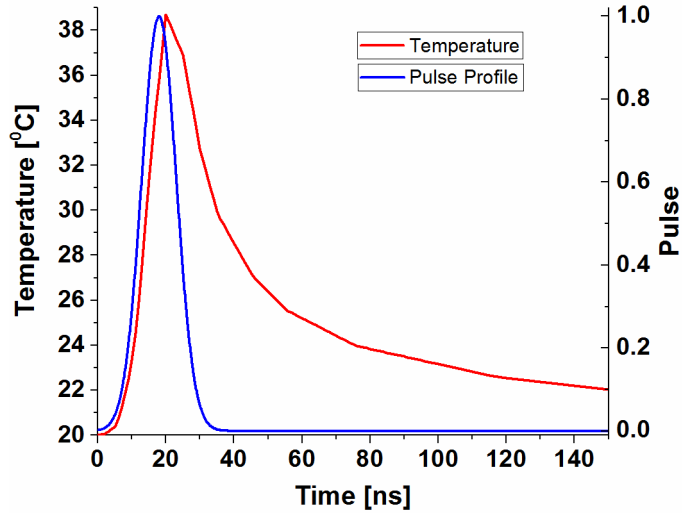


Figure 42. Temperature variation with time for the center AuNP (0,0) and the laser pulse profile
One can see that the difference between the time attributed to the maximum Gaussian beam intensity and the time attributed to the AuNP's maximum temperature is of only 2 ns. Furthermore,

while the pulse ends after 35 ns, the AuNP temperature reaches the thermal equilibrium temperature (20.35°C) after 1050 ns.

3.5.2 3D Model - The influence of near field interactions on the AuNP temperature

3.5.2.1 Methods

As general features, due to the reduced computational time, the simulations that have a two dimensional (2D) geometry have the advantage of lower computing times and memory requirements. However, the models that are constructed in a three dimensional (3D) geometry usually produce more realistic results. In this view, the influence of the AuNPs distance on the electric field enhancement and its impact on the system temperature is studied for a three dimensional geometry that consists of water embedded 20 nm spherical AuNPs. The following three systems are studied: 1) the first system (System III) has three AuNPs that are arranged along the beam polarization 2) the second system (System IV) has three AuNPs that are arranged perpendicular to the beam polarization and 3) the third system (System V) contains nine spherical AuNPs that are arranged in the xz plane in a cross-type geometry. For all cases, the surrounding matrix is represented as a cub of 1000 nm length and has an absorbing outermost layer (PML) of 500 nm.

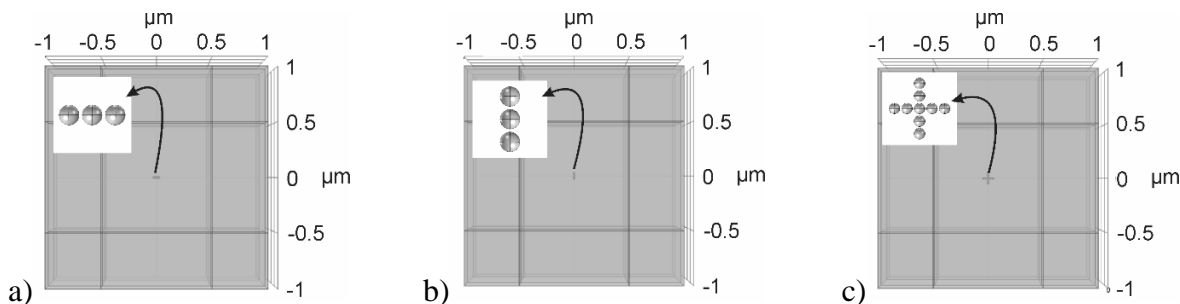


Figure 43. Geometry in xz plane of a) System III, b) System IV and c) System V

The systems are irradiated with a Nd:YAG nanosecond laser that has a Gaussian pulse of 12 ns at FWHM, 532 nm wavelength, a waist radius that is twice the wavelength and an intensity of 3.95E+05 W/cm^2 . The electric field enhancement effect, the heat generated by the irradiated AuNPs and the system's time and space temperature evolution are modeled in Comsol Multiphysics, using the “Wave Frequency Domain” and Time Dependent Heat Transfer in Solids”

modules. In order to determine the AuNPs electric field enhancement and additionally their heat generation, the wave equation (Equation 32) is solved for the AuNPs, their water surrounding medium and the outermost PML. For the 3D simulation, the incident electric field for a Gaussian beam has the following equation:

$$E(x, y, z) = E_0 \frac{\omega_0}{\omega(z)} \exp \left[-\frac{x^2 + y^2}{\omega^2(z)} - jkz - jk \frac{x^2 + y^2}{2R(z)} + j \tan \left(\frac{z - p_0}{z_0} \right) \right], [V/m] \quad (42)$$

where ω_0 is the waist radius, $\omega(y)$ is the spot radius for different positions along the y axis, z_0 is the Rayleigh range, $R(y)$ is the radius of curvature and E_0 is the initial applied electric field amplitude and has a value of 1.220616e6 [V/m].

Regarding the AuNPs heat generation, the same equation (Equation 38) as in the 2D model is used. This first simulation has as a zero electric field as initial condition and a PML that absorbs all the radiative waves with small reflections is chosen as a boundary condition.

Equations 39 and 40 that describe the system's temperature dynamics (AuNPs temperature accumulation and its transfer through conduction to the surrounding medium) are also applied for the 3D model. In terms of initial and boundary conditions, the model assumes that the system has an initial temperature of 20 °C, at the exterior boundary the system is isolated and, at the AuNP surface there is a continuity of heat flux and temperature.

3.5.2.2 Results and discussions

3.5.2.2.1 Influence of AuNP distance for 3 AuNPs embedded in water

The study of the laser irradiated cross-type spherical AuNPs modeled in the two dimensional geometry concluded that, for a 40 nm distance between two adjoining AuNPs, the AuNP orientation with respect to the laser beam polarization influences the AuNPs electric field and consequently their heat generation. The AuNPs that are oriented along the beam polarization develop a significant electric field increase at the AuNPs surface because the induced field ads constructively to the applied field. The NP chain that is oriented perpendicular to the beam polarization has an electric field diminish due to the fact that the scattered field ads destructively to the applied field [123].

Moreover, Zeng et al demonstrates that the distance between two identical particles influences the energy absorption efficiency [131]. Thereby, for two NPs that are modeled in a 2D geometry, it is demonstrated that the shorter the distance between the AuNPs, the greater the energy absorption efficiency. The highest efficiency is obtained when the two NPs touch each other [131].

For System III and System IV that are modeled in a 3D geometry, the influence of the ratio between the distance D (distance between two NP centers) and the NP diameter (d_{AuNP}) on the NPs heat generation and consequently their temperature is studied, and the results are presented in Figures 44 and 45.

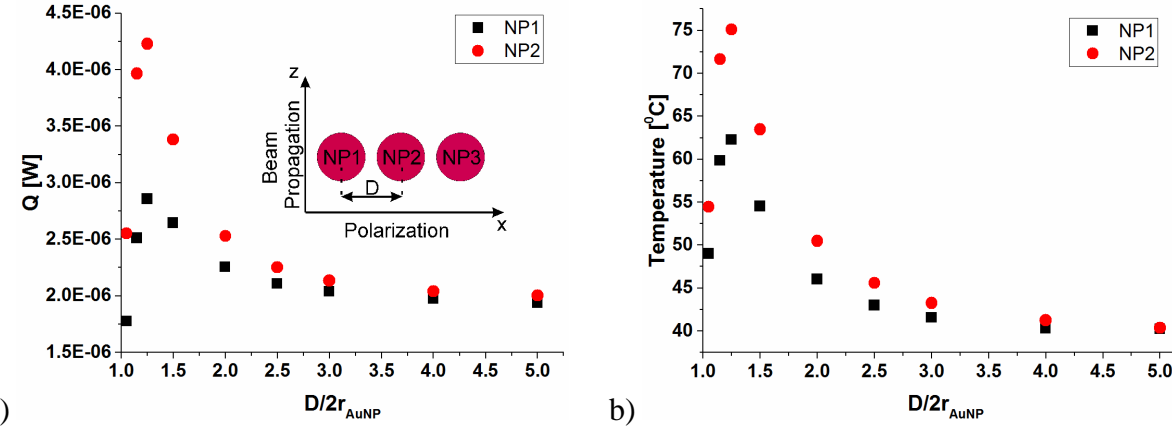


Figure 44. System III a) The influence of the D/d_{AuNP} ratio on the AuNP heat generation and b) The influence of the D/d_{AuNP} ratio on the AuNP maximum temperature

Regarding System III (Figure 44 a and b), where the laser beam propagates perpendicular to the three AuNPs, but has a polarization on the x direction (along the AuNPs), one can see that the AuNP heat generation depends not only on the NP distance D , but also on the AuNP diameter d_{AuNP} and displacement. Compared to the neighboring NPs, the center AuNP (NP2) reaches its highest generated heat when the D/d_{AuNP} ratio reaches the value of 1.25. At this NP distance, the heat generated by the center AuNP is 4.2279E-6 W, value that is 1.5 times higher than the other 2 AuNPs. Furthermore, for all metallic NPs, the generated heat drastically increases up to the D/d_{AuNP} ratio of 1.25. Afterwards, the AuNPs generated heat decreases with the D/d_{AuNP} ratio increase. The generated AuNP heat increase is attributed to the near-field interactions and to the NP arrangement. Together with the NP distance decrease, the water volume near the central NP decreases, thus, the AuNP heat has lower volume to diffuse in. When D/d_{AuNP} ratio is lower than 1.25, the AuNP heat drastically decreases with diminishing the NPs distance. This phenomenon can be explained by the AuNPs shielding effect.

From Figure 44b one can see that, similar to the generated AuNP heat, also the maximum temperature is influenced by the NP distance. All AuNPs have the highest maximum temperature at D/d_{AuNP} ratio of 1.25, the center AuNP being the one that has the highest temperature of 75 °C. At this NP distance the temperature difference between the center AuNP and the neighboring NP

is 13 degrees. Also, until the D/d_{AuNP} ratio reaches the value of 1.25, the AuNP maximum temperature drastically increases. Afterwards, the AuNPs maximum temperature decreases with the D/d_{AuNP} ratio increase. In addition, for both the AuNP heat generation and AuNP temperature, the three NPs have similar generated heat and temperature values only for AuNP distances that are greater than four times their diameter.

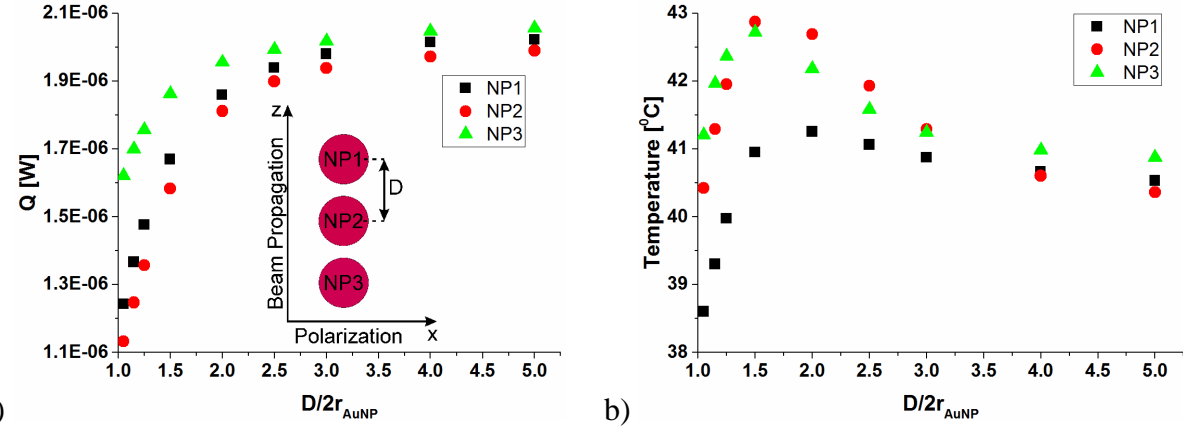


Figure 45. System IV - a) The influence of the D/d_{AuNP} ratio on the AuNP heat generation and b) The influence of D/d_{AuNP} ratio on the AuNP temperature

In System IV, where the NP are oriented perpendicular to the beam polarization, but along its direction of propagation, the decrease of the AuNP distance causes a AuNP heat generation drop (Figure 45a). This behavior can be explained by the fact that the AuNP scattered field ads destructively to the applied field. Also, for this system, the first NP that interacts with the electric field (NP3) is also the one that has the highest generated heat. In terms of heat generation, NP3 is followed by NP2, the central AuNP, and NP1, the last NP in the electric field direction of propagation. Moreover, for all three NPs, for a D/d_{AuNP} ratio less than 1.5, the heat values have a steeper slope, suggesting that, at these NP distances, the shielding effect may also be present for this NP orientation.

Figure 45b presents the influence of the D/d_{AuNP} ratio on the AuNPs maximum temperature. The highest maximum temperature for all NPs is reached at a D/d_{AuNP} ratio of 1.5. Even though, at this AuNP distance, there is a significant difference between NP2 and NP3 generated heat, the maximum temperatures of these two NPs are almost identical: $42.87\text{ }^{\circ}\text{C}$ for NP2 and $42.72\text{ }^{\circ}\text{C}$ for NP3, respectively. At this D/d_{AuNP} ratio the maximum temperature difference between the center AuNP and NP1 is $2\text{ }^{\circ}\text{C}$. Also, one can see that, compared to NP3, the center AuNP has comparable or, for some AuNP distances, even higher temperatures, despite the fact that its generated heat is

lower. This phenomena demonstrates the importance of the AuNP arrangement. The center AuNP has the lowest generated heat, but due to the NP arrangement, the heat has a smaller water volume to diffuse in, leading to a local maximum temperature increase. A greater than 1.5 D/d_{AuNP} ratio leads to an increase in the water volume near the central AuNP, thus leading to a slightly decrease of the AuNPs maximum temperature. For AuNP distances that are greater than three times their diameter, the metallic nanoparticles have similar generated heat and temperature values.

Compared to System III in which the highest maximum AuNP temperature is 75 °C, in System IV the highest maximum temperature is 43 °C. The 32 degree difference is mainly due to the AuNPs orientation with respect to the electric field polarization.

The AuNPs in System V are arranged in an identical geometry to the one in 2D cross-type model which is described in subsection 3.5.1. In this view, for the same distance between neighboring AuNP, the AuNPs electric field and generated heat behavior is identical with the 2D model. Also, for AuNPs that are oriented along and perpendicular to the beam polarization, the influence of NPs distance on the AuNPs heat generation and consequently their temperature is modeled in System III and System IV. In this view, for System V, only the influence of the D/d_{AuNP} ratio on the central AuNP (NPC) heat generation and maximum temperature is presented (Figure 46).

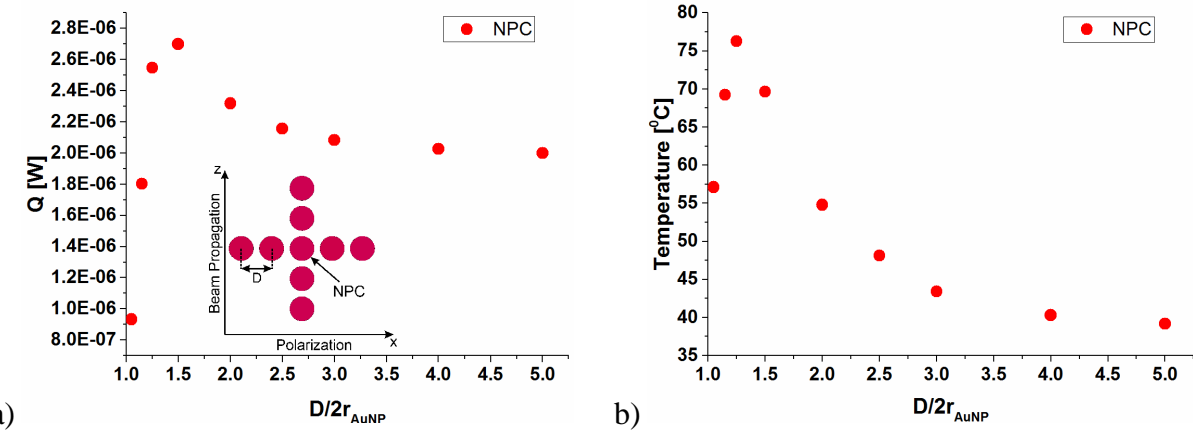


Figure 46. System V - a) The influence of the D/d_{AuNP} ratio on the AuNP heat generation and b) The influence of the D/d_{AuNP} ratio on the AuNP temperature

Similar to Systems 3 and 4, in System V, up to the D/d_{AuNP} ratio of 1.5, the center AuNP has an extremely steep heat generation growth. Even though for this distances an electric field increase should be expected, the heat generation diminish with the decrease of the AuNPs distance is caused by the scattered electric field that ads destructively to the applied field and also by the AuNPs shielding effects. For the D/d_{AuNP} ratio of 1.5, the AuNPs reach the highest generated heat value of

2.6997E-6 W. A greater than 1.5 D/d_{AuNP} ratio induces a heat generation decrease until the AuNPs distance reaches a value of four times their diameter. This is the distance from which the near-field interactions and the shielding effects no longer influence the generated heat and consequently the AuNP temperature.

Except for D/d_{AuNP} ratio that has the value of 1, along with the AuNP distance increase, the center AuNP maximum temperature follows the same trend as the heat generation. In Figure 46 a, one can see that the highest heat generation is encountered at a D/d_{AuNP} ratio of 1.5, whereas the maximum AuNP temperature is reached at a D/d_{AuNP} ratio of 1.25 (Figure 46 b). This mismatch between the AuNP generated heat and maximum temperature trends may be explained by the NPs arrangement. A greater AuNP distance implies a greater volume for the heat to diffuse in, leading, for similar AuNP heat values, to a temperature diminish.

3.5.3 The influence of AuNPs distance on the AuNP heat generation and their maximum temperature. Comparison between two modelling approaches.

3.5.3.1 Methods

The two different models that tackle the AuNPs heat generation and temperature dynamics are: i) a model in which the near-field interactions are taken into account (model A) and ii) a model that determines the AuNP heat generation based on the absorption efficiency (model B).

In this subsection, System III, System IV and System V, the results regarding the AuNPs heat generation and temperature dynamics modeled which are obtained based on model A, are compared with the results obtained by using model B. In order to compare the results obtained for the two models, the same geometry, laser parameters and the same heat transfer equation and boundary conditions are used for both approaches.

The difference between the two models consists of the heat transfer calculation. Model A solves the wave equation for a homogeneous dielectric and assumes that the generated AuNP heat is proportional to the real part of the product between the current density and the electric field complex conjugate (Equation 38). Model B assumes that the generated AuNP heat is only proportional to the absorption efficiency and the laser intensity (Equation 21). For an easier comparison, the two equations are presented as follows:

Model A	$Q_{rh} = \frac{1}{2} \operatorname{Re}[J \cdot E^*] \exp(-(t - t_0)^2/\tau^2), [\text{W/m}^3]$	(38)
------------	---	------

Where J/Am^{-2} is the current density, E^* is the complex conjugate, t/s is time, t_0/s is the Position of the center of the pulse peak and τ/s is the Gaussian pulse duration.

Model B	$Q = \frac{3K_{abs}I\exp(-{(t-t_0)^2}/{\tau^2})}{4r_{AuNP}}, [\text{W/m}^3]$	(21)
------------	--	------

Where K_{abs} is the absorption efficiency, $I/\text{W/m}^2$ is the intensity and r_{AuNP}/m is the gold nanoparticle radius.

The absorption efficiency is calculated in Comsol software, using model A. The same geometry, laser parameters and equations as in Systems 3, 4 and 5 are used. Thus, the absorption efficiency is determined for a single 20 nm spherical AuNP that is embedded in water and is irradiated with a nanosecond Nd:YAG laser. The Gaussian beam characteristics are the following: it has a 532 nm wavelength, a spot size that is double the wavelength, a $3.95E+05 \text{ W/cm}^2$ intensity and a pulse of 12 ns FWHM. Under these conditions, the absorption cross section (σ_{abs}) is calculated as follows:

$$\sigma_{abs} = \frac{P_{abs}}{I_0}, [\text{m}^2] \quad (43)$$

where $I_0/\text{W/m}^2$ is the laser intensity and $P_{abs}/\text{W/m}^3$ is the absorbed power per unit length and has the following equation:

$$P_{abs} = \iiint Q_h dx dy dz, [\text{W}] \quad (44)$$

Where Q/W is the total power dissipation energy.

As a result, for the 20 nm water embedded spherical AuNP a 503.27 nm^2 absorption cross section is obtained. The absorption efficiency is calculated with Equation 5 and its value is 1.602.

3.5.3.2 Results and discussions

The comparison between model A and model B for the three systems (System III, System IV and System V) regarding the AuNPs heat generation and maximum temperature are presented in Figures 47 and 48.

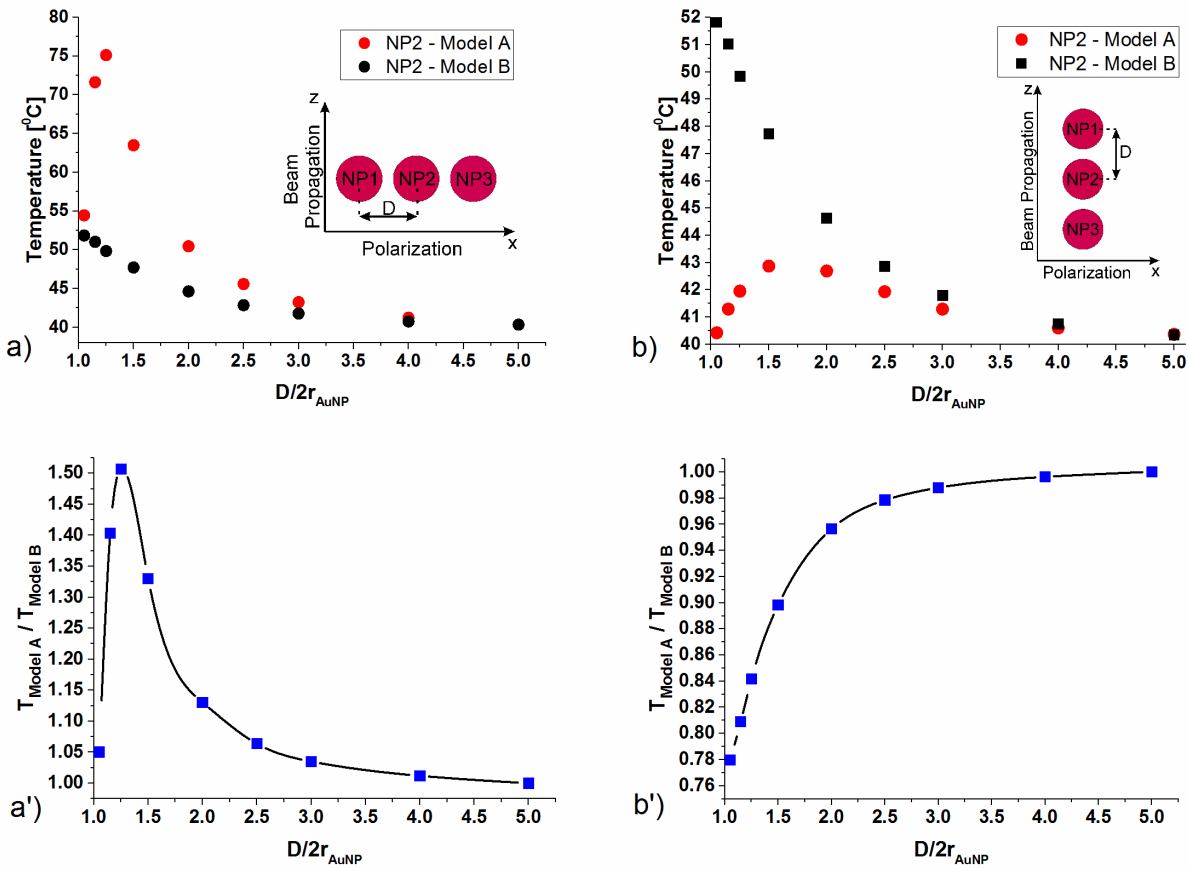


Figure 47. Model A (red dots) and model B (black dots) calculated temperatures for different D/d_{AuNP} ratios in case of System III (a) and System IV (b); The influence of AuNP distance on the ratio between the temperature calculated with model A and model B, respectively, for System III (a') and System IV (b').

Regarding System 2, one can see that model B drastically underestimates the AuNP temperature. In both modeling approaches, the NP distance influences its maximum temperature. In this regard, due to the NP distance decrease, three effects are present. The electric field interactions and the NP geometry are responsible for the temperature increase, while the shielding effect is responsible for the drastic temperature drop. The NP geometry effects are present in both systems, but its influence is better pointed out for model B, due to the fact that these effects are the only ones that cause a AuNP temperature increase that comes along with the AuNP distance diminishing. Due to the NP agglomeration, there is a smaller volume of water for the heat to diffuse in and, consequently, the temperature in the central NP increases.

Even though the shielding effect has such an important impact on the AuNP temperature decrease, at this NP distances, model B still has lower AuNP temperatures than model A. Only form NP

distances that are greater than four times the NP diameter, the two modelling approaches reach similar temperatures. This behavior is better highlighted in Figure 47 a', where the influence of D/d_{AuNP} ratio on the T_{modelA}/T_{modelB} ratio is studied. One can see that T_{modelA}/T_{modelB} ratios that have a value close to 1 are reached only for NP distances that are four times the NP diameter. In comparison to System III, in System IV, for the central AuNP, model B approach generates higher AuNP temperatures. Again, this model does not take into consideration the destructive interactions that occur between the AuNPs. One can see in Figure 47 b, T_{modelA}/T_{modelB} ratios that are around the value of 1 are encountered only for large AuNP distances. As a result, the approach in which the AuNP heat generation and temperature dynamics is modeled only by calculating the absorption cross section can be used only for diluted AuNPs solutions, in which the NP distance is greater than four times their diameter.

Compared to Systems 3 and 4, System V has a cross-type AuNP arrangement, geometry that resembles more to the displacement of AuNPs in a real system, having all three effects present. As for the other two systems, the influence of D/d_{AuNP} ratio on the central AuNP temperature is studied with both modelling approaches (Figure 48a). Also the influence of AuNP distance on the ratio between the central AuNP temperature obtained with model A and model B is studied (Figure 48b).

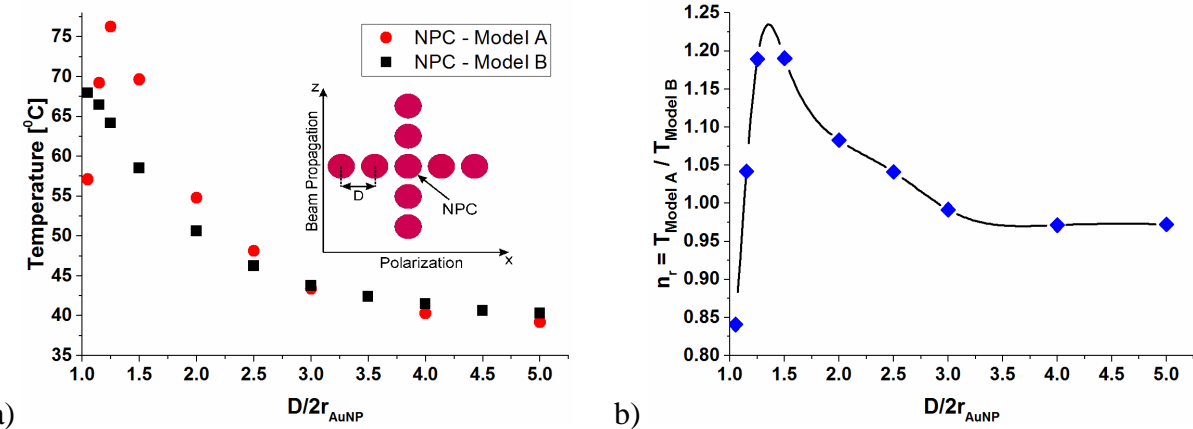


Figure 48. System V – a) Model A (red dots) and model B (black dots) calculated temperatures for different D/d_{AuNP} ratios; b) The influence of AuNP distance on the ratio between the temperature calculated with model A and model B, respectively.

For almost touching AuNPs (D/d_{AuNP} ratios < 1.25), the maximum temperatures calculated with model B are higher than the ones obtained with model A. Conversely, for D/d_{AuNP} ratios that are situated between 1.05 and 3, the maximum temperatures obtained with model B are lower than

those obtained with model A. Almost identical maximum temperature values are obtained only if the D/d_{AuNP} ratio is greater than 3.

As a result, the model that takes into account the absorption cross section is valid only for aqueous AuNP solutions in which the distance between any two AuNPs is greater than three times its diameter. In an aqueous AuNP solution this AuNP distance corresponds to a concentration of 3.7037e16 particles/m³.

Even though for the temperature dynamics modelling model A is more accurate, model B is easier to implement and requires less memory requirements. Thus, for AuNP concentrations that are less than 3.7e16 particles/m³, the AuNP temperatures obtained with model B should be calculated as follows:

$$T = n_r T_{modelB} \quad (45)$$

where n_r (Figure 48b) is the ratio between the maximum temperature calculated with model A and model B.

3.6 Conclusions Part B

In this work we studied the temperature dynamics in various systems that are irradiated with a pulsed laser which has a Gaussian pulse of 12 ns at FWHM, 532 nm wavelength and an intensity of 3.95E+05 W/cm². The most appropriate tool to determine the space/time evolution of the temperature inside such a system is mathematical modeling using finite element method. In this view, the temperature distribution in time and space is calculated by solving the heat diffusion equations with appropriate initial and boundary conditions. The influence of particle size, number and their displacement in the surrounding matrix as well as the influence of the interfacial thermal conductance is studied by using a model that calculates the system temperature based on the nanoparticle absorption cross section. In addition, the effect of AuNPs near-field interactions, their orientation regarding the electric field polarization and the AuNPs distance on their heat generation and maximum temperature is studied by solving both the wave and the heat transfer equations. Finally, the impact of the two modelling approaches on the AuNP heat generation is studied.

The temperature evolution in time and space is obtained for AuNPs of 20 nm, 30 nm and 40 nm diameter embedded in a polystyrene sulfonic acid matrix. This system resembles experimentally with an aqueous AuNP solution in which there is a substantial distance between the nanoparticles. It is observed that the increase of the AuNP diameter determines a rise of the AuNP temperature and, implicitly, the rise of the entire system temperature. Also, the NP temperature rise determines

an increase in the necessary time to reach the systems thermal equilibrium. These effects are correlated to both an increase in the spherical NP generation of heat and a decrease in the heat diffusion volume.

Further on we performed a comparison between one 20 nm AuNP and an infinite system of AuNPs embedded and randomly distributed in a PSS matrix. The obtained results highlight the importance of taking into consideration an infinite system, for the reason that this system reach higher temperatures in a longer period of time. Also, the infinite system of randomly distributed AuNPs needs a much larger period of time to reach the thermal equilibrium.

The impact of AuNPs displacement on the temperature dynamics of an infinite system that contains AuNPs is studied for 20 nm spherical NP distributed in four different geometries: an array, a concentric, a radial and a random AuNP distribution. The different arrangements of the NPs in the polymer matrix plays a significant role in the temperature distribution and in the dynamics of the system towards reaching thermal equilibrium. The more agglomerated the AuNPs are the higher the temperature near that area and the longer the time to reach the thermal equilibrium.

For the four AuNPs geometries that simulate an infinite system of PSS embedded AuNPs, we investigated the influence of the thermal property mismatch between the AuNP and the surrounding medium. The results demonstrate that there are cases in which the interface thermal conductance can not be neglected. In these cases the AuNPs thermal decay is achieved in a longer time, phenomenon that leads to higher temperatures in the AuNPs and in the nearby polymer, and, consequently higher maximum temperatures in the system. As expected, the system that is mostly influenced by the thermal property mismatch is the radial distribution.

Modeling the influence of near-field interactions on the water embedded AuNPs temperature requires, before solving the heat transfer equation, also solving the wave equation for an electromagnetic pulse propagating in an optically inhomogenous medium.

A first study models the near-field interactions between nine AuNPs that are arranged in a cross-type arrangement. For less memory requirements and thus a faster computation, the model is developed in a two dimensional geometry. The results indicate that the AuNPs layout with respect to the polarization of the electric field plays an important role in establishing the propagated field and the heat generation. The system temperature distribution is strongly influenced by the electric

field enhancement that is developed on the AuNPs surface. Depending on the AuNP orientation the AuNP scattered electric field adds constructively or destructively to the applied field. Consequently, the metallic NPs that are oriented parallel to the electric field polarization generate much more heat than the ones oriented perpendicular to the electric field. Even though the central AuNP does not have the highest generated heat, the maximum temperature in this cross-type AuNP system is reached in this particle, phenomenon that is attributed to the system's geometry (the center particle has other four NPs nearby and therefore, the temperature has less water to diffuse in).

The influence of the gold nanoparticle distance on the AuNP near-field effects, heat generation and temperature enhancement is studied for the cross-type system and for other two less complicated systems that have a chain of three AuNPs oriented parallel and perpendicular to the electric field polarization. For more accurate results these three cases are modeled in a three dimensional geometry.

For the case in which the AuNP chain is oriented along the electric field polarization, the results demonstrate that the highest generated heat and, therefore, the highest temperature is reached in the AuNP, when the distance between the NPs centers is 1.25 times higher than their diameter. The AuNP heat decreases with the increase of the distance between the NPs, and reaches a similar heat when the distance is greater than four times their diameter. On the other hand, when the distance is smaller than 1.25 their diameter, due to the shielding effects, the AuNPs heat drastically decreases. In respect to the AuNP temperature, we mention that it follows the same trend as the heat generation.

In the system that has the AuNP chain oriented perpendicular to the electric field polarization, the highest generated heat develops in the first particle situated in the direction of beam propagation. Also, for all AuNP distances, the center AuNP has the lowest heat generation values. Furthermore, the heat generation for all three particles increases with the NP distance increase, having a more pronounced rise for NP distances that range between 1 and 1.5 times the NP diameter. For this AuNP arrangement, the temperature increase does not follow the heat generation trend. For all three NPs, the temperature increases until distances that are 1.5 times higher the AuNPs diameter, whereas for greater NP distances, the metallic NP temperature decreases. Also, the center AuNP and the one that is firstly situated in the beam propagation direction have similar temperatures.

In terms of the AuNP maximum temperature, the AuNPs oriented parallel to the electric field polarization have higher temperatures than those oriented perpendicular to the electric field polarization. Therefore, we may conclude that the electric field polarization has a significant influence on the AuNPs temperature.

Regarding the cross-type geometry, the AuNP heat generation has a steep growth until the AuNP distance that is equal to 1.5 times the NP diameter. For greater distances, the heat generation diminishes until the AuNPs distance reaches a value of four times their diameter. This is the distance from which the near-field interactions and the shielding effects no longer influence the generated heat and consequently the AuNP temperature.

In conclusion, depending on the AuNP distance, the NPs heat generation is influenced by the shielding effects and near-field effects. In addition to these effects, the AuNPs maximum temperature is also influenced by geometry effects.

The impact of the two modelling approaches on the AuNP maximum temperature is studied for various AuNPs distances, considering the cross-type AuNPs arrangement. The differences between the two models are presented only for the center AuNP, this case being the one that most closely resembles to the displacement of particles in a real system. The two models have almost identical maximum temperatures only for AuNP distances that are greater than three times the particle diameter. In an aqueous AuNP solutions this AuNP distance corresponds to a concentration of $3.7e16$ particles/m³. Therefore, the model that takes into account the absorption cross section is valid only for aqueous AuNP solutions that have a AuNP concentration less than $3.7e16$ particles/m³.

In consequence, due to the fact that the model that calculates the system temperature based on the nanoparticle absorption cross section is easier to implement and necessitates less memory requirements, a relation for determining a more accurate AuNP temperature is deduced.

General conclusions

In this work, original results that concern two aspects of the photochemical generation of AuNPs, are presented: 1) the synthesis and modeling of the gold nanoparticles photochemical generation process and 2) the heat generation and heat transfer of the laser irradiated AuNPs that are embedded in polymer and aqueous matrixes.

For obtaining these results both experimental and theoretical methods were applied. The thesis main original contributions to the AuNPs generation process and their heat generation are presented as follows:

1. Stable and reproducible AuNPs in thick polymer films are photochemically generated by using a direct light writing method and the main factors that influence the AuNPs dimension are determined to be: the citrate: Au^{3+} ratio, radiation intensity and scanning velocity.
2. The real dimension of the embedded AuNPs is estimated using an exponential fit that is obtained based on the TEM measured AuNPs mean diameters and their corresponding localized SPR absorption maxima measured in thick film.
3. For the first time, an ANN is developed to predict the AuNPs diameter. Based on this model the influence of the citrate: Au^{3+} ratio, radiation intensity and scanning velocity on the AuNPs diameter is investigated. Thus, it is demonstrated that the AuNPs size increases with the increase of the scanning velocity and a decrease in the radiation intensity. Also, higher citrate: Au^{3+} ratios lead to bigger AuNPs, implying that higher Au^{3+} concentrations result in a decrease of the AuNPs dimension.
4. Using the Garson and Goh method that relies on the ANN model, the relative impact of each process parameter on the particle size is evaluated. It is determined that the radiation intensity has a relative importance of 40%, being thus the factor that most influences the AuNPs size. The scanning velocity and the citrate: Au^{3+} ratio have a similar relative importance, the scanning velocity having a slightly higher value of 31% in comparison with the citrate: Au^{3+} ratio which has a value of 29%.

5. The ANN input variable importance is also examined using a feature selection algorithm that finds the subsets of features which optimally predict the measured data, revealing the features that are most influential. The same ordering as for the Garson and Goh method is determined.
6. The space/time evolution of the temperature inside systems that consist of AuNPs embedded in a polymer matrix is mathematically modeled using the finite element method. The temperature distribution in time and space is calculated with Comsol software, in a 3D geometry, by solving the heat diffusion equations with appropriate initial and boundary conditions. An infinite system (macro system) that has four different AuNPs distributions is simulated by imposing periodic boundary conditions.
7. It is demonstrated that for describing the temperature evolution in such a system is important to take into consideration the macro system, not just one NP. The AuNPs size and distribution can also drastically influence the system's temperature dynamics.
8. The macro system with the four AuNPs distributions is compared with a model that is adapted to take into account the thermal property mismatch. It is determined that this material mismatch can not be neglected in the radial, concentric and random AuNP distributions, where the interfacial thermal conductance mostly influences the AuNPs temperature.
9. The 3D mathematical model is also adapted to calculate the temperature dynamics of an aqueous solution of AuNPs. The AuNPs are displaced in a cross-type system and, a less complicated systems that has a chain of three AuNPs oriented parallel and perpendicular to the electric field polarization. The temperature distribution in time and space is calculated by solving both the wave equation for an electromagnetic pulse propagating in an optically inhomogenous medium and the heat diffusion equations with appropriate initial and boundary conditions.

10. For the cross-type and chain of AuNPs systems it is determined that the AuNPs temperature is influenced by: i) the AuNPs distance, ii) the electric field polarization and c) the AuNPs displacement.
11. For the first time it is demonstrated that the distance between the AuNPs influences their temperature through three effects: the shielding effect, the near field effect and the AuNPs displacement regarding the beam propagation (geometry effect). It is determined that the shielding effect is encountered at NPs distances that are less than 1.5 times their diameter and is responsible for the drastic decrease of the AuNPs temperature. The near field effects are encountered at NPs distances that are less than 4 times their diameter and, depending on the polarization, are responsible for either decreasing or drastically increasing the AuNPs temperature. The AuNPs displacement regarding the beam propagation is also important due to the fact that, in a row of particles, the first NP that interact with the laser beam will have the highest temperature.
12. It is determined that the three effects drastically influence the AuNPs temperature only for distances that are lower than 4 times the AuNPs diameter. In consequence, it is demonstrated that in an aqueous solution of 20 nm spherical AuNPs, the shielding effect, the near field effect and the geometry effect influence the system's temperature only for AuNPs concentrations that are greater than $3.7e16$ particles/m³.
13. For the cross-type geometry the model that solves only the heat equation and the one that solves both the wave and heat equations are compared. It is observed that the model that only solves the heat equations is easier to implement and necessitates less memory requirements. It is found that, for AuNPs concentrations that are greater than $3.7e16$ particles/m³, the model that also solves the wave equation is more realistic.
14. As a result of the two model comparison, a relation for determining a more accurate AuNP temperature with the model that only solves the heat equation is deduced.

We appreciate the generated DLW gold nanoparticulate patterns can represent the starting point for the design of different types of materials with interesting properties, opening new solutions in AuNPs size dependent applications such as optical filters as well as substrates for biosensing detection.

We also appreciate that instead of the usual trial and error approach for generating the desired nanoparticles dimension, the fast and easy method to predict the AuNP size can be used. Moreover, knowing the influence and relative impact of each process parameter on the AuNPs size can lead to a better understanding and control of the NPs generation process.

The modeled thermal behavior of the laser irradiated AuNPs provides crucial information about the temperature distribution control and can prevent undesirable processes such as film deterioration, or in some cases ablation.

We appreciate that this thesis helps in understanding the DLW photochemical synthesis of AuNPs and can be a starting point for controlling this process.

The results listed above are presented in two ISI articles, three conferences and one summer school.

ISI Articles:

A. M. M. Gherman, N. Tosa, M. V. Cristea, V. Tosa, S. Porav and P. S. Agachi, Artificial neural networks modelling of the parameterized gold nanoparticles generation through photo-induced process, Materials Research Express 5 (2018), 085011, 1-13.

A. M. M. Gherman, N. Tosa, D. N. Dadarlat, V. Tosa, M. V. Cristea, and P. S. Agachi, Temperature dynamics of laser irradiated gold nanoparticles embedded in a polymer matrix, Thermochimica Acta, 656 (2017), 25-31.

Conferences:

A.M.M.Gherman, N.Tosa, D.Dadarlat, M.Cristea, V.Tosa, P.S. Agachi, "Time Dependent Temperature Evolution in Laser Irradiated Gold Nanoparticles Doped Matrix", Applied Nanotechnology and Nanoscience International Conference, 5-7 November 2015, Paris, France – Poster presentation.

A.M.M. Gherman, V.Tosa, N. Tosa, P.S Agachi, "Near field effects and temperature dynamics of laser irradiated gold nanoparticles", 15th UK Heat Transfer Conference, 4-5 September 2017, London, UK, Proceeding Paper and Poster

A.M.M Gherman, N.Tosa, N.D Dadarlat, V. Tosa, M.V. Cristea, P.S. Agachi, "Nanosecond Laser PhotoInduced Heating of Gold Nanoparticles Embedded in a Polymer Matrix - the Influence of Interface Conductance", Processes in Isotopes and Molecules Conference, 27-29 September 2017, ClujNapoca, Romania – Poster presentation.

Summer School:

A.M.M. Gherman, N. Tosa, D. Dadarlat, V. Tosa, P.S. Agachi, "Temperature Evolution in a Laser Irradiated System of one/a periodic array of Gold Nanoparticles Embedded in a Polymer Matrix", 5th International School Lasers in Materials Science, Isola di San Servolo, Venetia, 10-17 July, 2016 –Poster presentation.

References

- [1] C. Binns, Introduction to Nanoscience and Nanotechnology, Wiley, (2010).
- [2] G. Schmid, Nanotechnology, Principles and Fundamentals, Wiley-VCH Verlag GmbH, Weinheim, Germany, (2008).
- [3] X. Huang, M.A. El-Sayed, Gold nanoparticles: Optical properties and implementations in cancer diagnosis and photothermal therapy, *J. Adv. Res.* 1 (2010) 13–28. doi:10.1016/j.jare.2010.02.002.
- [4] E. Boulais, R. Lachaine, A. Hatef, M. Meunier, Plasmonics for pulsed-laser cell nanosurgery: Fundamentals and applications, *J. Photochem. Photobiol. C Photochem. Rev.* 17 (2013) 26–49. doi:10.1016/j.jphotochemrev.2013.06.001.
- [5] Y. Hou, Z. Sun, W. Rao, J. Liu, Nanoparticle-mediated cryosurgery for tumor therapy, *Nanomedicine Nanotechnology, Biol. Med.* (2017). doi:10.1016/j.nano.2017.11.018.
- [6] P. Ghosh, G. Han, M. De, C.K. Kim, V.M. Rotello, Gold nanoparticles in delivery applications, *Adv. Drug Deliv. Rev.* 60 (2008) 1307–1315. doi:10.1016/j.addr.2008.03.016.
- [7] N.K. Rajendran, S.S.D. Kumar, N.N. Houreld, H. Abrahamse, A review on nanoparticle based treatment for wound healing, *J. Drug Deliv. Sci. Technol.* (2018). doi:10.1016/j.jddst.2018.01.009.
- [8] G. Schmalz, R. Hickel, K.L. van Landuyt, F.X. Reichl, Nanoparticles in dentistry, *Dent. Mater.* 33 (2017) 1298–1314. doi:10.1016/j.dental.2017.08.193.
- [9] X. He, H.M. Hwang, Nanotechnology in food science: Functionality, applicability, and safety assessment, *J. Food Drug Anal.* 24 (2016) 671–681. doi:10.1016/j.jfda.2016.06.001.
- [10] E. Hutter, D. Maysinger, Gold-nanoparticle-based biosensors for detection of enzyme activity, *Trends Pharmacol. Sci.* 34 (2013) 497–507. doi:10.1016/j.tips.2013.07.002.
- [11] Y. Li, H.J. Schluesener, S. Xu, Gold nanoparticle-based biosensors, *Gold Bull.* 43 (2010) 29–41. doi:10.1007/BF03214964.
- [12] J. Liu, Y. Lu, Colorimetric Biosensors Based on DNAzyme-Assembled Gold Nanoparticles, 14 (2004).
- [13] U.J. Krull, Biosensing with Quantum Dots: A Microfluidic Approach, 2011. doi:10.3390/s111009732.
- [14] I.L. Medintz, A.R. Clapp, H. Mattoussi, E.R. Goldman, B. Fisher, J.M. Mauro, Self-assembled nanoscale biosensors based on quantum dot FRET donors, *Nat. Mater.* 2 (2003) 630–638. doi:10.1038/nmat961.
- [15] J.B. Haun, T. Yoon, H. Lee, R. Weissleder, Magnetic nanoparticle biosensors, (2010) 291–304. doi:10.1002/wnan.84.
- [16] K. Niska, E. Zielinska, M.W. Radomski, I. Inkielewicz-Stepniak, Metal nanoparticles in dermatology and cosmetology: Interactions with human skin cells, *Chem. Biol. Interact.* (2017). doi:10.1016/j.cbi.2017.06.018.
- [17] S.Z. Mousavi, S. Nafisi, H.I. Maibach, Fullerene nanoparticle in dermatological and cosmetic applications, *Nanomedicine Nanotechnology, Biol. Med.* 13 (2017) 1071–1087. doi:10.1016/j.nano.2016.10.002.
- [18] J. Pardeike, A. Hommoss, R.H. Müller, Lipid nanoparticles (SLN, NLC) in cosmetic and pharmaceutical dermal products, *Int. J. Pharm.* 366 (2009) 170–184. doi:10.1016/j.ijpharm.2008.10.003.
- [19] K. Luo, D.H. Chae, Z. Yao, Room-temperature single-electron transistors using alkanedithiols, *Nanotechnology* 18 (2007). doi:10.1088/0957-4484/18/46/465203.
- [20] J.E. Millstone, D.F.J. Kavulak, C.H. Woo, T.W. Holcombe, E.J. Westling, A.L. Briseno, M.F. Toney, J.M.J. Fr, S. Synchrotron, R. Lightsource, M. Park, Synthesis , Properties , and Electronic Applications of Size-Controlled Poly (3-hexylthiophene) Nanoparticles, 26 (2010) 13056–13061. doi:10.1021/la1022938.
- [21] P. Avouris, Z. Chen, V. Perebeinos, Carbon-based electronics, (2007) 605–615.
- [22] A. Kosmala, R. Wright, Q. Zhang, P. Kirby, Synthesis of silver nano particles and fabrication of

- aqueous Ag inks for inkjet printing, *Mater. Chem. Phys.* 129 (2011) 1075–1080. doi:10.1016/j.matchemphys.2011.05.064.
- [23] W. Wu, Inorganic nanomaterials for printed electronics: a review, *Nanoscale*. 9 (2017) 7342–7372. doi:10.1039/C7NR01604B.
- [24] I. Khan, K. Saeed, I. Khan, Nanoparticles: Properties, applications and toxicities, *Arab. J. Chem.* (2017). doi:10.1016/j.arabjc.2017.05.011.
- [25] B. Issa, I.M. Obaidat, B.A. Albiss, Y. Haik, Magnetic nanoparticles: Surface effects and properties related to biomedicine applications, *Int. J. Mol. Sci.* 14 (2013) 21266–21305. doi:10.3390/ijms141121266.
- [26] Vincenzo Amendola and Roberto Pilot and Marco Frasconi and Onofrio M Maragò and Maria A Iati, Surface plasmon resonance in gold nanoparticles: a review, *J. Phys. Condens. Matter*. 29 (2017) 203002. <http://stacks.iop.org/0953-8984/29/i=20/a=203002>.
- [27] C. Louis, O. Pluchery, Gold nanoparticles for physics, chemistry and biology, Imperial College Press, 2012. https://books.google.co.uk/books?id=4zK6CgAAQBAJ&dq=physical+vapour+deposition+nanoarticles&source=gbs_navlinks_s.
- [28] S.A. Maier, *Plasmonics: Fundamentals and Applications*, Springer Science+Business Media LLC, 2007.
- [29] M.C.M. Daniel, D. Astruc, Gold Nanoparticles: Assembly, Supramolecular Chemistry, Quantum-Size Related Properties and Applications toward Biology, Catalysis and Nanotechnology, *Chem. Rev.* 104 (2004) 293–346. doi:10.1021/cr030698.
- [30] L. Soares, A. Csáki, J. Jatschka, W. Fritzsche, O. Flores, R. Franco, E. Pereira, Localized surface plasmon resonance (LSPR) biosensing using gold nanotriangles: detection of DNA hybridization events at room temperature, *Analyst*. 139 (2014) 4964–4973. doi:10.1039/C4AN00810C.
- [31] M. Peixoto de Almeida, E. Pereira, P. Baptista, I. Gomes, S. Figueiredo, L. Soares, R. Franco, Gold Nanoparticles as (Bio)Chemical Sensors, *Compr. Anal. Chem.* 66 (2014) 529–567. doi:10.1016/B978-0-444-63285-2.00013-4.
- [32] S. Barbosa, A. Agrawal, L. Rodríguez-Lorenzo, I. Pastoriza-Santos, R.A. Alvarez-Puebla, A. Kornowski, H. Weller, L.M. Liz-Marzán, Tuning size and sensing properties in colloidal gold nanostars, *Langmuir*. 26 (2010) 14943–14950. doi:10.1021/la102559e.
- [33] S. Link, M.A. El-Sayed, Size and Temperature Dependence of the Plasmon Absorption of Colloidal Gold Nanoparticles, *J. Phys. Chem. B*. 103 (1999) 4212. doi:10.1021/jp984796o.
- [34] H.-W.W. Cheng, Z.R. Skeete, E.R. Crew, S. Shan, J. Luo, C.-J.J. Zhong, Synthesis of Gold Nanoparticles, Elsevier, 2014. doi:10.1016/B978-0-444-63285-2.00002-X.
- [35] S. Link, M.A. El-Sayed, Spectral Properties and Relaxation Dynamics of Surface Plasmon Electronic Oscillations in, *J. Phys. Chem. B*. 103 (1999) 8410–8426. doi:10.1021/jp9917648.
- [36] C.S. Ah, Y.J. Yun, H.J. Park, W.J. Kim, D.H. Ha, W.S. Yun, Size-controlled synthesis of machinable single crystalline gold nanoplates, *Chem. Mater.* 17 (2005) 5558–5561. doi:10.1021/cm051225h.
- [37] G. Dacarro, P. Pallavicini, S.M. Bertani, G. Chirico, L. D’Alfonso, A. Falqui, N. Marchesi, A. Pascale, L. Sironi, A. Taglietti, E. Zuddas, Synthesis of reduced-size gold nanostars and internalization in SH-SY5Y cells, *J. Colloid Interface Sci.* 505 (2017) 1055–1064. doi:10.1016/j.jcis.2017.06.102.
- [38] C.J. Murphy, A.M. Gole, S.E. Hunyadi, C.J. Orendorff, One-dimensional colloidal gold and silver nanostructures, *Inorg. Chem.* 45 (2006) 7544–7554. doi:10.1021/ic0519382.
- [39] H.L. Wu, C.H. Kuo, M.H. Huang, Seed-mediated synthesis of gold nanocrystals with systematic shape evolution from cubic to trisoctahedral and rhombic dodecahedral structures, *Langmuir*. 26 (2010) 12307–12313. doi:10.1021/la1015065.
- [40] A.O. Govorov, H. Zhang, H.V. Demir, Y.K. Gun’Ko, Photogeneration of hot plasmonic electrons with metal nanocrystals: Quantum description and potential applications, *Nano Today*. 9 (2014) 85–101. doi:10.1016/j.nantod.2014.02.006.
- [41] P.K. Jain, K.S. Lee, I.H. El-Sayed, M.A. El-Sayed, Calculated absorption and scattering properties

- of gold nanoparticles of different size, shape, and composition: Applications in biological imaging and biomedicine, *J. Phys. Chem. B.* 110 (2006) 7238–7248. doi:10.1021/jp057170o.
- [42] K.M. Mayer, J.H. Hafner, A.À. Antigen, Localized surface plasmon resonance sensors, *Chem. Rev.* 111 (2011) 3828–3857. doi:10.1021/cr100313v.
- [43] K.M. Mayer, S. Lee, H. Liao, B.C. Rostro, A. Fuentes, P.T. Scully, C.L. Nehl, J.H. Hafner, A label-free immunoassay based upon localized surface plasmon resonance of gold nanorods, *ACS Nano.* 2 (2008) 687–692. doi:10.1021/nn7003734.
- [44] S. Link, M.A. El-Sayed, Simulation of the Optical Absorption Spectra of Gold Nanorods as a Function of Their Aspect Ratio and the Effect of the Medium Dielectric Constant, *J. Phys. Chem. B.* 109 (2005) 10531–10532. doi:10.1021/jp058091f.
- [45] C. Bai, M. Liu, Implantation of nanomaterials and nanostructures on surface and their applications, *Nano Today.* 7 (2012) 258–281. doi:10.1016/j.nantod.2012.05.002.
- [46] A. Mocanu, I. Cernica, G. Tomoaia, L.D. Bobos, O. Horovitz, M. Tomoaia-Cotisel, Self-assembly characteristics of gold nanoparticles in the presence of cysteine, *Colloids Surfaces A Physicochem. Eng. Asp.* 338 (2009) 93–101. doi:10.1016/j.colsurfa.2008.12.041.
- [47] S. Aryal, B.K.C. Remant, N. Dharmaraj, N. Bhattachari, C.H. Kim, H.Y. Kim, Spectroscopic identification of SAu interaction in cysteine capped gold nanoparticles, *Spectrochim. Acta - Part A Mol. Biomol. Spectrosc.* 63 (2006) 160–163. doi:10.1016/j.saa.2005.04.048.
- [48] S. Zeng, K.-T. Yong, I. Roy, X.-Q. Dinh, X. Yu, F. Luan, A Review on Functionalized Gold Nanoparticles for Biosensing Applications, *Plasmonics.* 6 (2011) 491–506. doi:10.1007/s11468-011-9228-1.
- [49] R. Baron, M. Zayats, I. Willner, Dopamine-, L-DOPA-, adrenaline-, and noradrenaline-induced growth of Au nanoparticles: Assays for the detection of neurotransmitters and of tyrosinase activity, *Anal. Chem.* 77 (2005) 1566–1571. doi:10.1021/ac048691v.
- [50] K. Saha, S. Agasti, C. Kim, X. Li, V. Rotello, Gold Nanoparticles in Chemical and Biological Sensing, *Chem. Rev.* 112 (2012) 2739–2779. doi:10.1021/cr2001178.
- [51] E.C. Dreaden, A.M. Alkilany, X. Huang, C.J. Murphy, M.A. El-Sayed, The golden age: gold nanoparticles for biomedicine, *Chem. Soc. Rev.* 41 (2012) 2740–2779. doi:10.1039/C1CS15237H.
- [52] J. Turkevich, P.C. Stevenson, J. Hiller, a Study of the Nucleation and Growth Processes IN the Synthesis of Colloidal Gold, *Discuss. Faraday Soc.* 11 (1951) 55–75. doi:10.1039/DF9511100055.
- [53] G. FRENS, Controlled Nucleation for the Regulation of the Particle Size in Monodisperse Gold Suspensions, *Nat. Phys. Sci.* 241 (1973) 20–22. doi:10.1038/physci241020a0.
- [54] S.D. Perrault, W.C.W. Chan, Synthesis and Surface Modification of Highly Monodispersed, Spherical Gold Nanoparticles of 50-200 (vol 131, pg 17042, 2009), *J. Am. Chem. Soc.* 132 (2010) 11824. doi:10.1021/ja907069u.
- [55] D.T. Nguyen, D.J. Kim, K.S. Kim, Controlled synthesis and biomolecular probe application of gold nanoparticles, *Micron.* 42 (2011) 207–227. doi:10.1016/j.micron.2010.09.008.
- [56] N.R. Jana, L. Gearheart, C.J. Murphy, Seeding Growth for Size Control of 5 - 40 nm Diameter Gold Nanoparticles, *Langmuir.* 17 (2001) 6782–6786. doi:10.1021/la0104323.
- [57] K. Mallick, Z.L. Wang, T. Pal, Seed-mediated successive growth of gold particles accomplished by UV irradiation: A photochemical approach for size-controlled synthesis, *J. Photochem. Photobiol. A Chem.* 140 (2001) 75–80. doi:10.1016/S1010-6030(01)00389-6.
- [58] and C.J.M. Nikhil R. Jana, Latha Gearheart, N.R. Jana, L. Gearheart,, C.J. Murphy, Seed-Mediated Growth Approach for Shape- Controlled Synthesis of Spheroidal and Rod-like Gold Nanoparticles Using a Surfactant Template, *Adv. Mater.* (2001) 1389–1393. doi:10.1002/1521-4095(200109)13:18<1389::AID-ADMA1389>3.0.CO;2-F.
- [59] B. Nik, a El Sayed, B. Nikoobakht, A. El-Sayed, B. Nik, a El Sayed, B. Nikoobakht, A. El-Sayed, Preparation and Growth Mechanism of Gold Nanorods (NRs) Using Seed - Mediated Growth Method, *Chem. Mater.* 15 (2003) 1957–1962. doi:Doi 10.1021/Cm0207321.
- [60] J.E. Millstone, S. Park, K.L. Shuford, L. Qin, G.C. Schatz, C.A. Mirkin, Observation of a quadrupole plasmon mode for a colloidal solution of gold nanoprisms, *J. Am. Chem. Soc.* 127 (2005) 5312–

5313. doi:10.1021/ja043245a.
- [61] M. Brust, M. Walker, D. Bethell, D.J. Schiffrian, R. Whyman, Synthesis of Thiol-derivatised Gold Nanoparticles in a Two-phase Liquid-Liquid System, *J. Chem. Soc. Chem. Commun.* (1994) 801–802. doi:10.1039/C39940000801.
- [62] M.N. Martin, J.I. Basham, P. Chando, S.K. Eah, Charged gold nanoparticles in non-polar solvents: 10-min synthesis and 2D self-assembly, *Langmuir*. 26 (2010) 7410–7417. doi:10.1021/la100591h.
- [63] K.-S. Kim, D. Demberelnyamba, H. Lee, Size-Selective Synthesis of Gold and Platinum Nanoparticles Using Novel Thiol-Functionalized Ionic Liquids, *Langmuir*. 20 (2004) 556–560. doi:10.1021/la0355848.
- [64] E. Oh, K. Susumu, R. Goswami, H. Matoussi, One-phase synthesis of water-soluble gold nanoparticles with control over size and surface functionalities, *Langmuir*. 26 (2010) 7604–7613. doi:10.1021/la904438s.
- [65] E. Yilmaz, S. Suzer, Au nanoparticles in PMMA matrix: In situ synthesis and the effect of Au nanoparticles on PMMA conductivity, *Appl. Surf. Sci.* 256 (2010) 6630–6633. doi:10.1016/j.apsusc.2010.04.060.
- [66] A. Pucci, M. Bernabò, P. Elvati, L.I. Meza, F. Galembeck, C.A. de Paula Leite, N. Tirelli, G. Ruggeri, Photoinduced formation of gold nanoparticles into vinyl alcohol based polymers, *J. Mater. Chem.* 16 (2006) 1058–1066. doi:10.1039/B511198F.
- [67] R. Seoudi, A.A. Fouda, D.A. Elmenshawy, Synthesis, characterization and vibrational spectroscopic studies of different particle size of gold nanoparticle capped with polyvinylpyrrolidone, *Phys. B Condens. Matter.* 405 (2010) 906–911. doi:10.1016/j.physb.2009.10.012.
- [68] M. Sakamoto, M. Fujitsuka, T. Majima, Light as a construction tool of metal nanoparticles: Synthesis and mechanism, *J. Photochem. Photobiol. C Photochem. Rev.* 10 (2009) 33–56. doi:10.1016/j.jphotochemrev.2008.11.002.
- [69] S. Eustis, H.-Y. Hsu, M. a El-Sayed, Gold Nanoparticle Formation from Photochemical Reduction of Au³⁺ by Continuous Excitation in Colloidal Solutions. A Proposed Molecular Mechanism, *J. Phys. Chem. B.* 109 (2005) 4811–4815. doi:10.1021/jp044158z.
- [70] M. Sakamoto, T. Tachikawa, M. Fujitsuka, T. Majima, Acceleration of laser-induced formation of gold nanoparticles in a poly(vinyl alcohol) film, *Langmuir*. 22 (2006) 6361–6366. doi:10.1021/la060304k.
- [71] K.L. McGilvray, M.R. Decan, D. Wang, J.C. Scaiano, Facile photochemical synthesis of unprotected aqueous gold nanoparticles, *J. Am. Chem. Soc.* 128 (2006) 15980–15981. doi:10.1021/ja066522h.
- [72] R.A. Caruso, M. Ashokkumar, F. Grieser, Sonochemical formation of gold sols, *Langmuir*. 18 (2002) 7831–7836. doi:10.1021/la020276f.
- [73] K. Okitsu, M. Ashokkumar, F. Grieser, Sonochemical Synthesis of Gold Nanoparticles: Effects of Ultrasound Frequency, *J. Phys. Chem. B.* 109 (2005) 20673–20675. doi:10.1021/jp0549374.
- [74] Yu-Ying Yu, Ser-Sing Chang, Chien-Liang Lee, and C. R. Chris Wang*, S.-S. Chang, C.-L. Lee, C.R.C. Wang, Yu-Ying Yu, Ser-Sing Chang, Chien-Liang Lee, and C. R. Chris Wang*, Gold Nanorods: Electrochemical Synthesis and Optical Properties, *J. Phys. Chem. B.* 101 (1997) 6661–6664. doi:10.1021/jp971656q.
- [75] A. Henglein, Radiolytic Preparation of Ultrafine Colloidal Gold Particles in Aqueous Solution : Optical Spectrum , Controlled Growth , and Some Chemical Reactions, (1999) 6738–6744.
- [76] F.K. Liu, C.J. Ker, Y.C. Chang, F.H. Ko, T.C. Chu, B.T. Dai, Microwave heating for the preparation of nanometer gold particles, *Japanese J. Appl. Physics, Part 1 Regul. Pap. Short Notes Rev. Pap.* 42 (2003) 4152–4158. doi:10.1143/JJAP.42.4152.
- [77] K.A. Elsayed, H. Imam, M.A. Ahmed, R. Ramadan, Effect of focusing conditions and laser parameters on the fabrication of gold nanoparticles via laser ablation in liquid, *Opt. Laser Technol.* 45 (2013) 495–502. doi:10.1016/j.optlastec.2012.06.004.
- [78] J. Polte, Fundamental growth principles of colloidal metal nanoparticles – a new perspective, *CrystEngComm.* 17 (2015) 6809–6830. doi:10.1039/C5CE01014D.
- [79] N.T.K. Thanh, N. Maclean, S. Mahiddine, Mechanisms of nucleation and growth of nanoparticles in

- solution, *Chem. Rev.* 114 (2014) 7610–7630. doi:10.1021/cr400544s.
- [80] T. Vetter, M. Iggland, D.R. Ochsenbein, F.S. Hänseler, M. Mazzotti, Modeling nucleation, growth, and ostwald ripening in crystallization processes: A comparison between population balance and kinetic rate equation, *Cryst. Growth Des.* 13 (2013) 4890–4905. doi:10.1021/cg4010714.
- [81] K. Aslan, J.R. Lakowicz, C.D. Geddes, Nanogold-plasmon-resonance-based glucose sensing, *Anal. Biochem.* 330 (2004) 145–155. doi:10.1016/j.ab.2004.03.032.
- [82] J. Matsui, K. Akamatsu, S. Nishiguchi, D. Miyoshi, H. Nawafune, K. Tamaki, N. Sugimoto, Composite of Au Nanoparticles and Molecularly Imprinted Polymer as a Sensing Material, *Anal. Chem.* 76 (2004) 1310–1315. doi:10.1021/ac034788q.
- [83] H. Wohltjen, Colloidal Metal - Insulator - Metal Ensemble Chemiresistor Sensor, *Anal. Chem.* 70 (1998) 2856–2859. doi:10.1021/ac9713464.
- [84] J.M. Bergen, H.A. Von Recum, T.T. Goodman, A.P. Massey, S.H. Pun, Gold nanoparticles as a versatile platform for optimizing physicochemical parameters for targeted drug delivery, *Macromol. Biosci.* 6 (2006) 506–516. doi:10.1002/mabi.200600075.
- [85] B.D. Chithrani, A.A. Ghazani, W.C.W. Chan, Determining the size and shape dependence of gold nanoparticle uptake into mammalian cells, *Nano Lett.* 6 (2006) 662–668. doi:10.1021/nl052396o.
- [86] W. Haiss, N.T.K. Thanh, J. Aveyard, D.G. Fernig, Determination of size and concentration of gold nanoparticles from UV-Vis spectra, *Anal. Chem.* 79 (2007) 4215–4221. doi:10.1021/ac0702084.
- [87] S. Kumar, K.S. Gandhi, R. Kumar, Modeling of Formation of Gold Nanoparticles by Citrate Method †, *Ind. Eng. Chem. (Analytical Ed.)* 46 (2007) 3128–3136. doi:10.1021/ie060672j.
- [88] T. Kim, C.H. Lee, S.W. Joo, K. Lee, Kinetics of gold nanoparticle aggregation: Experiments and modeling, *J. Colloid Interface Sci.* 318 (2008) 238–243. doi:10.1016/j.jcis.2007.10.029.
- [89] N. Sapogova, N. Bityurin, Model for UV induced formation of gold nanoparticles in solid polymeric matrices, *Appl. Surf. Sci.* 255 (2009) 9613–9616. doi:10.1016/j.apsusc.2009.04.078.
- [90] G. Vitrant, J. Bosson, N. Tosa, T. Rosenzveig, O. Stéphan, S. Astilean, P.L. Baldeck, Observation of optical dispersion effects in metallic nanostructures fabricated by laser illumination of an organic polymer matrix doped with metallic salts, *Proc. SPIE, Org. Photonic Mater. Devices IX.* 6470 (2007) 1–9. doi:10.1117/12.705881.
- [91] Q. Zhang, N. Li, J. Goebel, Z. Lu, Y. Yin, A Systematic Study of the Synthesis of Silver Nanoplates : Is Citrate a “ Magic ” Reagent ?, *J. Am. Chem. Soc.* 133 (2011) 18931–18939.
- [92] N.G. Bast, J. Comenge, V. Puntes, Kinetically Controlled Seeded Growth Synthesis of Citrate-Stabilized Gold Nanoparticles of up to 200 nm : Size Focusing versus Ostwald Ripening, *Langmuir.* 27 (2011) 11098–11105.
- [93] X. Liu, H. Xu, H. Xia, D. Wang, Rapid Seeded Growth of Monodisperse, Quasi-Spherical, Citrate-Stabilized Gold Nanoparticles via H₂O₂ Reduction, *Langmuir.* 28 (2012) 13720–13726.
- [94] S.S. Kumar, C.S. Kumar, J. Mathiyarasu, K.L. Phani, Stabilized Gold Nanoparticles by Reduction Using 3,4-Ethylenedioxythiophene-polystyrenesulfonate in Aqueous Solutions Nanocomposite Formation, Stability, and Application in Catalysis, *Langmuir.* 23 (2007) 3401–3408.
- [95] P. Shabanzadeh, R. Yusof, K. Shameli, Artificial neural network for modeling the size of silver nanoparticles' prepared in montmorillonite/starch bionanocomposites, *J. Ind. Eng. Chem.* 24 (2015) 42–50. doi:10.1016/j.jiec.2014.09.007.
- [96] E. Vatankhah, D. Semnani, M.P. Prabhakaran, M. Tadayon, S. Razavi, S. Ramakrishna, Artificial neural network for modeling the elastic modulus of electrospun polycaprolactone/gelatin scaffolds, *Acta Biomater.* 10 (2014) 709–721. doi:10.1016/j.actbio.2013.09.015.
- [97] K.L. Bhowmik, A. Debnath, R.K. Nath, S. Das, K.K. Chattopadhyay, B. Saha, Synthesis and characterization of mixed phase manganese ferrite and hausmannite magnetic nanoparticle as potential adsorbent for methyl orange from aqueous media: Artificial neural network modeling, *J. Mol. Liq.* 219 (2016) 1010–1022. doi:10.1016/j.molliq.2016.04.009.
- [98] J.D. Sitton, Y. Zeinali, B.A. Story, Rapid soil classification using artificial neural networks for use in constructing compressed earth blocks, *Constr. Build. Mater.* 138 (2017) 214–221. doi:10.1016/j.conbuildmat.2017.02.006.

- [99] M.A. Hakeem, M. Kamil, Analysis of artificial neural network in prediction of circulation rate for a natural circulation vertical thermosiphon reboiler, *Appl. Therm. Eng.* 112 (2017) 1057–1069. doi:10.1016/j.applthermaleng.2016.10.119.
- [100] A. Falamas, N. Tosa, V. Tosa, J. Of, Q. Spectroscopyradiative, Dynamics of laser excited colloidal gold nanoparticles functionalized with cysteine derivatives, *J. Quant. Spectrosc. Radiat. Transf.* 162 (2015) 207–212. doi:10.1016/j.jqsrt.2015.03.011.
- [101] J.D. Olden, M.K. Joy, R.G. Death, An accurate comparison of methods for quantifying variable importance in artificial neural networks using simulated data, *Ecol. Modell.* 178 (2004) 389–397. doi:10.1016/j.ecolmodel.2004.03.013.
- [102] Y.-C.C. Wei-chieh Huang, Photochemical synthesis of polygonal gold nanoparticles, *J. Nanoparticle Res.* 10 (2008) 697–702. doi:10.1007/s11051-007-9293-8.
- [103] A.O. Govorov, H.H. Richardson, Generating heat with metal nanoparticles, *Nano Today*. 2 (2007) 30–38. doi:10.1016/S1748-0132(07)70017-8.
- [104] M.Y. Sfeir, F. Wang, L. Huang, C.-C. Chuang, J. Hone, S.P. O'Brien, T.F. Heinz, L.E. Brus, Probing Electronic Transitions in Individual Carbon Nanotubes by Rayleigh Scattering, *Science* (80-.). 306 (2004) 1540–1543.
- [105] M. Honda, Y. Saito, N.I. Smith, K. Fujita, S. Kawata, Nanoscale heating of laser irradiated single gold nanoparticles in liquid, *Opt. Express*. 19 (2011) 12375. doi:10.1364/OE.19.012375.
- [106] J. Shah, S. Park, S. Aglyamov, T. Larson, L. Ma, K. Sokolov, K. Johnston, T. Milner, S.Y. Emelianov, Photoacoustic imaging and temperature measurement for photothermal cancer therapy, *J. Biomed. Opt.* 13 (2008) 1–19. doi:10.1117/1.294036.Photoacoustic.
- [107] F.J.O. Landa, X.L. Deán-Ben, R. Sroka, D. Razansky, Volumetric Optoacoustic Temperature Mapping in Photothermal Therapy, *Sci. Rep.* 7 (2017) 1–8. doi:10.1038/s41598-017-09069-5.
- [108] A.M.M. Gherman, N. Tosa, D.N. Dadarlat, V. Tosa, M.V. Cristea, P.S. Agachi, Temperature dynamics of laser irradiated gold nanoparticles embedded in a polymer matrix, *Thermochim. Acta*. 656 (2017) 25–31. doi:10.1016/j.tca.2017.08.008.
- [109] G. Baffou, H. Rigneault, Femtosecond-pulsed optical heating of gold nanoparticles, *Phys. Rev. B - Condens. Matter Mater. Phys.* 84 (2011) 1–13. doi:10.1103/PhysRevB.84.035415.
- [110] R.R. Letfullin, C.B. Iversen, T.F. George, Multipulse mode of heating nanoparticles by nanosecond, picosecond and femtosecond pulses, 7576 (2010) 757611-757611–11. doi:10.1117/12.852786.
- [111] E. Sassaroli, K.C.P. Li, B.E. O'Neill, Numerical investigation of heating of a gold nanoparticle and the surrounding microenvironment by nanosecond laser pulses for nanomedicine applications, *Phys. Med. Biol.* 54 (2009) 5541–5560. doi:10.1088/0031-9155/54/18/013.
- [112] V.K. Pustovalov, Theoretical study of heating of spherical nanoparticle in media by short laser pulses, *Chem. Phys.* 308 (2005) 103–108. doi:10.1016/j.chemphys.2004.08.005.
- [113] A. Plech, V. Kotaidis, S. Grésillon, C. Dahmen, G. Von Plessen, Laser-induced heating and melting of gold nanoparticles studied by time-resolved x-ray scattering, *Phys. Rev. B - Condens. Matter Mater. Phys.* 70 (2004) 1–7. doi:10.1103/PhysRevB.70.195423.
- [114] M. Rashidi-Huyeh, B. Palpant, Thermal response of nanocomposite materials under pulsed laser excitation, *J. Appl. Phys.* 96 (2004) 4475–4482. doi:10.1063/1.1794894.
- [115] A.A. Smirnov, A. Pikulin, N. Sapogova, N. Bityurin, Femtosecond laser irradiation of plasmonic nanoparticles in polymer matrix: Implications for photothermal and photochemical material alteration, *Micromachines*. 5 (2014) 1202–1218. doi:10.3390/mi5041202.
- [116] B. Lamien, H.R.B. Orlande, G.E. Eliçabe, Inverse problem in the hyperthermia therapy of cancer with laser heating and plasmonic nanoparticles, *Inverse Probl. Sci. Eng.* 25 (2017) 608–631. doi:10.1080/17415977.2016.1178260.
- [117] Y. Ren, H. Qi, Q. Chen, L. Ruan, Thermal dosage investigation for optimal temperature distribution in gold nanoparticle enhanced photothermal therapy, *Int. J. Heat Mass Transf.* 106 (2017) 212–221. doi:10.1016/j.ijheatmasstransfer.2016.10.067.
- [118] D. Dadarlat, C. Neamtu, High performance photopyroelectric calorimetry of liquids, *Acta Chim. Slov.* 56 (2009) 225–236.

- [119] G. Baffou, P. Berto, E. Bermúdez Ureña, R. Quidant, S. Monneret, J. Polleux, H. Rigneault, Photoinduced heating of nanoparticle arrays, *ACS Nano.* 7 (2013) 6478–6488. doi:10.1021/nn401924n.
- [120] X. Chen, A. Munjiza, K. Zhang, D. Wen, Molecular Dynamics Simulation of Heat Transfer from a Gold Nanoparticle to a Water Pool, *J. Phys. Chem. C.* 118 (2014) 1285–1293. doi:10.1021/jp410054j.
- [121] O.M. Wilson, X. Hu, D.G. Cahill, P. V. Braun, Colloidal metal particles as probes of nanoscale thermal transport in fluids, *Phys. Rev. B - Condens. Matter Mater. Phys.* 66 (2002) 2243011–2243016. doi:10.1103/PhysRevB.66.224301.
- [122] S. Bruzzone, M. Malvaldi, Local field effects on laser-induced heating of metal nanoparticles, *J. Phys. Chem. C.* 113 (2009) 15805–15810. doi:10.1021/jp9003517.
- [123] X. Wang, P. Gogol, E. Cambril, B. Palpant, Near- and Far-Field Effects on the Plasmon Coupling in Gold Nanoparticle Arrays, *J. Phys. Chem. C.* 116 (2012) 24741–24747.
- [124] W. Rechberger, A. Hohenau, A. Leitner, J.R. Krenn, B. Lamprecht, F.R. Aussenegg, Optical properties of two interacting gold nanoparticles, *Opt. Commun.* 220 (2003) 137–141. doi:10.1016/S0030-4018(03)01357-9.
- [125] A. Bouhelier, R. Bachelot, J.S. Im, G.P. Wiederrecht, G. Lerondel, S. Kostcheev, P. Royer, Electromagnetic interactions in plasmonic nanoparticle arrays, *J. Phys. Chem. B.* 109 (2005) 3195–3198. doi:10.1021/jp046224b.
- [126] S.K. Gray, T. Kupka, Propagation of light in metallic nanowire arrays: Finite-difference time-domain studies of silver cylinders, *Phys. Rev. B - Condens. Matter Mater. Phys.* 68 (2003) 454151–4541511. doi:10.1103/PhysRevB.68.045415.
- [127] T.E. Itina, Ultra-short laser interactions with nanoparticles in different media: From electromagnetic to thermal and electrostatic effects, *Synth. Photonics Nanoscale Mater. XIV* 2017. 10093 (2017) 1–8. doi:10.1117/12.2256509.
- [128] COMSOL Multiphysics, Wave Optics Module User's Guide, n.d.
- [129] P.B. Johnson, R.W. Christy, Optical constants of the noble metals, *Phys. Rev. B.* 6 (1972) 4370–4379. doi:10.1103/PhysRevB.6.4370.
- [130] G.M. Hale, M.R. Querry, Optical Constants of Water in the 200-nm to 200-microm Wavelength Region., *Appl. Opt.* 12 (1973) 555–563. doi:10.1364/AO.12.000555.
- [131] N. Zeng, A.B. Murphy, Heat generation by optically and thermally interacting aggregates of gold nanoparticles under illumination, *Nanotechnology.* 20 (2009) 375702, 1–8. doi:10.1088/0957-4484/20/37/375702.